Modeling and Control of Impedance Source Converters for Grid-Connected PV Systems

Liu, Wenjie

DOI (link to publication from Publisher):
10.5278/vbn.phd.eng.00081

Publication date:
2021

Document Version
Publisher's PDF, also known as Version of record

MODELING AND CONTROL OF IMPEDANCE SOURCE CONVERTERS FOR GRID-CONNECTED PV SYSTEMS

BY
WENJIE LIU

DISSERTATION SUBMITTED 2021

AALBORG UNIVERSITY
DENMARK

Modeling and Control of Impedance Source Converters for Grid-Connected PV Systems

Ph.D. Dissertation

Wenjie Liu

A Dissertation Submitted to the Faculty of Engineering and Science at Aalborg University in Partial Fulfilment for the Degree of Doctor of Philosophy in Electrical Engineering

Dissertation submitted Jan., 2021

Dissertation submitted: January 2021

PhD supervisor: Assoc. Prof. Yongheng Yang
Aalborg University

Assistant PhD supervisors: Assoc. Prof. Tamas Kerekes
Aalborg University

Prof. Frede Blaabjerg
Aalborg University

PhD committee: Professor Stig Munk-Nielsen (chairman)
Aalborg University

Professor Haitham Abu-Rub
Texas A&M University at Qatar

Professor Liuchen Chang
University of New Brunswick

PhD Series: Faculty of Engineering and Science, Aalborg University

Department: Department of Energy Technology

ISSN (online): 2446-1636
ISBN (online): 978-87-7210-879-7

Published by:
Aalborg University Press
Kroghstræde 3
DK – 9220 Aalborg Ø
Phone: +45 99407140
aauf@forlag.aau.dk
forlag.aau.dk

Printed in Denmark by Rosendahls, 2021

Abstract

As the key interface for delivering renewable energy, e.g., photovoltaic (PV) energy, to the grid or residential load, stringent requirements are then considered in the developments of power converters. The impedance source converter (ISC) can operate as a single-stage buck-boost converter with a wider operational range, which shows advantages over the traditional two-stage inverters. Moreover, the input source of the ISC can be either a voltage source or a current source, making the ISC-based renewable generation system more reliable. However, the utilization of the impedance source network (ISN) as well as the additional shoot-through (ST) state in ISC introduces challenges for practical applications. Thus, in this Ph.D. project, the widely adopted quasi-Z-source converter (qZSC) is exemplified to explore the application of the ISCs for PV systems.

One of the challenges is that the ISN complicates the operational state analysis of the qZSC with varying conditions. Generally, the operational states of the qZSC are classified into ST state and non-ST state. However, for the PV source with intermittent and low-voltage features, undesired abnormal operational modes will occur under extreme conditions, which deteriorates the entire PV generation system. Meanwhile, the system models should be derived to further investigate the system dynamics. The passive components affect the dynamics of the ISN, while the qZSN and the inverter part of the qZSC couple with each other. Thus, the energy transfer modes as well as the dynamic models of the qZSC are essential for optimizing the entire system. The qZSC system is venerable to oscillations when encountering transient disturbances, which is also a big challenge for the application of the qZSC in the PV generation system. The oscillation comes from the insufficient damping inside the qZSC, which will further cause stability issues. Unlike the two-stage structure, the ISN is obviously coupled with the inverter part intensively in the qZSI system, leading to that the ac control loop of the qZSC is inappropriate to be designed like a conventional VSI. Thus, to address this issue, the transient disturbances need to be included in the ac control loop of the qZSC with an adequate margin, making the PV system operate effectively with a wider input range.

Another challenge is due to the adoption of the ST state, e.g., large inductor current ripple (ICR) and additional common-mode voltage (CMV) state. The unoptimized ICRs lead to the requirement of large inductors. The maximum ICR is generally taken into consideration when designing the inductance, which affects the size of the ISN as well as the power density. Meanwhile, the introduced ST switching vector introduces an additional CMV state, making the CMV reduction methods for the voltage source inverter (VSI) inappropriate for the qZSC. As the source of the leakage current as well as electromagnetic interference (EMI), the CMV should be well tackled in the transformerless qZSC-based PV systems. Thus, the ICR reduction and CMV reduction methods should be explored for the application of the qZSC in PV systems. Meanwhile, the ISC can also be used in multilevel inverters, like the neutral-point-clamped (NPC) inverters. In that case, the additional ST state can address the issue like neural-point voltage imbalance to some extent. With more ISNs in the NPC inverter, there are more control freedoms. How to make full use of the new states could be of interest.

To tackle the above issues for ISC-based PV systems, this Ph.D. project proposes solutions for modeling and control of the ISCs for grid-connected PV systems. Firstly, the energy transfer modes for the qZSC are used to derive all the possible operating modes of the qZSC as well as the critical parameters. Meanwhile, the small-signal models of the qZSC are derived to investigate the dynamics of the qZSC system with the ISN. Furthermore, by including the operational conditions of the ISN into the ac control loop of the qZSC, the coupled control model is used to assist the stability analysis under different operational conditions. To extend the operational range of the qZSC, a design process for the coefficient selection of the ac side controller has been proposed, which enhances the oscillation suppression capability under variations. Then, to optimize the ICR, the instantaneous ICRs of the qZSC with the conventional ZSVM6 have been analyzed. Modified ZSVM6 strategies are proposed in this project to limit the maximum ICR. As for the additional CMV state introduced by the ST state, a CMV reduction strategy is introduced to make a balance between the average CMV from the conventional switching vectors of the VSI and the CMV from the ST switching vector. The input inductor is split to achieve the balance of the CMVs under the ST state and the non-ST state of the qZSC. Finally, with the extra ST state in the qZSN-based NPC inverter, a neutral-point voltage strategy is developed by using the additional operational modes. The above contributions are presented in five chapters in this thesis, which is technically divided into two parts: *Operational Mode Analysis and Modeling of the QZSC* and *Advanced Modulation and Control for the QZSI*.

Resumé

Som nøglekomponent til levering af vedvarende energi, f.eks. Solenergi (PV), der er strenge krav i udviklingen af frekvensomformere. Impedanskilde-frekvensomformeren (ISC) kan fungere som en enkelt-trins buck-boost konverter med et bredere driftsområde, hvilket viser fordele i forhold til de traditionelle to trins frekvensomformere. Desuden kan ISC's indgangskilde være enten en spændingskilde eller en strømkilde, hvilket gør det ISC-baserede system til vedvarende produktion mere pålideligt. Imidlertid introducerer brugen af impedanskildenetværket (ISN) såvel som den ekstra shoot-through (ST) -tilstand i ISC, udfordringer til praktiske anvendelser. I denne Ph.D. projekt, er den bredt vedtagne kvasi-Z-kilde konverter (qZSC) eksemplificeret for at undersøge anvendelsen af ISC'erne til solcelleanlæg.

En af udfordringerne er, at ISN komplicerer den operationelle tilstandsanalyse af qZSC under forskellige forhold. Generelt klassificeres de operationelle tilstande i qZSC i ST-tilstand og ikke-ST-tilstand. For PV-kilden med intermitterende og lavspændingsfunktioner vil der imidlertid forekomme uønskede unormale driftstilstande under ekstreme forhold, hvilket forværrer hele PV-genereringssystemet. I mellemtiden skal systemmodellerne udledes for yderligere at undersøge systemets dynamik. De passive komponenter påvirker dynamikken i ISN, mens DC-siden og AC-siden af qZSC parrer hinanden. Således er energioverførselstilstande såvel som de dynamiske modeller af qZSC afgørende for at optimere hele systemet. QZSC-systemet er ærværdigt over for svingninger, når der opstår forbigående forstyrrelser, hvilket også er en stor udfordring for anvendelsen af qZSC i PV-systemet. Svingningen kommer fra den utilstrækkelige dæmpning inde i qZSC, hvilket yderligere vil medføre stabilitetsproblemer. I modsætning til to trins strukturen med en stor afkobling af jævnstrømsforbindelseskondensator er ISN naturligvis koblet med vekselstrømsiden intensivt, hvilket gør vekselstrømsst -yringssløjfen af qZSC upassende til at blive designet som en konventionel VSI. For at løse dette problem skal de forbigående forstyrrelser således inkluderes i qZSC's vekselstrømsstyringssløjfe med en passende margen, hvilket får PV-systemet til at fungere effektivt med et bredere inputområde.

En anden udfordring skyldes vedtagelsen af ST-tilstanden, fx stor induktorstrømskridt (ICR) og yderligere common-mode-spænding (CMV). De uoptimerede ICR'er fører til krav for store induktorer. Den maksimale ICR tages generelt i betragtning ved design af induktansen, som påvirker ISN-størrelsen såvel som effekttætheden. I mellemtiden introducerer den indførte ST-skiftevektor en yderligere CMV-tilstand, hvilket gør CMV-reduktio -nsmetoderne til spændingskildeomformeren (VSI) upassende for qZSC. Som kilde til læk strømmen samt elektromagnetisk interferens (EMI) skal CMV tackles i de transformerløse qZSC-baserede solcelleanlæg. Således bør ICR-reduktions- og CMV-reduktio -nsmetoder undersøges til anvendelse af qZSC i solcelleanlæg. I mellemtiden kan ISC også bruges i invertere med flere niveauer, ligesom de neutrale punktklemmede (NPC) invertere. I så fald kan den yderligere ST-tilstand til en vis grad løse problemet som ubalance i neurale punkter. Med flere ISN'er i NPC-inverteren er der flere kontrolfriheder. Hvordan man udnytter de nye tilstander fuldt ud, kan være af interesse.

For at tackle ovenstående spørgsmål for ISC-baserede solcelleanlæg, denne Ph.D. projekt foreslår løsninger til modellering og styring af ISC'erne til nettilsluttede solcelleanlæg. For det første, bruges energioverførselsmetoderne til qZSC til at udlede alle mulige driftstilstande for qZSC såvel som de kritiske parametre. I mellemtiden er de små signalmodeller af qZSC afledt for at undersøge dynamikken i qZSC-systemet med ISN. Ved at inkludere ISN's driftsbetingelser i qZSC's vekselstrømsstyringssløjfe bruges den koblede styringsmodel desuden til at hjælpe stabilitetsanalysen under forskellige driftsforhold. For at udvide driftsområdet for qZSC er der blevet foreslået en designproces til koefficientvalg af vekselstrømsregulatoren, som forbedrer undertrykkelsesfunktionen for svingninger under variationer. Derefter er de øjeblikkelige ICR'er af qZSC med den konventionelle ZSVM6 blevet analyseret for at optimere ICR. Modificerede ZSVM6-strategier foreslås i dette projekt for at begrænse den maksimale ICR. Hvad angår den yderligere CMV-tilstand, der er indført med ST-tilstand, introduceres en CMV reduktionsstrategi for at skabe en balance mellem den gennemsnitlige CMV fra de konventionelle skiftevektorer i VSI og CMV fra ST-skiftevektoren. Indgangsspolen er delt for at opnå balancen mellem CMV'erne under ST tilstanden og ikke-ST tilstanden for qZSC. Endelig, med den ekstra ST tilstand i den qZSN-baserede NPC-inverter, udvikles en neutral-spændingsstrategi ved hjælp af de ekstra driftsformer. Ovennævnte bidrag er præsenteret i fem kapitler i denne afhandling, som teknisk er opdelt i to dele: Operationel tilstandsanalyse og modellering af QZSC og Advanceret Modulation og Styring til QZSI.

Preface

This Ph.D. thesis is a summary of the Ph.D. project "*Modeling and Control of Impedance Source Converters for Grid-Connected PV Systems*". This Ph.D. project is mainly supported by the Department of Energy Technology, Aalborg University, Denmark, Otto Mønsteds Fond, and Dora Pluss Scholarships. I would like to thank for all the supports obtained from them.

First of all, I would like to express my sincere gratitude to my supervisor, Assoc. Prof. Yongheng Yang, for his patient and professional guidance throughout my Ph.D. project. This Ph.D. thesis could not be finalized without his support. I would also like to thank my co-supervisors, Assoc. Prof. Tamas Kerekes and Prof. Frede Blaabjerg, for their consistent advice and encouragement. I am really honored to have this chance to work with them.

Special thanks go to Prof. Dmitri Vinnikov, Dr. Oleksandr Husev, and Dr. Andrii Chub for their enthusiastic guidance and industrial vision during my stay at Tallinn University of Technology, Estonia. Also, thanks to Oleksandr Matiushkin, Bohdan Pakhaliuk, Denys Zinchenko, Vadim Sidorov, and Dr. Oleksandr Korkh for the fun and inspiration in the Power Electronics Group.

I would like to extend my gratitude to all my local and external colleagues from the Department of Energy Technology, Aalborg University, Denmark. Many thanks to Dr. Zhongting Tang, Dr. Qiao Peng, Dr. Jing Yuan, Dr. Zhan Shen, Dr. Weihua Zhou, Dr. Zhengge Chen, Dr. Mengxin Chen, Dr. Songda Wang, Yiwei Pan, Hongbo Zhao, Kamran Ali Khan Niazi, and all my lovely colleagues at the Department of Energy Technology, Aalborg University for their kind help.

Last but not least, I would like to express my sincere gratitude to my parents and my wife Xinrong Huang for their endless love all the way. Without their support, this project would not be possible.

Wenjie Liu
January 19, 2021

Contents

Report

Part I

Preamble

Part I *is the preamble of this Ph.D. project, in which only one chapter, i.e.,* ***Chapter 1****. Introduction, is included.*

1 Introduction

The background and motivation of this Ph.D. project are firstly presented in this chapter, which also briefly introduces the impedance source converter (ISC) for photovoltaic (PV) applications. Then, the research objectives and limitations are discussed, followed by the outline of this Ph.D. thesis. At the end of this chapter, the publications related to this Ph.D. project are listed.

1.1 Background and Motivation

With the deficiency of fossil fuels, the interest in solar PV energy has been growing worldwide. By 2019, the global solar PV installation capacity has reached 627 GW [1], taking a large share in the electricity market with no sign of slowing down. Meanwhile, the cost of the recent PV power generation technology has been reduced as well. However, the fluctuating power generated from solar power systems is dependent on weather conditions, e.g., solar irradiance and ambient temperature, imposing new challenges with the increase of the penetration level of PV technologies. increases [2, 3]. In fact, without the key interface, i.e., power electronic converter system, renewable energy sources including Solar PV energy can not be integrated into the grid or residential applications [4]. A typical schematic diagram of a power electronics conversion system for PV applications with high controllability is shown in Fig. 1.1. The power generated by the PV panels can be further regulated by the power electronic converter according to the grid/load requirements.

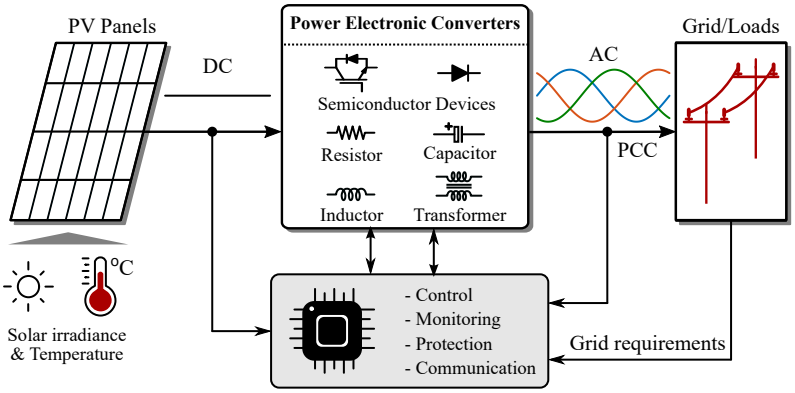

Fig. 1.1: Typical diagram of a power electronic conversion system for PV applications, in which PCC is the point of common coupling.

Due to the wide output voltage range of PV modules, the most commonly used voltage source inverter (VSI) is no longer suitable for PV power conversion systems. Generally, a front-end DC-DC converter is used to regulate the dc-link voltage for the ac part, which is the so-called two-stage inverter [5], as shown in Fig. 1.2(a). With a bulky electrolytic capacitor, the dc-link voltage in the two-stage structure is kept constant, thereby decoupling the two stages [6]. Maximum power point tracking (MPPT) can be realized by regulating the front-end DC-DC converter during the intensive PV power variation [7]. However, the two-stage structure will increase the cost and lower the efficiency of the entire energy conversion system.

Since the proposal of the impedance source converter (ISC) in 2003, i.e., Z-source inverter (ZSI) [8], it has gained widespread attentions. The ISC is proposed to overcome the limitations of the voltage/current source converters by employing a special impedance source network (ISN) [9–13]. The ISNs can be used in all power converter systems, e.g., dc-dc, dc-ac, and ac-ac systems [14]. With the ISN, the original converter can be coupled with the input source, load, or other converters. A typical ISC-based PV system is shown in Fig. 1.2(b). The ISN in Fig. 1.2(b) makes the system capable of single-stage boosting. The additional shoot-through (ST) state, which is forbidden in the VSI, enables the input source of the ISC as a voltage source or a current source, improving the system reliability to a certain extent, even short-circuiting the phase leg is available. With appropriate modulation strategies, the ST state will not affect the operation of the inverter part [15]. Although the ISC has shown many advantages when compared with the two-stage inverter, there are still certain issues to be solved seen from the perspective of PV applications. Thus, this Ph.D. project will focus on how to modeling and control the ISC-based system for PV applications.

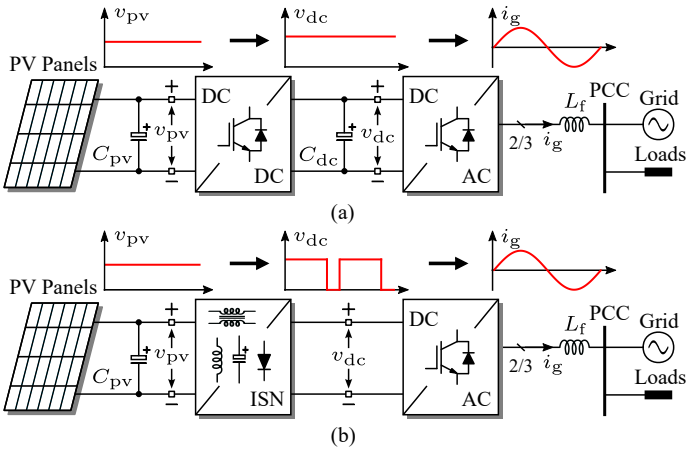

Fig. 1.2: Configurations of typical PV systems with (a) a two-stage inverter and (b) an impedance source inverter, in which C_{pv} and C_{dc} are the input capacitor and the DC-link capacitor, L_f is the output filter, v_{pv} and v_{dc} are the input voltage and the DC-link voltage, and i_g is the output current of the inverter.

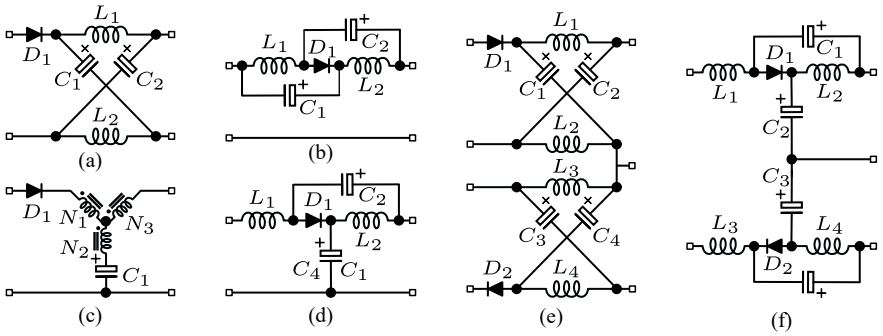

Fig. 1.3: Popular topologies of the impedance network: (a) Z-source network, (b) quasi-Z-source network with a discontinuous input current, (c) Y-source network, (d) quasi-Z-source network with a continuous input current, (e) neutral-point-clamped Z-source network, and (f) neutral-point-clamped quasi-Z-source network.

1.1.1 Impedance Source Converters for PV Systems

Various ISN topologies, modulation strategies, and control methods have been proposed in the literature [16–20]. The most popular ISN topologies are present in Fig. 1.3. The first proposed Z-source network (ZSN) in Fig. 1.3(a) is a two-port network with two capacitors C_1, C_2, two inductors, L_1, L_2, and a diode D_1. By rearranging the elements in the ZSN, the quasi-Z-source networks (qZSNs) in Figs. 1.3(b) and (d) can be obtained [21]. The ISN topologies focus on higher boosting capability and lower component stress. With the coupled inductor technology, the Y-source network shown in Fig. 1.3(c)

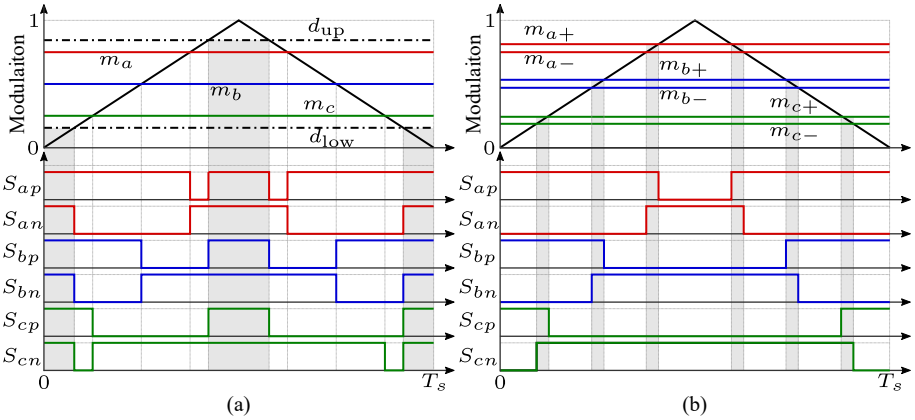

Fig. 1.4: Modulation strategies for the ISCs with: (a) sinusoidal PWM and (b) space-vector PWM in a switching cycle, in which m_a, m_b and m_c are the modulation references, d_{up} and d_{down} are the ST references for the SPWM strategies, $m_{a+/-}$, $m_{b+/-}$ and $m_{c+/-}$ are the shifted modulation references for the SVPWM strategies, $S_{ap/n}$, $S_{ap/n}$ and $S_{ap/n}$ are the switching signals.

can achieve a higher boosting gain, which serves as a basic unit for further topology derivation [22, 23]. The basic two-port ISN can be used to construct new structures, e.g., the neutral-point-clamped (NPC) ISNs in Figs. 1.3(e) and (f) [24]. However, the ISNs in Figs. 1.3(a)-(c) and (e) with a discontinuous input current are inappropriate for renewable applications. The qZSN in Fig. 1.3(d) can ensure a continuous input current, and the voltage stress can be reduced when compared with the ZSN. Correspondingly, the NPC-qZSN in Fig. 1.3(f) shows the same operating characteristics as the qZSN in Fig. 1.3(d). Therefore, the qZSN-based inverter, i.e., quasi-Z-source inverter (qZSI), is exemplified to explore the application of the ISC in PV systems.

The ISC can achieve the boosting capability with the additional ST state, which is not allowed in the conventional VSI [25]. To implement the ST state, modifications in the conventional pulse width modulation (PWM) strategies are necessary. The modulation strategies for the ISC can be divided into sinusoidal PWM (SPWM) and space-vector PWM (SVPWM) [15]. For the SPWM strategies, e.g., simple boost control (SBC) [8], maximum boost control (MBC) [26], and maximum constant boost control (MCBC) [27], two additional ST references, i.e., d_{up} and d_{low}, are needed to insert the ST state into the zero state for the inverter, as shown in Fig. 1.4(a). There will be extra switching commutations during the switching cycle when the SPWM strategy is used to insert the ST intervals. By shifting the modulation references, the SVPWM strategies, e.g, ZSVMx ($x = 1, 2, 4, 6$), can be achieved [28], as seen in Fig. 1.4(b). The active states of the SVPWM strategies are maintained without additional switching commutations when the ST intervals are inserted into the corresponding switching instant [29]. In addition, more modulation

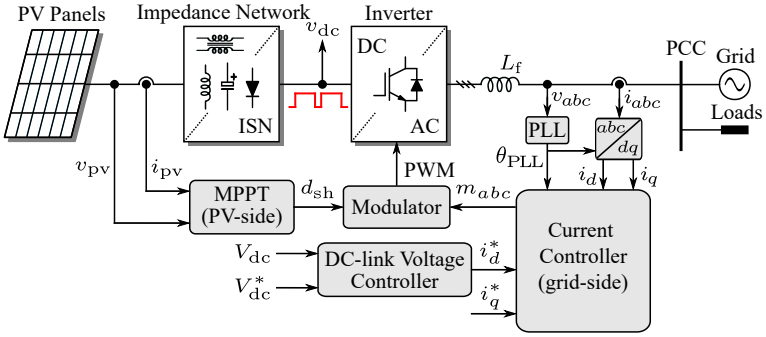

Fig. 1.5: General control configuration of the ISC-based PV generation system, in which v_{pv} and i_{pv} are the output voltage and current of the PV panels, v_{abc} and i_{abc} are the voltage and current at the PCC, θ_{PLL} is the phase angle tracked by the phase-locked loop (PLL), $i_{d/q}$ and $i^*_{d/q}$ are the actual currents and the reference currents for the three phases in dq-frame, V_{dc} and V^*_{dc} are the DC-link voltage variable and the corresponding reference, d_{sh} is the ST duty ratio, m_{abc} are the modulation ratios, and L_f is the output filter.

strategies have been proposed in the literature to improve the ISC system performance, e.g., higher boosting gain and less switching commutations.

Similar to the two-stage inverter, there are two control variables in the ISC, i.e., the modulation index and the ST duty ratio. Therefore, the ISC-based PV system can be controlled like a two-stage structure [30], as shown in Fig. 1.5, in which the MPPT controller is adopted to generate the ST duty ratio, and the current controller generates the modulation index [31]. However, the "DC-link" voltage (v_{dc}, see Fig. 1.5) is not constant in the ISC, making the control of the DC-link voltage different from that in the two-stage inverter. There will be direct and indirect strategies to control the DC-link voltage in the ISC [15]. With special measuring circuits, the peak of v_{dc} can be monitored and controlled directly, which will increase the cost and volume of the entire system. Unlike the direct control, the capacitor voltage in the ISN or the estimated peak of v_{dc} will be considered as the control variable in the indirect strategy [16, 32, 33]. When the capacitor voltage in the ISN is controlled as the dc-link voltage, the peak value of v_{dc} across the inverter will change when the input voltage varies [34]. Meanwhile, the peak of v_{dc} can be estimated through the relationship among the input voltage, the capacitor voltage in the ISN, and the ST duty ratio [35]. Many nonlinear controllers have been proposed to improve the transient performance of the ISC system [36–38].

To make full use of solar PV energy, higher requirements are essential for the power electronic converter system. As a transformerless alternative to the two-stage inverter, the ISC will encounter new challenges in practical PV applications. Therefore, further exploration of the ISC-based PV generation system should be performed in detail.

1.1.2 Project Motivation

As discussed previously, the ISN couples the input source and the inverter part to achieve the buck-boost operation. With the ISN in PV generation systems, the operational modes become complicated when various operational conditions are considered. Under extreme operational conditions, undesirable operating modes can occur, which affect the output power quality. To improve system performance, a full picture of all operating modes should be investigated. Without the large decoupling capacitor that existed in the two-stage structure, the coupling, e.g., the input and the inverter through the ISN, makes the inverter controller more complicated. The ISC-based system is also prone to oscillation when encountering transient disturbances from the operating conditions. Therefore, a detailed system model should be derived to study how the ISN affects the system dynamics.

The ST state will also challenge the application of the ISC in PV generation systems. The input current ripple in the ISN, i.e., large inductor current ripples (ICRs), can be affected by the adoption of the ST state. Large ICRs lead to the need of large inductors, thereby lowering the system power density. Although increasing the switching frequency or using coupled inductors can alleviate this issue, the overall system cost will increase as well. Since the ST state is implemented through modulation technologies, the ICR reduction with appropriate modulation strategies becomes essential. As closely related to leakage currents, the common-mode voltage (CMV) should be tackled in the transformerless ISC-based PV-systems. The ST switching vector introduces an additional CMV state, making the CMV reduction methods for the VSI inappropriate for the ISC-based systems. Therefore, the exploration of the ICR reduction and CMV reduction methods becomes important in the transformerless ISC-based PV-systems.

There are inherent issues in conventional typologies such as NPC inverter, e.g., unbalanced neutral-point voltage (NPV). The NPV imbalance, which comes from the mismatch between the mid-point capacitance and device characteristics, can lead to severe output current harmonics, and even cause system shut-down in practical applications. Usually, the switching vectors related to the NPV can be controlled to solve this issue. Due to the module feature of the two-port ISN, there will be more control degrees of freedoms introduced into the ISN-module-based PV systems, e.g., the NPC ISNs in Figs. 1.3(e) and (f). The ISN modules in the ISN-module-based system can operate in the same or the opposite operational state by controlling the upper-bridge ST state and the lower-bridge ST state separately, which can control the NPV and CMV of the ISN-based NPC inverter simultaneously. With more controllable ST switching vectors, there could be new solutions to tackle these issues in the ISN-based NPC inverter for PV applications.

1.2 Project Objectives and Limitations

1.2.1 Research Questions and Objectives

This Ph.D. project aims at investigating the ISC for PV applications, including modeling and control of the ISC-based PV systems. Considering the unique feature of the ISC, new challenges emerge for PV applications when compared with the conventional system structure. To enhance the utilization of the ISC-based PV systems, the following overall research question for this Ph.D. project is defined:

- **How to make the most of the ISC-based power conversion system to improve the performance of PV systems with appropriate modeling, modulation and control?**

To answer this question, the challenges that the transformerless ISC-based PV generation system faces should be aware of. Thus, according to the overall research question for the application of the ISC-based converter in PV system, the following sub-questions have been considered through the project:

- Q1: How to ensure the system performance with proper system parameters under different operational conditions?
- Q2: How to model the effect of the ISN on the system controller design when the ISN is coupled with the inverter?
- Q3: How to reduce the inductor current ripples through modulation of the inverter by properly implementing the ST states?
- Q4: Are there any methods to reduce the CMV (then, the leakage currents) for the ISC-based PV system?
- Q5: How can the ST variable be utilized to solve the inherent issues in the conventional converter structure for system enhancement?

To find the answers to those questions, several objectives are motivated by this Ph.D. project for the ISC-based PV system as:

- **O1: Energy transfer mode analysis of the qZSN-based converter considering critical parameters for different operational modes**

  Besides the general operational state, there will be a new state occurring when the inductance is inappropriate. The qZSN-based converter will be simplified for the analysis of the energy transfer process, which can be used to derive the critical parameters. With the parameter consideration, the undesired operational mode can be avoided.

- **O2: Small-signal modeling of the qZSN-based inverter considering the coupling between the ISN and the inverter part**

  The dc-link voltage through the inverter part is affected by the operational conditions, e.g., input voltage, ST duty ratio, and load conditions. A small-signal model will be obtained to study the coupling between the ISn and the inverter part. The oscillation triggered by the input variation is explored to enhance system stability. More consideration will be provided for the controller design for the inverter part.

- **O3: Inductor Current Ripple Analysis and Reduction for the qZSN-based inverter with modified SVPWM strategies**

  The inductor current ripple in the ISN is smaller using the SVPWM strategies with more ST intervals, e.g., the ZSVM6, when compared with the SPWM strategies. To further optimize the inductor current ripple, the instantaneous inductor current ripples when the conventional ZSVM6 strategy is used will be calculated in detail. According to the instantaneous current ripples with the conventional ZSVM6 strategy, improved ZSVM6 strategies can be proposed to limit the maximum instantaneous current ripple for ripple reduction.

- **O4: CMV reduction for the qZSN-based inverter to alleviate the high-frequency harmonics introduced by the additional ST states**

  The ST state introduces a new CMV value, which can increase the high-order harmonics in the CMV. The CMV reduction strategies for the VSI will be unavailable for the qZSN-based inverter with the ST vector, which generates a new CMV state, increasing the high-frequency harmonics. According to the CMV under different operational states, a CMV reduction strategy by modifying the qZSN is proposed to alleviate the effect of the additional ST states on the high-frequency harmonics and make the CMV reduction strategies for the VSI available for the qZSN-based inverter.

- **O5: NPV balance and CMV reduction simultaneously in the qZSN-based NPC inverter by controlling the extra ST variables**

  The switching patterns in the NPC inverter are used for NPV balance and CMV reduction. However, the switching vectors that can balance the NPV might increase the CMV in the applications, e.g., the small vectors that relate to the half-bridge voltage. The extra ST states in the qZSN-based NPC inverter will be analyzed to find how these states affect the NPV. The switching state and corresponding CMV magnitude are derived for the qZSN-based NPC inverter. Then, an improved control method for NPV balance and CMV reduction can be achieved simultaneously by optimizing the switching pattern.

1.2.2 Project Limitation

There are several assumptions and limitations in this Ph.D. project:

- Various ISCs have been proposed in the literature, but only the qZSN-based inverters are explored in this Ph.D. project. Other topologies, e.g., inductor-coupled ISN, which may show different characteristics, are not discussed. The strategies proposed in this Ph.D. project can also be used for the topologies with a similar structure.
- Although the non-linear features of the passive components are important, the passive components in the qZSN-based inverters, e.g., inductors and capacitors, are assumed to be ideal in the analysis.
- To explore the ISN-based inverters for PV applications, the characteristics of the conventional inverters, e.g., the VSI and the NPC inverter, are assumed to operate in an ideal way.

1.3 Thesis Outline

The Ph.D. project in the document of this Ph.D. thesis contains a formal ***Report*** and a collection of ***Selected Publications*** during the Ph.D. period. The structure of this Ph.D. thesis is illustrated in Fig. 1.6. There are four parts in the formal ***Report***, including seven chapters, and relevant papers are shown to enrich these chapters. The research questions and corresponding objectives **Q/O1-Q/O5** are discussed in *Chapters 2-6*, respectively.

Part I is the preamble, in which *Chapter 1. Introduction* is included. An overview of the ISC about topologies, modulation strategies, and control methods is presented in *Chapter 1*, followed by the motivation of this Ph.D. project. The research questions, objectives, and limitations for this Ph.D. project are also discussed in this chapter. **Part II** - "Operational Mode Analysis and Modeling of the QZSC" has two chapters, which are *Chapter 2. Operational Mode Analysis of the QZSC* and *Chapter 3. Interactive Modeling and Stability Analysis of the QZSC*. The energy transfer modes of the qZSC are derived in *Chapter 2* for the critical system parameters. *Chapter 3* presents the interactive small-signal models of the qZSC, revealing how the ISN affects the control of the inverter part. There are three chapters, i.e., *Chapters 4*, *5* and *6*, in **Part III** - "Advanced Modulation and Control for the QZSI". *Chapter 4. Inductor Current Ripple Reduction through Modulation* analyzes the instantaneous inductor current ripple when the conventional ZSVM6 strategy is used, and accordingly, an improved SVPWM strategy is further proposed to optimize the inductor current ripple. The CMV reduction methods for the qZSC to alleviate the high-frequency harmonics introduced by the ST state are explored in *Chapter 5. Common-Mode Voltage Mitigation for PV Applications*. *Chapter 6. Control of the QZSN-Based NPC Inverter* deals with the NPV balance

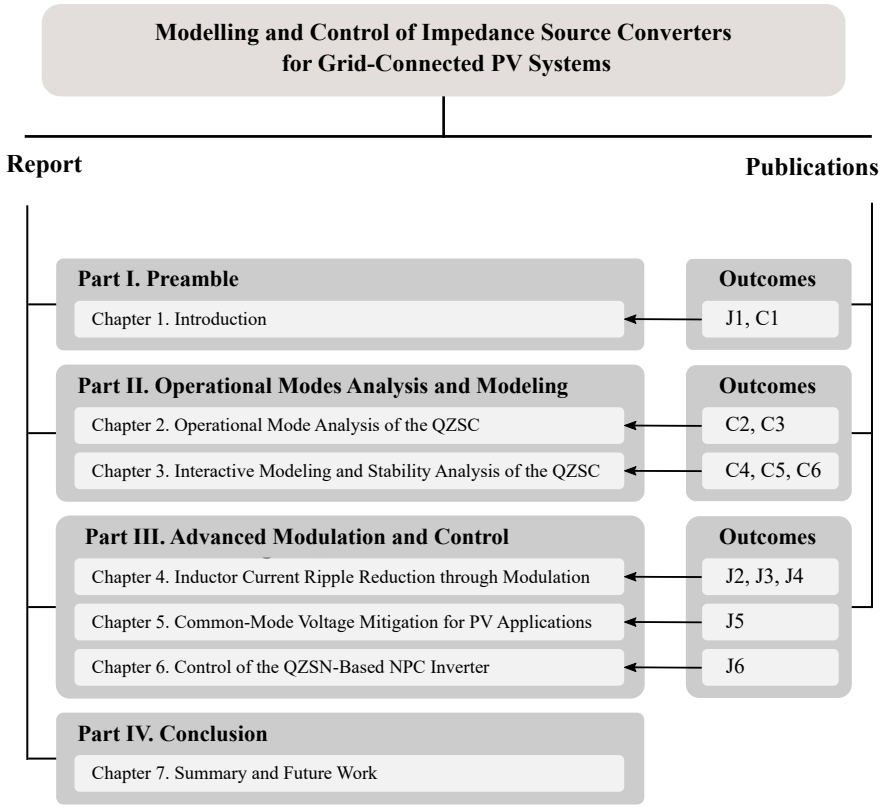

Fig. 1.6: Outline of this Ph.D. thesis and related publications, in which publications J1-J7 and C1-C9 are listed in Section 1.4.

and CMV reduction simultaneously. The Ph.D. project is concluded in **Part IV**- "Conclusion", in which *Chapter 7. Summary and Future Work* gives the main contributions and perspectives of this Ph.D. work.

1.4 List of Publications

A list of the papers derived from this project, which are published till now or have been submitted, is given as follows:

Journal Papers

J1. **W. Liu**, K. A. K. Niazi, T. Kerekes, and Y. Yang, "A Review on Transformerless Step-Up Single-Phase Inverters with Different DC-Link Voltage for Photovoltaic Applications," *Energies*, vol. 12, no. 19, pp. 1-17, Jan. 2019.

J2. **W. Liu**, Y. Yang, T. Kerekes, D. Vinnikov, and F. Blaabjerg, "Inductor Current Ripple Analysis and Reduction for Quasi-Z-Source Inverters with An Improved ZSVM6 Strategy," *IEEE Trans. Power Electron.*, in press, 2020.

J3. **W. Liu**, Y. Yang, T. Kerekes, and F. Blaabjerg, "Generalized Space Vector Modulation for Ripple Current Reduction in Quasi-Z-Source Inverters," *IEEE Trans. Power Electron.*, vol. 36, no. 2, pp. 1730–1741, Feb. 2021.

J4. **W. Liu**, Y. Yang, T. Kerekes, and F. Blaabjerg, "Inductor Ripple Reduction in the QZSI by Limiting the Maximum Instantaneous Current Ripple," *IEEE Trans. Ind. Electron.*, to be submitted, 2021.

J5. **W. Liu**, Y. Yang, T. Kerekes, E. Liivik, D. Vinnikov, and F. Blaabjerg, "Common-Mode Voltage Analysis and Reduction for the Quasi-Z-Source Inverter with A Split Inductor," *Applied Sciences*, vol. 10, no. 23, pp. 1-13, Jan. 2020.

J6. **W. Liu**, Y. Yang, T. Kerekes, and F. Blaabjerg, "Neutral-Point Voltage Balance Strategy for the Three-Level Neutral-Point-Clamped Quasi-Z-Source Inverter with Common-Mode Voltage Reduction," *IEEE Trans. Ind. Electron.*, under preparation, 2021.

Conference Contributions

C1. **W. Liu**, Y. Yang, and T. Kerekes, "Characteristic Analysis of the Grid-Connected Impedance-Source Inverter for PV Applications," in *Proc. IEEE PEDG*, pp. 874–880, Jun. 2019.

C2. **W. Liu**, Y. Yang, E. Liivik, D. Vinnikov, and F. Blaabjerg, "Critical Parameter Analysis and Design of the Quasi-Z-Source Inverter," in *Proc. IEEE UKRCON*, pp. 474–480, Jul. 2019.

C3. **W. Liu**, T. Kerekes, and Y. Yang, "Energy Transfer Modes of the Quasi-Z-Source DC-DC Converter Considering Critical Inductance," in *Proc. IPEMC - IEEE ECCE Asia*, pp. 1–6, in press, 2020.

C4. **W. Liu**, Y. Pan, and Y. Yang, "Small-Signal Modeling and Dynamic Analysis of the Quasi-Z-Source Converter," in *Proc. IEEE IECON*, pp. 5039–5044, Oct. 2019.

C5. **W. Liu**, J. Yuan, Y. Yang, and T. Kerekes, "Modeling and Control of Single-Phase Quasi-Z-Source Inverters," in *Proc. IEEE IECON*, pp. 3737–3742, Oct. 2018.

C6. **W. Liu**, Y. Yang, T. Kerekes, E. Liivik, and F. Blaabjerg, "Impedance Network Impact on the Controller Design of the QZSI for PV Applications," in *Proc. IEEE COMPEL*, pp. 1–6, Nov. 2020.

The publications done during the Ph.D. study but excluded in the Ph.D. thesis are listed below:

- **W. Liu**, Y. Yang, T. Kerekes, and F. Blaabjerg, "Current Ripple Reduction for the Quasi-Z-Source Inverter with Modified Space-Vector PWM Strategy," in *Proc. IEEE ECCE*, pp. 1867–1872, Oct. 2020.
- **W. Liu**, Y. Yang, and T. Kerekes, "Modified Quasi-Z-Source Inverter with Model Predictive Control for Constant Common-Mode Voltage," in *Proc. IPEMC - IEEE ECCE Asia*, pp. 1–6, May 2019.
- J. Yuan, Y. Yang, Y. Shen, **W. Liu**, F. Blaabjerg, and P. Liu, "An Embedded Enhanced-Boost Z-Source Inverter Topology with Fault-Tolerant Capabilities," in *Proc. IEEE IECON*, pp. 3712–3717, Oct. 2018.

- P. Cai, X. Wu, Y. Yang, W. Yao, **W. Liu**, and F. Blaabjerg, "Design of Digital Filter-based Highly Robust Active Damping for LCL-filtered Grid-tied Inverters," in *Proc. IEEE SPEC*, pp. 1–8, Dec. 2018.
- K. A. K. Niazi, Y. Yang, **W. Liu**, and D. Sera, "Sub-Module Level Differential Power Processing for Parallel-Connected Architecture in Photovoltaic Systems," in *Proc. EPE - IEEE ECCE Europe*, pp. 1–9, Sep. 2019.

Part II

Operational Mode Analysis and Modeling of the QZSC

There are two chapters in this part, i.e., ***Chapter 2****. Operational Mode Analysis of the QZSC and* ***Chapter 3****. Interactive Modeling and Stability Analysis of the QZSC.*

2 Operational Mode Analysis of the QZSC

This chapter will discuss the operational modes of the qZSC. Besides the ST state and non-ST state, the load-induced-current (LIC) mode is also investigated in this chapter. To analyze the transformation of these modes, the energy transfer process of the conventional qZSC is provided for parameter consideration and design.

2.1 Introduction

Unlike the conventional buck-type voltage source inverter (VSI), impedance-source inverters (ISIs) can operate in the buck-boost mode when an extra two-port impedance-source network (ISN) is used. The ISN can be considered as a combination of basic passive elements (i.e., inductors, capacitors and coupled inductors) and semiconductor elements (i.e., diodes and switches). Bu using special shoot-through (ST) states, the boost capability of the ISCs can be implemented. However, those ST states should be prohibited in the conventional VSIs, which can lead to short-circuiting. Meanwhile, the adoption of the ST state will not affect the operation of the ac side. Thus, the ISIs can improve the reliability of the inverters to some extent. The ST states can be inserted into the operational modes by modifying the conventional modula-

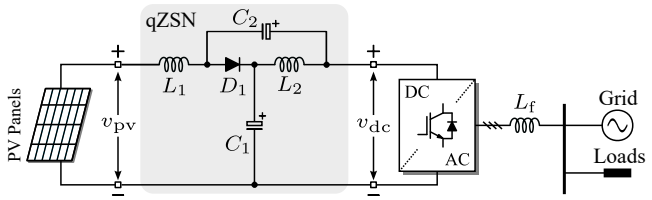

Fig. 2.1: Configuration of a typical three-phase voltage-fed quasi-Z-source inverter system, where v_{pv} is the terminal voltage of the PV panels, and v_{dc} is the terminal voltage of the qZSN.

tion strategies. Additionally, if the input voltage is already large enough to fulfill the requirements from the grid or the load side, the ST states can be "bypassed". Moreover, when the ST duty ratio is zero, the ISIs will also operate in buck mode, which generates the same output voltage similar to that when the VSI operates with the conventional strategies. Therefore, the ISIs are suitable for situations where high boosting capability is essential. e.g., renewable generation systems (PV applications)

Since the introduction of the Z-source inverter (see Fig. 1.3(a)) 8, many ISN topologies have been reported to further improve the boosting gains and reduce the component stresses. For instance, the qZSI inherits the advantages of the conventional Z-source inverter (ZSI) by rearranging the elements, [21] i.e., inductors, capacitors and diodes, and thus it can achieve a high voltage boosting ratio, but also a continuous input current.

Fig. 2.1 shows a typical three-phase qZSI system, in which there are two inductors L_1, L_2, two capacitors C_1, C_2, a diode D_1, a three-phase voltage-fed inverter, and L-type filters, being connected to local loads or the grid. If the inductance and capacitance in the qZSN are ideal to maintain the inductor currents and capacitor voltage constant, which reveals that only three normal operational modes, i.e., ST states, active states and null states, will appear in the continuous conduction mode (CCM) [39, 40]. However, the qZSI system can operate in an undesired operational mode when encountering light loads, low switching frequency or small inductance in the qZSN [41]. For example, the input current may drop to zero when the energy stored in the small inductance is totally released, which will make the qZSI operate in the discontinuous conduction mode (DCM) [35].

Although some of these operational modes are not desired for the qZSI system, those unwanted operational modes should also be analyzed for better system performance by appropriate parameter consideration. Then, in this Ph.D. project, the widely adopted qZSI system is exemplified to explore the operational modes of the ISCs. Thus, besides the typical ST and non-ST states, more operational modes of the qZSI system will be discussed in this chapter. Moreover, the energy transfer process of the qZSI system will be provided for parameter design under different operational modes.

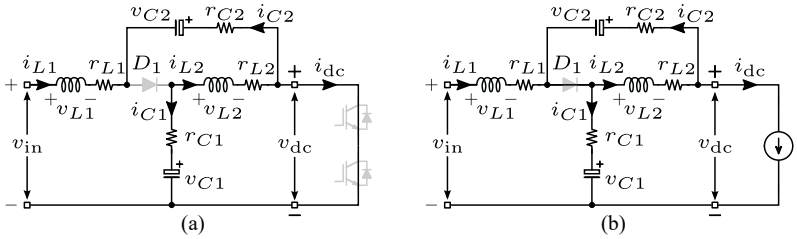

Fig. 2.2: Equivalent circuits of the qZSI during: (a) ST state and (b) non-ST state, where $i_{\rm dc}$ is the equivalent load current of the ac side.

2.2 Operational Modes of the Quasi-Z-Source Converter

2.2.1 ST State and Non-ST State

Generally, the operational modes of the qZSC can be classified into two states [42], i.e., ST state and non-ST state, as shown in Fig. 2.2. According to Fig. 2.2(a), the dynamics of the inductors L_1, L_2, C_1, and C_2 during the ST state can be expressed as

$$\begin{cases} v_{L1} = L_1 \dfrac{di_{L1}}{dt} = v_{\rm in} + v_{C2} - (r_{L1} + r_{C2}) i_{L1} \\ v_{L2} = L_2 \dfrac{di_{L2}}{dt} = v_{C1} - (r_{L2} + r_{C1}) i_{L1} \\ i_{C1} = C_1 \dfrac{dv_{C1}}{dt} = -i_{L2} \\ i_{C2} = C_2 \dfrac{dv_{C2}}{dt} = -i_{L1} \end{cases} \tag{2.1}$$

in which $v_{\rm in}$ is the input voltage, $i_{L1} i_{L2}$ are the inductor currents of L_1 and L_2, v_{C1} and v_{C2} are the capacitor voltages of C_1 and C_2, r_{L1}, r_{L2}, r_{C1}, and r_{C2} represent the equivalent series resistance of the corresponding passive component. The dc-link voltage $v_{\rm dc}$ is zero, and there will be no energy exchange between the qZSN and the ac side.

According to Fig. 2.2(b), the inductors L_1, L_2, C_1, and C_2 during the non-ST state can be given as

$$\begin{cases} v_{L1} = L_1 \dfrac{di_{L1}}{dt} = v_{\rm in} - v_{C1} - (r_{L1} + r_{C1}) i_{L1} + r_{C1} i_{\rm dc} \\ v_{L2} = L_2 \dfrac{di_{L2}}{dt} = -v_{C2} - (r_{L2} + r_{C2}) i_{L2} + r_{C2} i_{\rm dc} \\ i_{C1} = C_1 \dfrac{dv_{C1}}{dt} = i_{L1} - i_{\rm dc} \\ i_{C2} = C_2 \dfrac{dv_{C2}}{dt} = i_{L2} - i_{\rm dc} \end{cases} \tag{2.2}$$

where the sum of v_{C1} and v_{C2} will be the input voltage of the ac side.

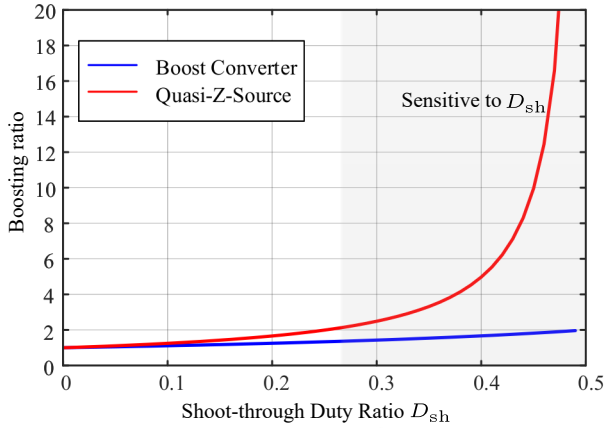

Fig. 2.3: Boosting ratio comparison of the boost converter and the qZSN.

In one switching cycle, the averaging model can be obtained as

$$\begin{cases} L_1\dfrac{di_{L1}}{dt} = v_{\rm in} - (1-d_{\rm sh})v_{C1} + d_{\rm sh}v_{C2} - [d_{\rm sh}(r_{L1}+r_{C2}) \\ \qquad\qquad +(1-d_{\rm sh})(r_{L1}+r_{C1})]i_{L1} + (1-d_{\rm sh})r_{C1}i_{\rm dc} \\ L_2\dfrac{di_{L2}}{dt} = d_{\rm sh}v_{C1} - (1-d_{\rm sh})v_{C2} - [d_{\rm sh}(r_{L2}+r_{C1}) \\ \qquad\qquad +(1-d_{\rm sh})(r_{L2}+r_{C2})]i_{L2} + (1-d_{\rm sh})r_{C2}i_{\rm dc} \\ C_1\dfrac{dv_{C1}}{dt} = (1-d_{\rm sh})(i_{L1}-i_{\rm dc}) - d_{\rm sh}i_{L2} \\ C_2\dfrac{dv_{C2}}{dt} = (1-d_{\rm sh})(i_{L2}-i_{\rm dc}) - d_{\rm sh}i_{L1} \end{cases} \tag{2.3}$$

with $d_{\rm sh}$ being the ST duty ratio. Accordingly, ignoring the internal equivalent resistances r_L and r_C, the steady-state values can be obtained by using the volt-sec balance on the inductor currents and amp-sec balance on the capacitor voltages as

$$\begin{aligned} V_{C1} &= \frac{1-D_{\rm sh}}{1-2D_{\rm sh}}V_{\rm in}, \quad I_{L1} = I_{L2} = \frac{1-D_{\rm sh}}{1-2D_{\rm sh}}I_{\rm dc}, \\ V_{C2} &= \frac{D_{\rm sh}}{1-2D_{\rm sh}}V_{\rm in}, \quad V_{\rm dc} = \frac{1}{1-2D_{\rm sh}}V_{\rm in}, \end{aligned} \tag{2.4}$$

where $V_{\rm in}$, V_{C1}, V_{C2}, $V_{\rm dc}$, I_{L1}, I_{L2}, $I_{\rm dc}$, and $D_{\rm sh}$ are the steady-state values of the input voltage $v_{\rm in}$, the capacitor voltages v_{C1}, v_{C2}, the peak dc-link voltage, the inductor currents i_{L1}, i_{L2}, the equivalent load current $i_{\rm dc}$, and the ST duty ratio $d_{\rm sh}$. Then, the boosting ratio of the qZSN can be obtained as

$$B = \frac{1}{1-2D_{\rm sh}} \tag{2.5}$$

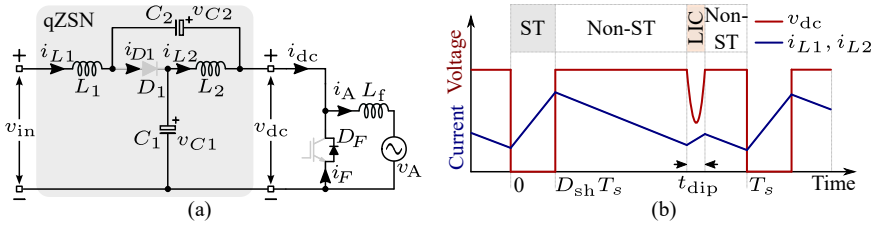

Fig. 2.4: Load-induced-current mode of the qZSI: (a) equivalent circuit, and (b) typical switching waveforms of the inductor current i_L and dc-link voltage v_{dc}, in which i_F is the freewheeling current, i_A and v_A is the equivalent output current and voltage, and t_{dip} is the dip duration of the LIC mode.

The boosting ratio comparison of the boost converter and the qZSN is presented in Fig. 2.3. As shown in Fig. 2.3, the boost ratio of the qZSN with the same duty ratio is higher than that of the boost converter. However, it is also seen in Fig. 2.3 that the qZSI is more sensitive to the input voltage and duty ratio variations when compared with the boost converter. It is thus necessary to model the qZSN under different operation modes to tolerate large variations in the input condition and the duty ratio.

2.2.2 Load-Induced-Current (LIC) Mode

The load-induced-current (LIC) mode will be triggered when the energy provided by the qZSN side is not sufficient for the load side, as shown in Fig. 2.4(a). Generally, the LIC mode will appear when the system changes from other states to the active states. When the LIC mode occurs, the freewheeling diode, e.g., D_F in Fig. 2.4(a), will enter the freewheeling condition for the load current. The LIC mode shows the feature of the ST state, which is undesired, as observed in Fig. 2.4(b). Similarly, the diode D_1 will be blocked, and the energy will be transferred to the inductors during the LIC mode. The inductor current i_L under the LIC mode will increase and remain positive, while the dc-link voltage will drop significantly, as shown in Fig. 2.4(b).. During the LIC mode, the freewheeling current i_F will decrease with the increase of the inductor current. When the freewheeling current i_F reaches zero, the qZSI system will switch from the LIC mode to another state immediately [41], as shown in Fig. 2.4(b). The LIC mode can not be controlled, and the duration is very short when compared to the normal ST states. The LIC mode will end when the relationship between inductor current i_L, dc-link current i_{dc} and output current i_A meets

$$i_A < i_{dc} = 2i_L \tag{2.6}$$

As an uncontrollable and unpredictable mode, the LIC mode is very short, which shows a negligible effect on the output quality.

2.2.3 Discontinuous Conduction Mode (DCM)

The CCM can be analyzed similarly to the ST and non-ST states. When considering the discontinuous conduction mode (DCM), there will be a discontinuous state introduced, affecting the steady-state feature [35, 43]. Thus, the ST duty ratio d_{sh}, non-ST duty ratio d_n and discontinuous duty ratio d_d will be used in the DCM. The sum of d_{sh}, d_n and d_d is expressed as

$$d_{\text{sh}} + d_n + d_d = 1 \tag{2.7}$$

The average model of the qZSI in the DCM is presented as

$$\begin{cases} L_1 \dfrac{di_{L1}}{dt} = d_n(v_{\text{in}} - v_{C1}) + d_{\text{sh}}(v_{\text{in}} + v_{C2}) + d_d \cdot 0 \\ L_2 \dfrac{di_{L2}}{dt} = d_{\text{sh}} v_{C1} - d_n v_{C2} + d_d \cdot 0 \end{cases} \tag{2.8}$$

Then, the steady-state capacitor voltages in the DCM can be obtained as

$$V_{C1} = \frac{1 - D_{\text{sh}}}{1 - 2D_{\text{sh}} - D_d} V_{\text{in}}, \quad V_{C2} = \frac{D_{\text{sh}} - D_d}{1 - 2D_{\text{sh}} - D_d} V_{\text{in}} \tag{2.9}$$

where D_s, D_n and D_d are the steady-state values of d_{sh}, d_n and d_d, respectively. The peak dc-link voltage can be described as

$$V_{\text{dc}} = V_{C1} + V_{C2} = \frac{1 - D_d}{1 - 2D_{\text{sh}} - D_d} V_{\text{in}} \tag{2.10}$$

which is larger than that in the CCM with the same system parameters. When i_L reaches zero, the dc-link voltage v_{dc} will be identical to v_{C1}.

As a lossless system, the following relationship can be obtained as

$$V_{\text{in}} I_{\text{in}} = (1 - D_{\text{sh}} - D_n) V_{\text{dc}} I_{\text{dc}} = V_{C1} I_{\text{dc}} \tag{2.11}$$

with the variables defined previously.

Then, in the DCM, the average inductor current can be expressed as

$$I_L = \frac{I_{\text{dc}}}{2} + \frac{V_{C1} D_{\text{sh}}^2}{2Lf_s} \left(\frac{2V_{C1} - V_{\text{in}}}{V_{C1} - V_{\text{in}}} \right) \tag{2.12}$$

where f_s is the switching frequency. Accordingly, a coefficient is defined as

$$\frac{V_{C1} D_{\text{sh}}^2}{V_{C1} - V_{\text{in}}} = \frac{I_{\text{dc}} L f_s}{V_{\text{in}}} = a \Rightarrow V_{C1} = \frac{a}{a - D_{\text{sh}}^2} V_{\text{in}} \tag{2.13}$$

in which a should be larger than D_{sh}^2. Then, the boundary for the CCM and the DCM is shown in Fig. 2.5.

To avoid the unwanted operational modes, the critical parameters should be derived. Thus, the energy transfer process of an exemplified qZSI system will be used to obtain the critical parameters. This will be presented in the following section.

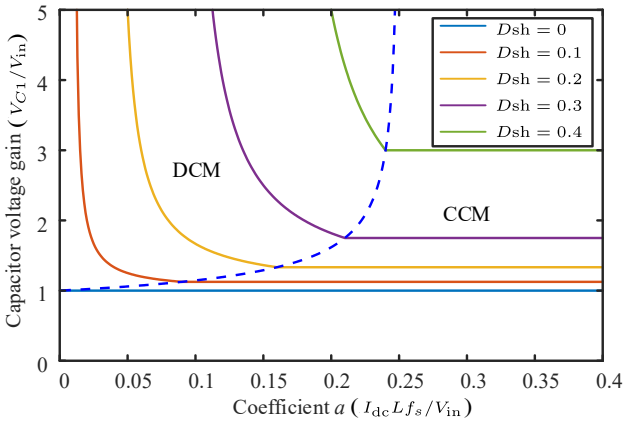

Fig. 2.5: Capacitor voltage ratio under the CCM and DCM considering the coefficient a.

2.3 Energy Transfer Process Analysis

The ac side of the qZSI can be replaced by a controlled current source or a resistor load to be regarded as a dc-dc converter [44]. As shown in Fig. 2.6, there are several operational modes in the quasi-Z-source (qZS) dc-dc converter when considering different system parameters. In an ideal situation with ideal system parameters, the equivalent circuits when the switch S is ON and OFF are shown in Figs. 2.6(a) and (b). The equivalent circuit is identical when the switch S is ON with different system parameters. However, the parameters such as the input voltage, duty cycle, and the inductance in the qZSN will affect the energy transfer process of the qZS dc-dc converter when the switch S is OFF, as shown in Figs. 2.6(b) and (c). Generally, the operational modes of the qZS dc-dc converter can be divided into the CCM and DCM. However, if the energy in the inductors is not enough to supply the load side in the CCM when the switch S is OFF, a new energy transfer mode called the incomplete inductor supply CCM (IISM-CCM) will appear, which is similar to the LIC mode in the qZSI. Then, the CCM can be divided into a complete inductor supply CCM (CISM) and an IISM-CCM [45, 46].

To obtain the critical inductances L_c and L_k between the CISM-CCM, IISM-CCM and DCM, the average inductor current I_L, and the inductor current ripple Δi_L are given as

$$I_L = \frac{I_O V_O}{V_{in}}, \quad \Delta i_L = \frac{V_{C1} D\text{sh}}{2Lf_s} \tag{2.14}$$

where V_O and I_O are the average values of the output variables i_O and i_O.

The critical inductance L_k between the CISM-CCM and IISM-CCM can be obtained when the minimum dc-link current $i_{dcl} = I_O$, and then, l_k is obtained as

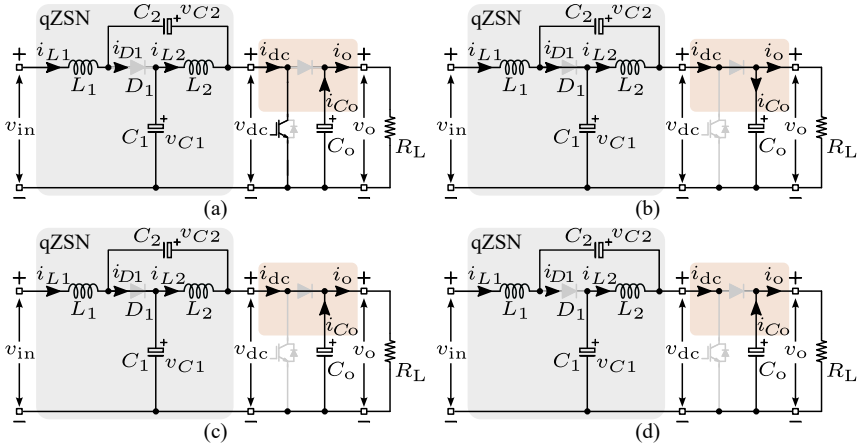

Fig. 2.6: Equivalent circuits of the qZS dc-dc converter in different operational modes when: (a) the switch S is ON, (b) the switch S is OFF and $i_{\rm dcl} \geq i_{\rm O}$, (c) the switch S is OFF and $0 < i_{\rm dcl} < i_{\rm O}$ and (d) the switch S is OFF and $i_{\rm dcl} = 0$, where $i_{\rm dcl}$ is the minimum value of the dc current $i_{\rm dc}$, $v_{\rm O}$ is the output voltage, $i_{\rm DC}$ is the virtual dc current for analysis, and $i_{\rm O}$ is the load current.

$$i_{L\,\min} = I_L - \frac{1}{2}\Delta i_L = I_{\rm O} \Rightarrow L_k = \frac{V_{\rm in} V_{\rm C1} R_L D}{4 f_s (V_O^2 - V_{\rm in} I_{\rm O} R_L)} \tag{2.15}$$

The critical inductance L_c between the CISM-CCM and IISM-CCM is obtained when $i_{\rm DCL} = 0$, and then, l_c is then obtained as

$$i_{L\,\min} = I_L - \frac{1}{2}\Delta i_L = 0 \Rightarrow L_c = \frac{V_{\rm in} V_C R_L D}{4 f_s V_O^2} \tag{2.16}$$

To verify the theoretical analysis, experimental tests are performed on a qZS dc-dc converter, referring to Fig. 2.6. Table 2.1 shows the parameters of the qZS dc-dc converter. According to the above, the critical inductances L_k and L_c are calculated as 240 uH and 600 uH, respectively. Three inductance values are considered for the verification of the CISM-CCM, IISM-CCM and DCM. Fig. 2.7 show the experimental results under the CISM-CCM, IISM-CCM and DCM, respectively, when the inductances are chosen as 160 uH, 275 uH and 760 uH.

As shown in Fig. 2.7(a), when the inductance is 760 uH, the converter operates in the CISM-CCM. The minimum dc-link current $i_{\rm dcl}$ is larger than the load current $i_{\rm O}$, as shown in Fig. 2.7(a). The peak of $v_{\rm dc}$ is 50 V and the voltage of the capacitor C_1 is 40 V in the experimental results. When the switch S is ON, $i_{\rm dc}$ is equal to two times of the inductor current i_L. During this mode, the inductor current ripple is small enough to make the converter operate with good performance. Increasing the inductance can further reduce the inductor current ripple, but the transient response will be affected.

Table 2.1: Parameters of the qZSI for model verification.

Parameter	Value
Input voltage v_{in}	30 V
Capacitors in the qZSI C_1, C_2	400 uF
Output capacitor C_{O}	2200 uF
Load resistor R_L	10 kHz
Switching frequency f_s	400 uF
Shoot-through duty cycle D	0.2
Inductors L_1, L_2 in the qZSI for CISM-CCM	760 uH
Inductors L_1, L_2 in the qZSI for IISM-CCM	275 uH
Inductors L_1, L_2 in the qZSI for DCM	160 uH

The performance of the qZS dc-dc converter in the CCM-IISM is shown in Fig. 2.7(b) when the inductance is 275 uH. During the CCM-IISM, the minimum DC-link current i_{dcl} is smaller than the load current i_{O}. When i_{DC} becomes smaller than i_{O}, the output capacitor C_{O} starts to release energy to keep the output voltage v_{O} constant as the peak of v_{dc} (see, Fig. 2.7(b)). The voltage ripple of C_1 is the same as that during the CISM-CCM, which is independent of the inductance in a control cycle. The inductor current ripple becomes larger while the other parameters are the same.

The DCM appears when the inductance is further reduced to 160 uH, as shown in Fig. 2.7(c). During the DCM, the minimum dc-link current i_{dcl} is equal to zero. There will be no energy exchange between the inductors and the capacitors when the inductor current i_L reaches zero, as demonstrated in Fig. 2.7(c). If there is no energy transferred inside the qZS network, which means v_{DC} equals to v_{C1}. The DCM makes the energy from the source that cannot be absorbed by the inductors be transferred to the capacitors, which in turn increases the equivalent switch-on time and the peak DC-link voltage. There is an apparent voltage drop in the DC-link voltage when the switch is OFF (i.e., T_{off} period) during the DCM, which verified the analysis.

2.4 Summary

In this chapter, the operational modes of the qZSI are analyzed and discussed in addition to the conventional ST and non-ST states. This includes the LIC mode and DCM mode. Then, the energy transfer process of a sim-

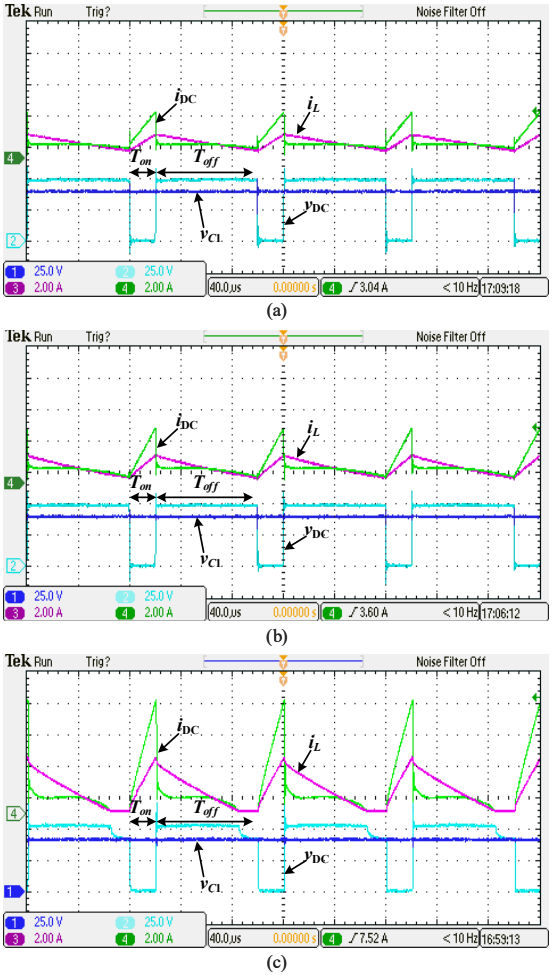

Fig. 2.7: Experimental results of a 50-W qZS dc-dc converter operating with a constant duty ratio: capacitor voltage V_{C1}, DC-link voltage v_{DC}, inductor current i_L and DC-link current i_{DC} when the converter operates in (a) CISM-CCM, (b) IISM-CCM and (c) DCM. (CH1/CH2-capacitor voltage V_{C1}/DC-link voltage v_{DC} [25 V/div], CH3/CH4-inductor currenti_L/ DC-link current i_{DC} [5 A/div], and time [40 us/div]).

ple qZSN (i.e., a qZS dc-dc converter) considering the critical inductances between the CISM-CCM, IISM and DCM is derived and analyzed. Then, the theoretical analysis was verified by experimental tests. It can be concluded from the discussions that the qZSN can have different operational modes which may in term affect the operation of the entire inverter system (e.g., the stability of the qZSI). The identified critical inductances can be used in the design phase of qZSI-based PV systems to ensure stable operation.

3 Interactive Modeling and Stability Analysis of the QZSC

This chapter presents the interactive small-signal modeling and stability analysis for the three-phase qZSI-based system. According to the interactive models, the effect of the ISN on the ac-side control system is then investigated. The resonance that is resulted from the operational conditions has been explored to enhance the controller design of the entire qZSI system.

3.1 Introduction

By introducing the ISN, the qZSI (see Fig. 2.1) can make use of the ST state to regulate the dc-link voltage under a wide input range. The ST state is inserting into the conventional zero states of the inverter, making the dc-link voltage v_{dc} in Fig. 2.1 varying (pulsating) [47–49]. Although the qZSI is a single-stage structure, it is controlled like a two-stage inverter, which contains two control variables, modulation index m and ST duty ratio d_{sh}. However, the dc-link capacitor C_{dc} in Fig. 1.2 can decouple the dc-dc converter and the inverter in the two-stage structure, enabling those two parts controlled separately. Thus, the qZSN and the inverter are coupled deeply in the qZSI system, challenging the design of the control system for the qZSI system.

With direct control, i.e., special measuring circuit, or indirect control, e.g., control the capacitor voltage, the control system for the qZSI is presented in Fig. 1.5. However, the extra inductors and capacitors in the qZSN introduce resonant issues in the qZSi system. In [17, 50], the non-minimum-plane (NMP) and right-half phase (RHP) zero resulted from the ISN have been discussed. The output impedance of the ZSI has been investigated on the uninterrupted power supply (UPS) for the controller design. A voltage feed-forward controller was presented in [51] to tackle the issues that come from the variation of the operational conditions. In [52], a damping compensator was proposed to address the stability issue in the ZSI system. The high-frequency LCL features of the qZSN were investigated in [53]. In [54], the circuit-averaging strategy was adopted to explore the instability phenomenon triggered by the operational conditions.

Thus, this chapter focuses on how the ISN affects the system dynamics (more specifically, the control of the inverter part) for the qZSI system. The small-signal modeling for the qZSN will be derived first. Then, based on the obtained qZSN models, the interactive small-signal models of the qZSI system can be obtained. The ac-side controller is subsequently designed by considering the impact of the ISN on the inverter-side system stability. Finally, simulations and experimental results have been provided to verify the obtained theoretical analysis on a three-phase qZSI.

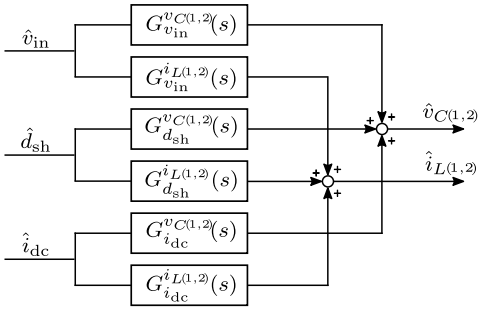

Fig. 3.1: Small-signal transfer functions of the qZSN.

3.2 Small-Signal Modeling of the QZSN

The small-signal models of the qZSN are derived in this section to explore the dynamics of the qZSN. The most popular modeling methods are state-space averaging methods, and circuit averaging methods [55].. These methods normally separate the impedance part and the inverter part, and make the inverter part equivalent to a current load or a simple LC load, i.e, $i_{\rm dc}$ in Fig. 2.2. For simplicity, referring to Fig. 2.1, it is assumed that $L_1 = L_2 = L$, $C_1 = C_2 = C$, $r_{L1} = r_{L2} = r_L$, and $r_{C1} = r_{C2} = r_C$. The linear model can be obtained around a chosen steady-state operating point. By substituting $x = X + \hat{x}$, (where X and $\hat{x}$ are steady-state terms and perturbations of the corresponding variables x = $d_{\rm sh}$, $v_{\rm in}$, $i_{\rm dc}$, $v_{C(1,2)}$, $i_{L(1,2)}$ in (2.3), the small-signal models of the qZSN can be expressed as

$$
\begin{cases}
sL\hat{i}_{L1} = \hat{v}_{\rm in} - (1-D_{\rm sh})\hat{v}_{C1} + D_{\rm sh}\hat{v}_{C2} - (r_L + r_C)\hat{i}_{L1} \\
\qquad +(V_{C1} + V_{C2} - r_C I_{\rm dc})\hat{d} + (1-D_{\rm sh})r_C\hat{i}_{\rm dc} \\
sL\hat{i}_{L2} = D_{\rm sh}\hat{v}_{C1} - (1-D_{\rm sh})\hat{v}_{C2} - (r_L + r_C)\hat{i}_{L2} \\
\qquad +(V_{C1} + V_{C2} - r_C I_{\rm dc})\hat{d} + (1-D_{\rm sh})r_C\hat{i}_{\rm dc} \\
sC\hat{v}_{C1} = (1-D_{\rm sh})\hat{i}_{L1} - D_{\rm sh}\hat{i}_{L2} - (1-D_{\rm sh})\hat{i}_{\rm dc} \\
\qquad +(I_{\rm dc} - I_{L1} - I_{L2})\hat{d} \\
sC\hat{v}_{C2} = -D_{\rm sh}\hat{i}_{L1} + (1-D_{\rm sh})\hat{i}_{L2} - (1-D_{\rm sh})\hat{i}_{\rm dc} \\
\qquad +(I_{\rm dc} - I_{L1} - I_{L2})\hat{d}
\end{cases}
\tag{3.1}
$$

As shown in Fig. 3.1, the small-signal models can be obtained, i.e., $G_{v_{\rm in}}^{v_{C(1,2)}}(s)$, $G_{d_{\rm sh}}^{v_{C(1,2)}}(s)$, $G_{i_{\rm dc}}^{v_{C(1,2)}}(s)$, $G_{v_{\rm in}}^{i_{L(1,2)}}(s)$, $G_{d_{\rm sh}}^{i_{L(1,2)}}(s)$ and $G_{i_{\rm dc}}^{i_{L(1,2)}}(s)$. The transfer functions from $d_{\rm sh}$ to the inductor currents i_{L1} and i_{L2} are identical as $G_{d_{\rm sh}}^{i_L}(s)$, and the transfer function from $d_{\rm sh}$ to the capacitor voltages v_{C1} and v_{C2} are also identical as $G_{d_{\rm sh}}^{v_C}(s)$. The detailed transfer functions can be obtained as

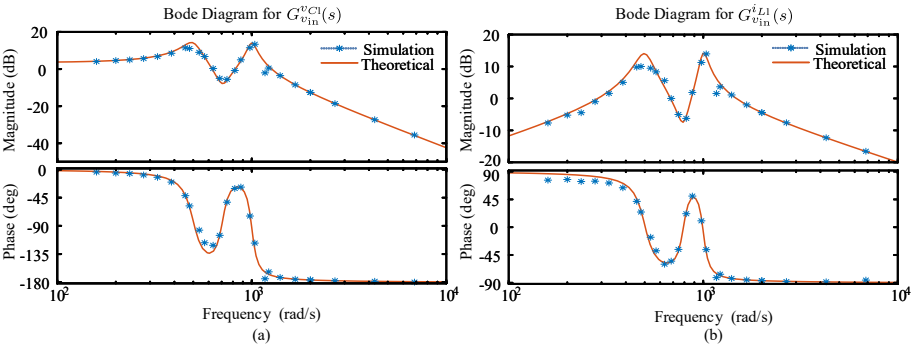

Fig. 3.2: The theoretical transfer functions and frequency response of the qZSN for $G_{v_{in}}^{v_{C1}}(s)$ and $G_{v_{in}}^{i_{L1}}(s)$ [56].

$$G_{d_{sh}}^{i_L}(s) = \frac{(V_{C1}+V_{C2}-r_C I_{dc})Cs-(1-2D_{sh})(I_{dc}-I_{L1}-I_{L2})}{LCs^2+C(r_L+r_C)s+(1-2D_{sh})^2} \tag{3.2}$$

$$G_{d_{sh}}^{v_C}(s) = \frac{(I_{dc}-I_{L1}-I_{L2})(Ls+r_L+r_C)+(1-2D_{sh})(V_{C1}+V_{C2}-r_C I_{dc})}{LCs^2+C(r_L+r_C)s+(1-2D_{sh})^2} \tag{3.3}$$

$$G_{i_{dc}}^{i_L}(s) = \frac{(1-D_{sh})r_C Cs+(1-2D_{sh})(1-D_{sh})}{LCs^2+C(r_L+r_C)s+(1-2D_{sh})^2} \tag{3.4}$$

$$G_{i_{dc}}^{v_C}(s) = \frac{-(1-D_{sh})Ls-(1-D_{sh})(2Dr_C+r_L)}{LCs^2+C(r_L+r_C)s+(1-2D_{sh})^2} \tag{3.5}$$

$$G_{v_{in}}^{v_{C1}} = \frac{(1-D_{sh})LCs^2+(1-D_{sh})(r_C+r_L)Cs+(1-D_{sh})(1-2D_{sh})}{[LCs^2+C(r_L+r_C)s+(1-2D_{sh})^2][LCs^2+C(r_L+r_C)s+1]} \tag{3.6}$$

$$G_{v_{in}}^{i_{L1}} = \frac{[LCs^2+(r_C+r_L)Cs+(1-D_{sh})^2+{D_{sh}}^2]Cs}{[LCs^2+C(r_L+r_C)s+(1-2D_{sh})^2][LCs^2+C(r_L+r_C)s+1]} \tag{3.7}$$

The theoretical transfer functions and frequency response of the qZSN for $G_{v_{in}}^{v_{C1}}(s)$ and $G_{v_{in}}^{i_{L1}}(s)$ are shown in Fig. 3.2, which can verify the obtained small-signal models. The small-signal models can be taken to explore the dynamics of qZSN under system parameter variations. Considering the variation of the inductance L, capacitance C, equivalent resistance r_L, r_C, and ST duty ratio D_{sh}, the transfer function $G_{d_{sh}}^{v_C}(s)$ from the duty ratio to the capacitor voltage is exemplified, which is shown in Fig. 3.3. As observed in Fig. 3.3, there are right-half plane (RHP) zeros in the transfer functions, which indicates the presence of the non-minimum phase (NMP) undershoot. When the input voltage increases, the dynamic capacitor voltage will drop first, and then, it

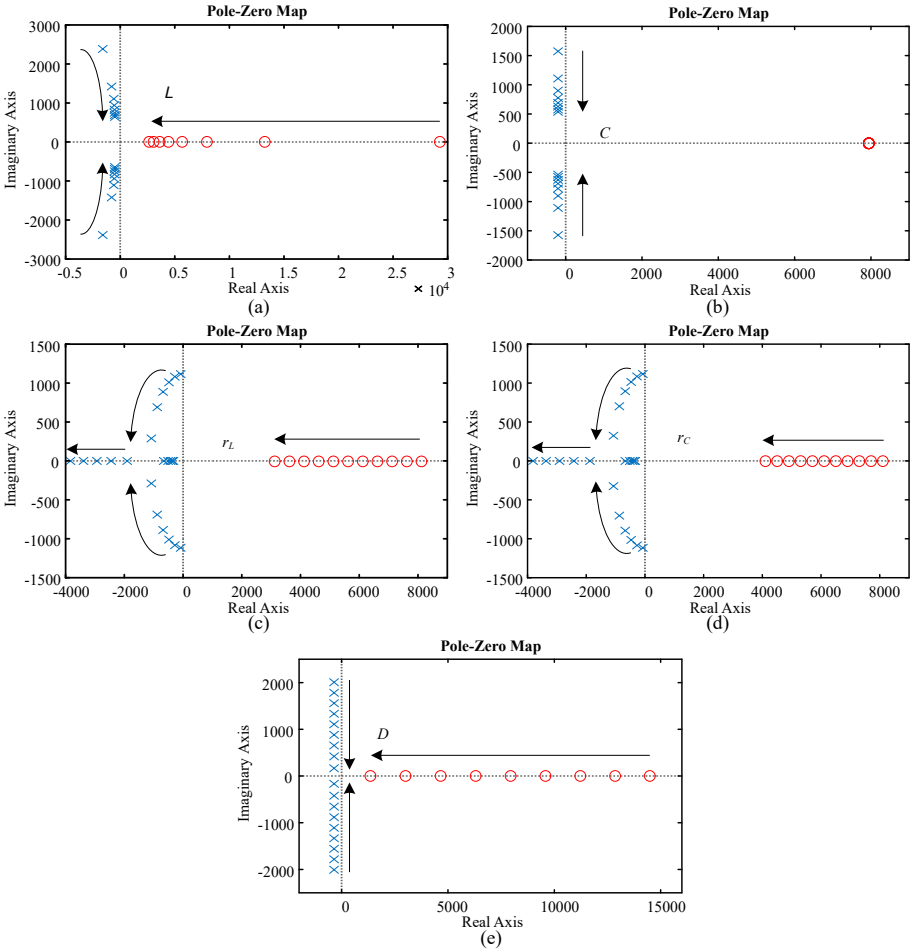

Fig. 3.3: Pole-zero map of $G_{d_{\text{sh}}}^{v_C}(s)$ with varying (a) inductance L, (b) capacitance C, (c) equivalent resistance of inductor r_L, (d) equivalent resistance of capacitor r_C, and (e) shoot-through duty ratio D_{sh}.

will continue to rise. When L increases, the degree of the NMP undershoot and the settling time also increases with the zeros and the conjugated poles moving toward the origin, as shown in Fig. 3.3(a). With the increase of C, the impact on the NMP undershoot is negligible, while the settling time rises, as shown in Fig. 3.3(b). Furthermore, with respect to the equivalent resistances of the passive components, as presented in Figs. 3.3(c) and (d), the increase of the equivalent resistance r_L or r_C will increase the degree of the NMP undershoot and system damping ratio simultaneously [57]. Fig. 3.3(e) implies that the effect of the ST duty ratio D_{sh} variation on the dynamics of the capacitor voltage is along with the variation of C.

3.3 Interactive Modeling of the QZSN and the Inverter

As mentioned previously, the controllers for the qZSN and the inverter are designed separately, which is similar to the two-stage structure [58, 59]. To investigate how the ISN affects the system dynamics, the interactive models of the qZSI system should be derived in detail. As presented in the previous section, the inverter is equivalent to a controlled current source, which can affect the dynamics of the qZSN. For the ac side, v_{dc} is the input voltage of the inverter part, which is also the output voltage of the qZSN during the non-ST state. Then, the inverter dynamic is inevitably affected by the variation of the peak dc-link voltage V_{dc} [12]. Thus, how the dc-link voltage variation affects the inverter dynamic will be explored in this section.

For simplicity, the following relationships are defined:

$$\begin{cases} v_{Csum} = v_{C1} + v_{C2} \\ i_{Lsum} = i_{L1} + i_{L2} \end{cases} \tag{3.8}$$

in which v_{Csum} is equal to v_{dc}. Accordingly, the small-signal models in Fig. 3.1 can be updated as

$$\begin{cases} \hat{v}_{Csum} = G_{v_{\mathrm{in}}}^{v_{Csum}}(s)v_{\mathrm{in}} + G_{d_{\mathrm{sh}}}^{v_{Csum}}(s)d_{\mathrm{sh}} + G_{i_{\mathrm{dc}}}^{v_{Csum}}(s)i_{\mathrm{dc}} \\ \hat{i}_{Lsum} = G_{v_{\mathrm{in}}}^{i_{Lsum}}(s)v_{\mathrm{in}} + G_{d_{\mathrm{sh}}}^{i_{Lsum}}(s)d_{\mathrm{sh}} + G_{i_{\mathrm{dc}}}^{i_{Lsum}}(s)i_{\mathrm{dc}} \end{cases} \tag{3.9}$$

where

$$\begin{cases} G_{v_{\mathrm{in}},\, d_{\mathrm{sh}},\, i_{\mathrm{dc}}}^{v_{Csum}}(s) = G_{v_{\mathrm{in}},\, d_{\mathrm{sh}},\, i_{\mathrm{dc}}}^{v_{C1}}(s) + G_{v_{\mathrm{in}},\, d_{\mathrm{sh}},\, i_{\mathrm{dc}}}^{v_{C2}}(s) \\ G_{v_{\mathrm{in}},\, d_{\mathrm{sh}},\, i_{\mathrm{dc}}}^{i_{Lsum}}(s) = G_{v_{\mathrm{in}},\, d_{\mathrm{sh}},\, i_{\mathrm{dc}}}^{i_{L1}}(s) + G_{v_{\mathrm{in}},\, d_{\mathrm{sh}},\, i_{\mathrm{dc}}}^{i_{L2}}(s) \end{cases} \tag{3.10}$$

Assuming the system is lossless, the inverter part can be simplified as

$$\begin{cases} V_{\mathrm{o}} = MV_{dc} = Mv_{Csum} \\ I_{\mathrm{o}} = \dfrac{1-2D_{\mathrm{sh}}}{M} I_{Lsum} \end{cases} \tag{3.11}$$

where V_{o} and I_{o} are the root mean square (RMS) values of the inverter output voltage and current, and M is the steady-state value of the modulation index m. Then, considering the small variations $\hat{v}_{\mathrm{o}}$, $\hat{i}_{\mathrm{o}}$ and $\hat{m}$, the corresponding small-signal models can be obtained from (3.11) as

$$\begin{cases} \hat{v}_{Csum} = \dfrac{1}{M}\hat{v}_{\mathrm{o}} - \dfrac{V_{in}}{(1-2D_{\mathrm{sh}})M}\hat{m} \\ \hat{i}_{\mathrm{o}} = \dfrac{1-2D}{M}\hat{i}_{Lsum} - \dfrac{2I_{\mathrm{o}}}{1-2D_{\mathrm{sh}}}\hat{d}_{\mathrm{sh}} - \dfrac{I_{\mathrm{o}}}{M}\hat{m} \end{cases} \tag{3.12}$$

Referring to (3.9), $\hat{v}_{Csum}$ can be rewritten as

$$M\hat{v}_{Csum} = G_1\hat{v}_{\mathrm{in}} + G_2\hat{d}_{\mathrm{sh}} + M^2 G_{i_{\mathrm{dc}}}^{v_{Csum}}(s)\frac{1-2D_{\mathrm{sh}}}{M}\hat{i}_{Lsum} \tag{3.13}$$

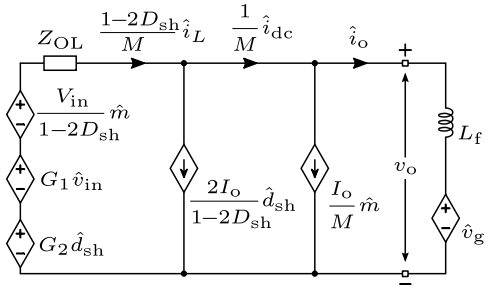

Fig. 3.4: Equivalent small-signal circuit of the qZSI considering the coupling between the qZSN and the inverter part, in which Z_{OL} is the open-loop impedance.

in which

$$\begin{cases} G_1 = MG_{v_{\mathrm{in}}}^{v_{Csum}}(s) \\ G_2 = MG_{d_{\mathrm{sh}}}^{v_{Csum}}(s) - \dfrac{2M^2 I_{\mathrm{o}}}{1-2D} G_{i_{\mathrm{dc}}}^{v_{Csum}}(s) \end{cases} \tag{3.14}$$

Thus, the open-loop impedance resulted from the impedance network can be obtained as

$$Z_{OL} = -M^2 G_{i_{\mathrm{dc}}}^{v_{Csum}}(s) = \frac{2(1-D_{\mathrm{sh}})LM^2 s}{LCs^2 + (1-2D_{\mathrm{sh}})^2} \tag{3.15}$$

in which the negative sign reflects the current direction, and $G_{i_{\mathrm{dc}}}^{v_{Csum}}(s)$ can be obtained by neglecting the equivalent resistors r_L and r_L as

$$G_{i_{\mathrm{dc}}}^{v_{Csum}}(s) = \frac{-2(1-D_{\mathrm{sh}})Ls}{LCs^2 + (1-2D_{\mathrm{sh}})^2} \tag{3.16}$$

According to (3.9) and (3.12), the equivalent interactive small-signal circuit of the qZSN and the inverter is presented in Fig. 3.4. As shown in Fig. 3.4, the output dynamics are affected by the variation of the ST duty ratio d_{sh}, input voltage v_{in} and modulation index m. To explore the transient response of the inverter, v_{Csum} is assumed constant under different input conditions. Then, the obtained interactive models can be used to analyze the effect of the ISN on the dynamics of the inverter for controller design.

3.4 Effect on the System Dynamics and Controller Design

The typical control system for the three-phase qZSI is presented in Fig. 3.5. v_{dc} in Fig. 2.1 is the input voltage for the inverter, which is pulsating. With a special sensor circuit, the peak v_{dc} can be controlled, which increases the cost of the entire system. Then, indirect control methods, e.g., control the capacitor voltage in the qZSN, can be another solution. The dc-link controller

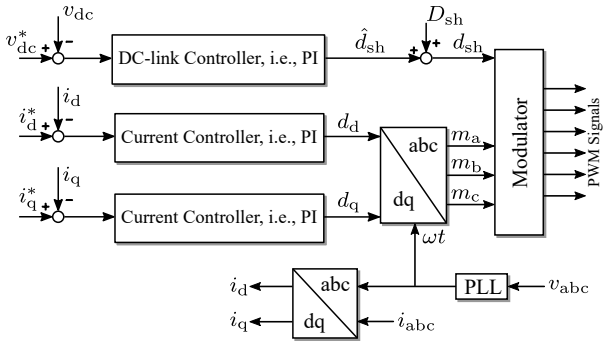

Fig. 3.5: The two-stage control system for the three-phase qZSI system, in which i_d, i_q, i^*_d, i^*_q, d_d, d_q are the currents, corresponding references, modulation ratios on the dq-axis, m is the modulation index, i_{abc} and v_{abc} are the output current and voltage (PLL - Phase Locked Loop). Here, PWM signals are the switching signals for the VSI.

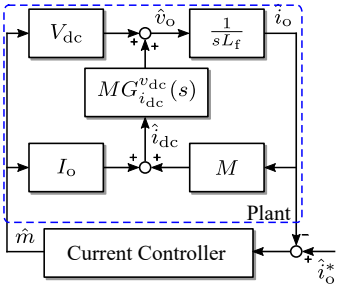

Fig. 3.6: The ac-side plant models considering the effect of the qZSN according to (3.9) and (3.12).

is a Proportional Integral (PI) controller, and the control parameter can be obtained according to the system model $G^{v_{C1}}_{d_{sh}}(s)$ [15, 60]. This section will discuss the effect of the ISN on the ac-side controller, and the qZSN will remain open-loop and maintain a constant peak v_{dc} by defining appropriate input conditions. The ac-side controller for the qZSI is the same as that for the conventional VSI, i.e., the PI controller in Fig. 3.5, and then, the PI controller can then be obtained as

$$G_{PI}(s) = k_p + \frac{k_i}{s} \tag{3.17}$$

with k_p and k_i being the controller parameters.

According to (3.9) and (3.12), the ac-side plant model with the effect of the qZSN is illustrated in Fig. 3.6, in which the variation of the peak dc-link voltaeg, i.e., $G^{v_{dc}}_{i_{dc}}(s)$, is considered. Then, the open-loop transfer function for the ac side can be expressed as

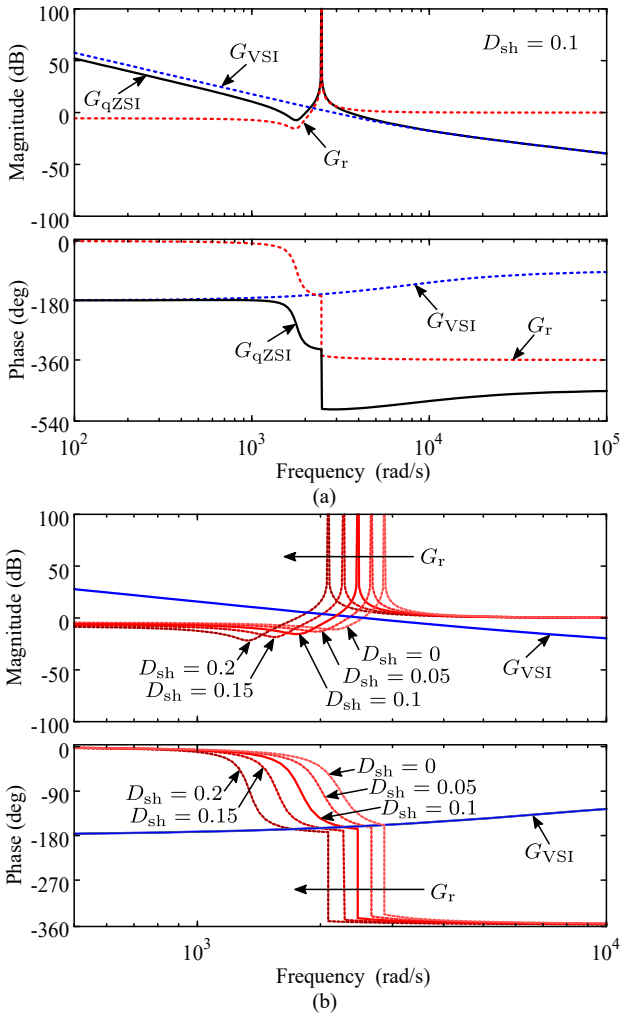

Fig. 3.7: Open-loop Bodes of: (a) Open-loop Bode of $G_{\rm qZSI}$, $G_{\rm VSI}$ and $G_{\rm r}$ with $D_{\rm sh} = 0.1$, and (b) $G_{\rm VSI}$ and $G_{\rm r}$ with the ST ratio $D_{\rm sh}$ varying from 0 to 0.2.

$$G_{\rm qZSI}(s) = \underbrace{G_{\rm PI}\frac{V_{\rm DC}}{L_f s}}_{G_{\rm VSI}} \underbrace{\frac{s^2 - \frac{2LI_{\rm o}M(1-D_{\rm st})}{LCV_{\rm DC}}s + \frac{(1-2D_{\rm st})^2}{LC}}{s^2 + \frac{2LM^2(1-D_{\rm st})}{LCL_f} + \frac{(1-2D_{\rm st})^2}{LC}}}_{G_{\rm r}} \tag{3.18}$$

in which $G_{\rm qZSI}$ and $G_{\rm VSI}$ are the open-loop transfer functions for the ac side of the qZSI system and the VSI system, and $G_{\rm r}$ is the transfer function that can represent from the qZSN.

Table 3.1: Parameters of the qZSI System (Fig. 2.1).

Parameter	Symbol	Value
Inductors in the qZSN	$L_1 = L_2 = L$	750 μH
Capacitors in the qZSN	$C_1 = C_2 = C$	200 μF
Output filter	L_f	1.8 mH
Output frequency	f_s	50 Hz
Load impedance	R_o	10 Ω
PI controller under unstable condition	k_p, k_i	0.4, 20
PI controller under stable condition	k_p, k_i	0.08, 3

The corresponding Bode plots of G_{qZSI}, G_{VSI} and G_r are illustrated in Fig. 3.7(a). As shown in Fig. 3.7(a), the phase margin of the ac-side controller for the qZSI is decreased by the transfer function G_r, when compared with that of G_{VSI}. Thus, the ac-side controller should not be designed exactly the same as the conventional VSI. The phase margin of qZSI should consider the effect of G_r for system stability. Meanwhile, G_r is affected by the input conditions, e.g., the ST duty ratio D_{sh}, which in turn affect the dynamics of the ac-side controller, as shown in Fig. 3.7(b). With the increase of D_{sh}, the qZSI system becomes unstable with the parameters designed with a small D_{sh}. Then, the resonant frequency ω_r when the qZSI system is unstable can be obtained as

$$\omega_r = \sqrt{\frac{2LM^2(1-D_{\mathrm{st}})}{LCL_f} + \frac{(1-2D_{\mathrm{st}})^2}{LC}} \tag{3.19}$$

According to the above theoretical analysis, the parameters for the ac-side controller, i.e., k_p and k_i, can be obtained from

$$\begin{cases} \left|G_{\mathrm{qZSI}}(\omega_r)\right| = 1 \\ \angle G_{\mathrm{qZSI}}(\omega_r) = \theta_{\mathrm{PM}} \end{cases} \tag{3.20}$$

where θ_{PM} is the phase margin considering the effect of G_r.

To verify the above analysis and design, simulations in MATLAB/SimPowerSystems and experimental tests are implemented on a three-phase qZSI. The system parameters of the three-phase qZSI for the simulations and experimental tests are listed in Table 3.1. The simulations provided all cases that can lead to an unstable system, i.e., input condition and load current variations, as shown in Fig. 3.8. As mentioned previously, the peak dc-link

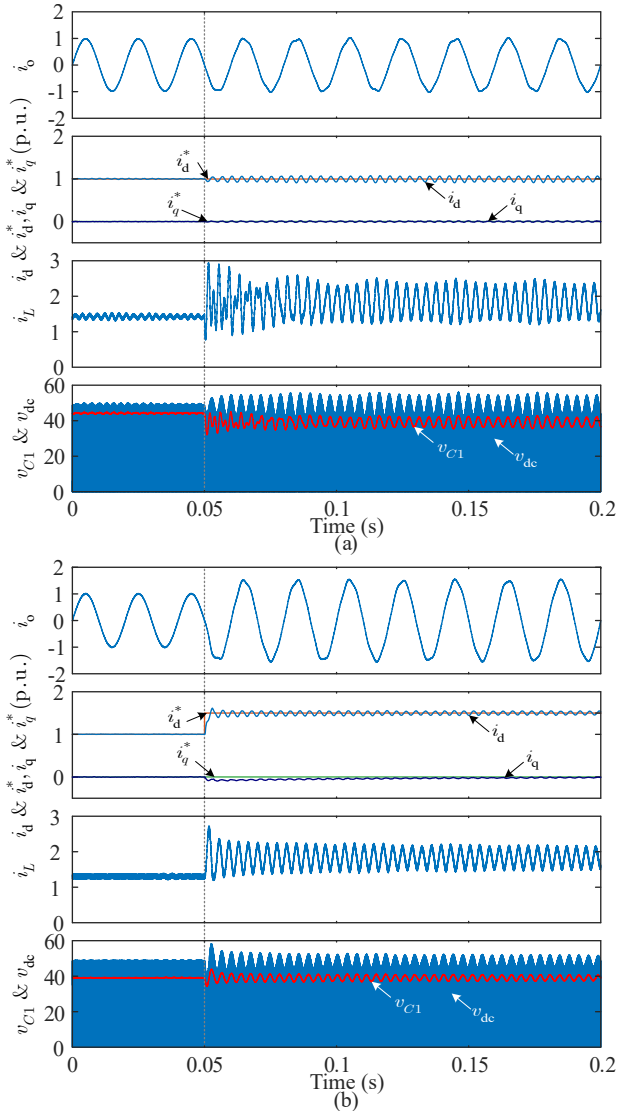

Fig. 3.8: Simulation results of the output current i_o, the current on dq-axis, the inductor current i_L, capacitor voltage v_{C1} and dc-link voltage v_{dc} of the qZSI when (a) input condition step changes and (b) load reference step changes.

voltage will remain constant by changing v_{in} and d_{sh} simultaneously. Then, the experimental results of the qZSI system under stable and unstable conditions are provided with the corresponding control parameters.

As observed in Fig. 3.8(a), when the input voltage step changes from 40 V to 30 V and the ST duty ratio step changes from 0.1 to 0.2 at 0.05 s, oscillations

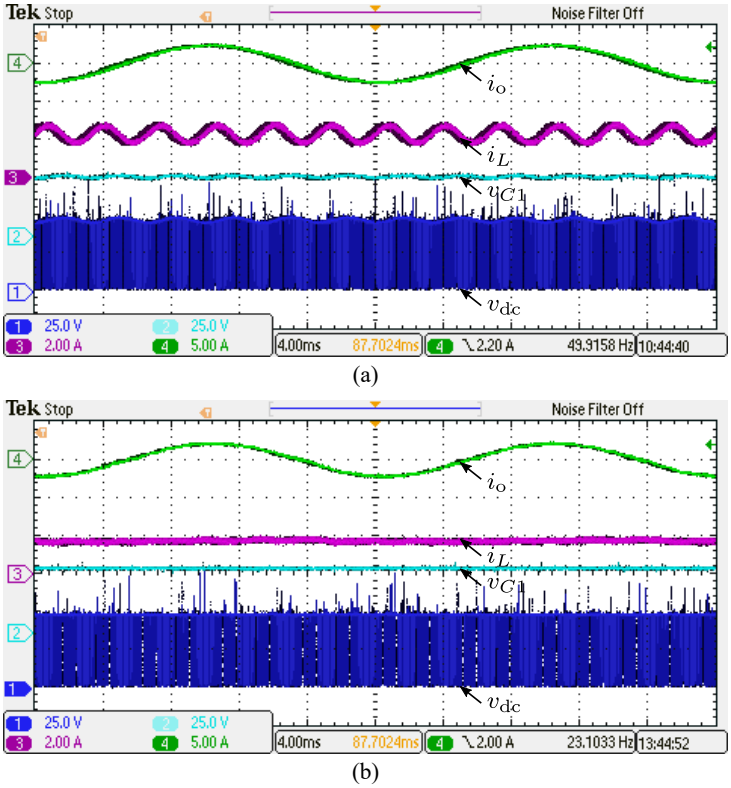

Fig. 3.9: Experimental results of the load current i_o [5 A/div], inductor current i_L [2 A/div], capacitor voltage v_{C1} [25 V/div] and dc-link voltage v_{dc} [25 V/div] when the qZSI is (a) unstable and (b) stable.

then occur in i_d, i_L, v_{C1} and v_{dc}. With an open-loop qZSN, the peak dc-link voltage is constant as 50 V, as seen in Fig. 3.8(a). The controller parameters are 0.4 and 20 for k_p and k_i, respectively in this case. When d_{sh} increases, the phase margin of G_{qZSI} is not enough to make the system stable. Referring to Fig. 3.8, and (3.19) in terms of oscillation frequency, the theoretical oscillation frequency is 284.7 Hz, and the oscillation frequency in the simulation result is 278 Hz, which agrees with the calculated analysis. As shown in Fig. 3.8(b), the input voltage is 40 V and the ST duty ratio is 0.1, which maintains the output of the qZSN. When the load current reference step change from 1 p.u. to 1.5 p.u at 0.05 s, oscillations then occur in i_d, i_L, v_{C1} and v_{dc}, as shown in Fig. 3.8(b). The oscillation frequency is not affected by the load current step change, which will only trigger the oscillations by reducing the phase margin of the qZSI system.

Furthermore, experimental results of the three-phase qZSI under unstable and stable conditions with identical system parameters in Table 3.1 were

performed. The input voltage v_{in} is 30 V, and the ST duty ratio d_{sh} is 0.2, which makes the peak dc-link voltage equal to 50 V, as shown in Fig. 3.9. When the control parameters k_p and k_i are 0.4 and 20, respectively, the qZSI system is unstable, as shown in Fig. 3.9(a). Oscillations appear in i_L, v_{C1} and v_{dc} with an oscillation frequency of 268 Hz, as observed in Fig. 3.9(a). The control parameters are designed for the VSI are not appropriate for the qZSI when the ST duty ratio increases. When taking G_{r} into design consideration, the control parameters k_p and k_i will be updated to 0.08 and 3, respectively. Then, the experimental results of the qZSI system with the modified control parameters are shown in Fig. 3.9(b). By fully considering the effect of the qZSN on the system dynamics, the qZSI system turns stable, as illustrated in Fig. 3.9(b). When designing the control system, the worst case should always be met first to ensure the qZSI system stable under all conditions.

3.5 Summary

In this chapter, the interactive modeling of the qZSI system considering the system stability has been investigated. The interactive models of the qZSI system are obtained. With the derived interactive models, the effect of the qZSN, i.e., G_{r}, on the stability issue is explored. To enhance the system stability under different operational conditions, e.g., input conditions and load variations, the control parameters for the ac-side controller should be well designed considering the effect of the qZSN. Simulations and experimental results that were implemented on a three-phase qZSI system have verified the analysis in this chapter.

Part III

Advanced Modulation and Control for the QZSI

There are three chapters in this part, i.e., ***Chapter 4****. Inductor Current Ripple Reduction with Modified SVM Strategies,* ***Chapter 5****. Common-Mode Voltage Mitigation for PV Applications, and* ***Chapter 6****. Control of the QZSN-based NPC Converter.*

4 Inductor Current Ripple Reduction through Modulation

This chapter will first investigate the inductor current ripples of the qZSI system when the conventional ZSVM6 strategy is used. The instantaneous inductor current ripples and the maximum inductor current ripple under different operational conditions will be derived with the conventional ZSVM6 strategy, which implements six identical ST intervals. According to the current ripple features, two modified ZSVM6 strategies are then developed to reduce the inductor current ripple for the three-phase two-level qZSI system.

4.1 Introduction

As shown in Fig. 2.1, the qZSN introduces two additional inductors, which will increase the volume and cost of the entire system. To decrease the size of the inductors in the qZSN, various methods have been proposed in the literature. For example, increasing the switching frequency or adopting a coupled inductor can reduce the inductor current ripple to some extent, but the system performance is also affected, e.g., more switching losses. The design of coupled inductors is not an easy job either. Alternatively, pulse

width modulation (PWM) techniques can be modified to reduce the inductor current ripple, which further results in smaller inductors.

There is only one ST interval in a switching cycle of the SPWM methods [8, 15], which makes the inductor current ripples large. By inserting x identical intervals in a switching cycle, the SVM strategies, e.g, ZSVMx ($x = 2, 4, 6$), can increase the equivalent operational frequency to reduce the inductor current ripples [60]. The comparison of the SVM strategies with identical ST intervals was presented in [61, 62]. However, the inductor current ripple can be further optimized with unequal ST intervals. In [63], the dwell time of the larger active vector is divided to reduce the maximum discharging current ripple, while the large charging current ripple remains. In [64] and [65], a small inductor ripple can be achieved by making the average discharging current equal to the average inductor current. By maintaining the charging ripple and discharging ripple identical in a sequence, the maximum inductor current ripple can be reduced in [66], which introduces additional computational burdens. However, no conclusion has been drawn for how to reduce the inductor current ripple under different operational conditions.

Thus, the ZSVM6 strategies will be explored in this chapter for inductor current ripple reduction under different operational conditions. Based on the feature of the instantaneous current ripples, ripple boundary can then be defined to reduce the overall ripple current. To verify the analysis and confirms the effectiveness of the proposed SVM strategies in terms of ripple current reduction, experimental tests have also been performed on a three-phase two-level qZSI in this chapter.

4.2 Inductor Current Ripple Analysis

The inductor current during the ST and non-ST states can be described as

$$\frac{di_L(t)}{dt} = \begin{cases} k_1 = V_{C1}/L & \text{ST} \\ k_2 = -(V_{C1} - V_{\text{in}})/L & \text{non-ST} \end{cases} \tag{4.1}$$

in which k_1, k_2 are the inductor charging and discharging coefficients, i_L, V_{in} and V_{C1} have been defined in Chapter 2.

As seen in Fig. 4.1, there are eight conventional space vectors (i.e., $\boldsymbol{V}_0$-$\boldsymbol{V}_7$) and an additional ST vector (i.e., $\boldsymbol{V}_{\text{st}}$), which divide the vector space into six sectors denoted by I, II, ..., VI [15]. The dwell time T_1, T_2, T_0 and T_{sh} of the SVM strategy for the qZSI in Sector I are derived as

$$\begin{cases} T_1 = mT_s \sin(\pi/3 - \theta) = d_1 T_s \\ T_2 = mT_s \sin\theta = d_2 T_s \\ T_0 - T_{\text{st}} = T_s - T_1 - T_2 - T_{\text{st}} = d_0 T_s \\ T_{\text{sh}} = d_{\text{sh}} T_s \end{cases} \tag{4.2}$$

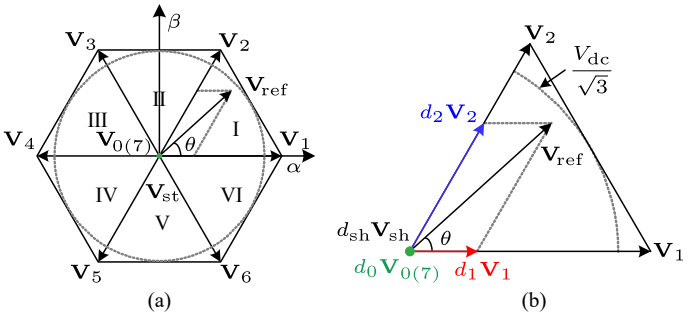

Fig. 4.1: Diagrams of (a) the vector space for the qZSI system with an output reference vector $\boldsymbol{V}_{\text{ref}}$ and (b) the switching vectors with corresponding dwelling duty ratio in Sector I.

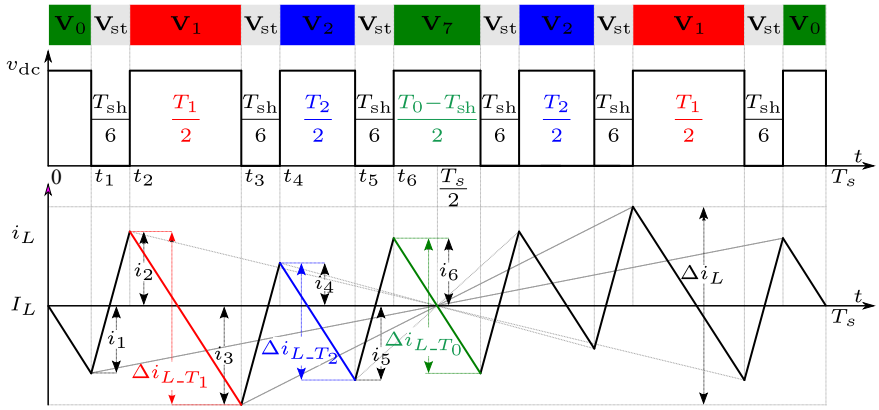

Fig. 4.2: Instantaneous ripple currents in a switching cycle with six identical ST intervals for the qZSI system.

where T_s is the switching period, T_1 and T_2 are the dwell time of $\boldsymbol{V}_1$ and $\boldsymbol{V}_2$, T_0 is the dwell time of $\boldsymbol{V}_{0(7)}$, T_{sh} is the dwell time of $\boldsymbol{V}_{\text{st}}$, θ is the output angle of $\boldsymbol{V}_{\text{ref}}$, and m is the modulation index. Then, the corresponding duty ratios of T_1, T_2, T_0, T_{sh} are denoted as d_1, d_2, d_0 and d_{sh}, which will be used to divide the operational region of the qZSI system.

As shown in Fig. 4.1(b), $\mathbf{V}_{\text{ref}}$ can then be synthesized with $\boldsymbol{V}_1$, $\boldsymbol{V}_2$, $\boldsymbol{V}_{0(7)}$ and $\boldsymbol{V}_{\text{sh}}$ as

$$\boldsymbol{V}_{\text{ref}} = d_1\boldsymbol{V}_1 + d_2\boldsymbol{V}_2 + d_0\boldsymbol{V}_{0(7)} + d_{\text{st}}\boldsymbol{V}_{\text{st}} \tag{4.3}$$

As presented in Fig. 4.2, the inductor discharging current ripples (denoted by $\Delta i_{L\_T_1}$, $\Delta i_{L\_T_2}$, and $\Delta i_{L\_T_0}$) and charging current ripples (denoted by $\Delta i_{L\_T_{\text{sh}}}$) with six identical ST intervals can be correlated by

$$\Delta i_{L\_T_{\text{sh}}} : \Delta i_{L\_T_1} : \Delta i_{L\_T_2} : \Delta i_{L\_T_0} = k_1\frac{T_{\text{sh}}}{6} : k_2\frac{T_1}{2} : k_2\frac{T_2}{2} : k_2\frac{T_0 - T_{\text{sh}}}{2} \tag{4.4}$$

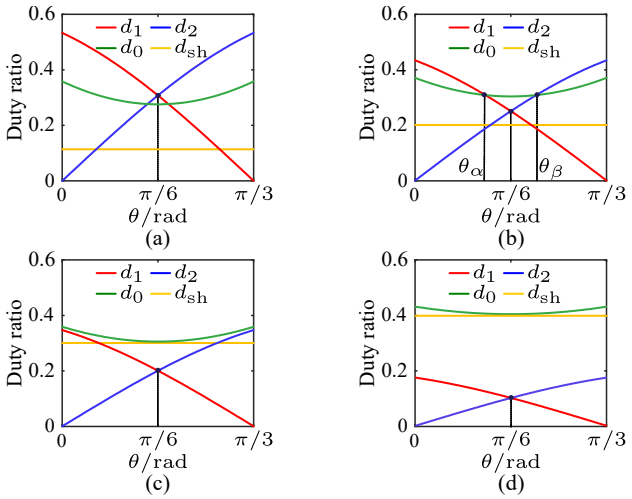

Fig. 4.3: Duty ratios d_1, d_2, d_0 and d_{sh} with the conventional ZSVM6 strategy in Sector I: (a) case 1 when max(d_1, d_2) is larger than d_0, (b) case 2 when max(d_1, d_2) is partially smaller than d_0, (c) case 3a when max(d_1, d_2) is smaller than d_0, and (d) case 3b when max(d_1, d_2) is much smaller than d_0.

The inductor current i_L is symmetric to the steady-state inductor current I_L. Accordingly, the instantaneous inductor current ripples i_x ($x = 1, 2, ..., 6$) when using the conventional ZSVM6 strategy in respect to steady-state inductor current I_L can be obtained as

$$\begin{cases} i_1 = i_6 = 3k\,|1 - d_{sh} - m\cos(\theta - \pi/6)| \\ i_2 = i_5 = k\,|1 - d_{sh} - 3m\cos(\theta - \pi/6)| \\ i_3 = k\left|1 - d_{sh} - 3\sqrt{3}m\sin(\theta - \pi/6)\right| \\ i_4 = k\left|1 - d_{sh} + 3\sqrt{3}m\sin(\theta - \pi/6)\right| \end{cases} \tag{4.5}$$

with k being defined as

$$k = \frac{V_{in} d_{sh} T_s}{12(1 - 2d_{sh})L} \tag{4.6}$$

As shown in Fig. 4.2, the maximum inductor current ripple Δi_L within a switching cycle is then expressed as

$$\Delta i_L = 2\max(i_1, i_2, i_3, i_4, i_5, i_6) \tag{4.7}$$

which is related to m, d_{sh} and the output angle θ of $\boldsymbol{V}_{ref}$.

Then, the operational region is divided into three cases to explore the effect of the operational conditions on the instantaneous ripples, as shown in Fig. 4.3. The maximum inductor instantaneous current ripple i_{Lmax} under

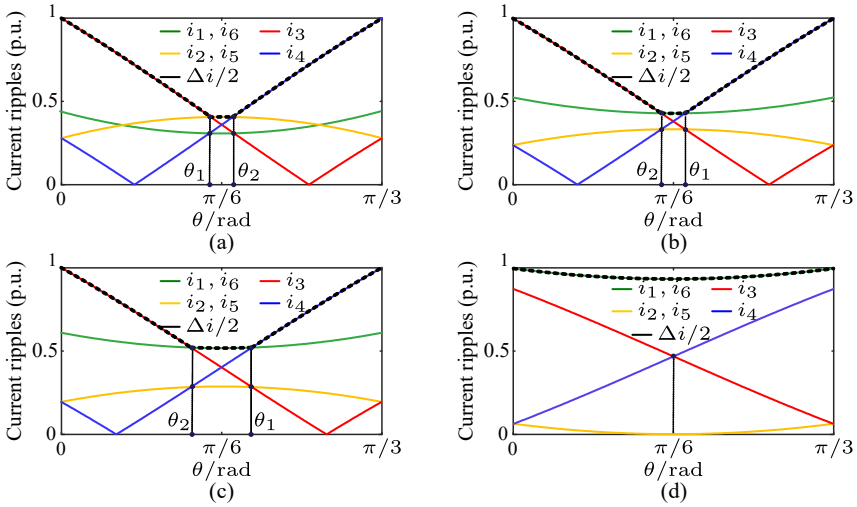

Fig. 4.4: Instantaneous inductor current ripples with the conventional ZSVM6 strategy, where $\boldsymbol{V}_{\text{ref}}$ is in Sector I: (a) case 1 when $\max(d_1, d_2)$ is larger than d_0, (b) case 2 when $\max(d_1, d_2)$ is partially smaller than d_0, (c) case 3a when $\max(d_1, d_2)$ is smaller than d_0, and (d) case 3b when $\max(d_1, d_2)$ is much smaller than d_0.

those cases are shown in Fig. 4.4(d). The maximum current ripple $\Delta i_{L\max}$ can then be expressed as

$$\Delta i_{L\,\max} = \begin{cases} 3\sqrt{3}mk + 2k(1 - d_{\text{sh}}), & \text{Case 1, 2, or 3a} \\ 6k(1 - d_{\text{sh}} - \dfrac{\sqrt{3}}{2}m), & \text{Case 3b} \end{cases} \tag{4.8}$$

The ST intervals within the ZSVM6 strategy will not affect the inductor discharging time in a switching cycle. The inductor discharging time is equal to the non-ST time, making the inductor discharging current ripples predictive [67]. Furthermore, six different ST intervals can be used to reduce the current ripple [68]. Considering the central axis-symmetric feature, only three different ST intervals need to be calculated in a switching cycle. The original six sectors are then divided into twelve zones, i.e., zones A and B, and then, the sum of the corresponding ST time intervals is

$$T_{a\text{X}} + T_{b\text{X}} + T_{c\text{X}} = \frac{T_{\text{sh}}}{2} \tag{4.9}$$

where $T_{a\text{X}}$, $T_{b\text{X}}$ and $T_{c\text{X}}$ are the unequal intervals with $\text{X} = \{\text{A}, \text{B}\}$, respectively. Meanwhile, the corresponding discharging current ripple can be expressed as

$$\Delta i_{L\_T_{a\text{X}}} : \Delta i_{L\_T_{b\text{X}}} : \Delta i_{L\_T_{c\text{X}}} = T_{a\text{X}} : T_{\text{bX}} : T_{\text{cX}} \tag{4.10}$$

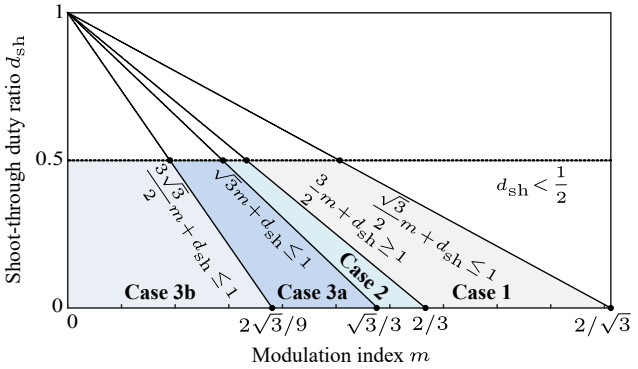

Fig. 4.5: Case classification considering the modulation index m and ST ratio $d_{\rm sh}$ in the operational region, where $d_{\rm sh} < \frac{1}{2}$.

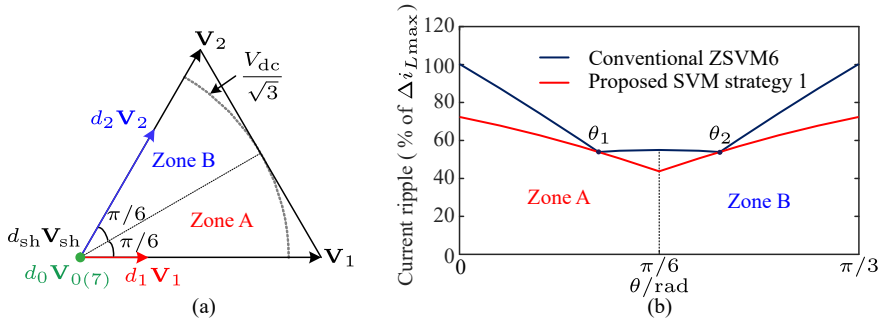

Fig. 4.6: Illustration of the ripple current reduction method by controlling the discharging current ripple for the qZSI: (a) operation rules of the proposed SVM strategy with the divided zones in Sector I, and (b) inductor current ripples with six identical ST intervals and the proposed unequal-ST ZSVM6 strategy in Sector I.

in which $\Delta i_{L\_T_{a\rm X}}$, $\Delta i_{L\_T_{\rm bX}}$, and $\Delta i_{L\_T_{\rm cX}}$ are the corresponding inductor charging current ripples. The proposed ripple reduction strategies can then be achieved flexibly, as detailed in the following section.

4.3 Ripple Current Reduction Strategies

4.3.1 Discharging Current Ripple Control

In operational conditions with high dc-link utilization like that in Case 1, the minimum ripple current within a switching cycle can be simplified as

$$\Delta i_{L\_\rm min} = \max(\Delta i_{L\_T_1}, \Delta i_{L\_T_2}) \tag{4.11}$$

According to $\Delta i_{L\_\rm min}$ in a switching cycle, the original operational zone in Sector I can be further divided into two zones, i.e., A and B, as seen in Fig. 4.6.

When $0 \leq \theta \leq \pi/6$, $\boldsymbol{V}_{\text{ref}}$ is in zone A with $T_1 \geq T_2$, which results in $\Delta i_{L\_T_1} \geq \Delta i_{L\_T_2}$ with $\Delta i_{L\_\min}$ equal to $\Delta i_{L\_T_1}$. By restricting all the instantaneous inductor current ripples within $\Delta i_{L\_T_1}$, the maximum ripple current can then be effectively limited. The instantaneous inductor current ripples $i_{x\text{A}}\,(x = 1, 2, ..., 6)$ in zone A are shown in Fig. 4.7(a). Meanwhile, x_{A} is introduced to indicate the moving distance of the mid-point of $\Delta i_{L\_T_2}$ to I_L. Hence, a coefficient k_{A} is used to describe x_{A} as

$$x_{\text{A}} = k_{\text{A}}\left(\frac{\Delta i_{L\_T_1}}{2} - \frac{\Delta i_{L\_T_2}}{2}\right) \tag{4.12}$$

where $0 \leq k_{\text{A}} \leq 1$. When $k_{\text{A}} = 1$, $\Delta i_{L\_T_2}$ reaches the boundary created by $\Delta i_{L\_T_1}$. When $k_{\text{A}} = 0$, the mid-point of $\Delta i_{L\_T_2}$ is the same as the average of the inductor current I_L. The three ST intervals $T_{a\text{A}}$, $T_{b\text{A}}$ and $T_{c\text{A}}$ can be obtained as

$$\begin{cases} T_{a\text{A}} = \dfrac{T_{st}}{4(T_s - T_{st})}(T_0 + T_1 - T_{st}) \\ T_{b\text{A}} = \dfrac{T_{st}}{4(T_s - T_{st})}[(1 - k_{\text{A}})T_1 + (1 + k_{\text{A}})T_2] \\ T_{c\text{A}} = \dfrac{T_{st}}{4(T_s - T_{st})}[T_0 + k_{\text{A}}T_1 + (1 - k_{\text{A}})T_2 - T_{st}] \end{cases} \tag{4.13}$$

Subsequently, the instantaneous inductor charging current ripples $i_{x\text{A}}$ in a switching cycle can be expressed as

$$\begin{cases} i_{1\text{A}} = i_{6\text{A}} = 3k\,|1 - d_{\text{sh}} - m\cos(\theta - \pi/6)| \\ i_{2\text{A}} = i_{3\text{A}} = 3km\sin(\pi/3 - \theta) \\ i_{4\text{A}} = 3km\,|(1 + k_{\text{A}})\sin\theta - k_{\text{A}}\sin(\pi/3 - \theta)| \\ i_{5\text{A}} = 3km\,|(1 - k_{\text{A}})\sin\theta + k_{\text{A}}\sin(\pi/3 - \theta)| \end{cases} \tag{4.14}$$

When $\pi/6 \leq \theta \leq \pi/3$, $\boldsymbol{V}_{\text{ref}}$ is in zone B with $T_1 < T_2$, making $\Delta i_{L\_T_1} < \Delta i_{L\_T_2}$ with $\Delta i_{L\_\min}$ equal to $\Delta i_{L\_T_2}$. $\Delta i_{L\_T_2}$ creates a ripple boundary to limit all the instantaneous inductor ripple currents, which reduces the maximum instantaneous ripple current. The instantaneous inductor current ripples $i_{x\text{B}}\,(x = 1, 2, ..., 6)$ in zone B are illustrated in Fig. 4.7(b). Then, x_{B} describes the moving track of the mid-point of $\Delta i_{L\_T_1}$. Meanwhile, a coefficient k_{B} can be used to describe x_{B} as

$$x_{\text{B}} = k_{\text{B}}\left(\frac{\Delta i_{L\_T_2}}{2} - \frac{\Delta i_{L\_T_1}}{2}\right) \tag{4.15}$$

where $0 \leq k_{\text{B}} \leq 1$. When $k_{\text{B}} = 1$, $i_{2\text{B}} = i_{4\text{B}} = i_{5\text{B}}$. Then, $\Delta i_{L\_T_1}$ reaches the ripple boundary that is defined by $\Delta i_{L\_T_2}$. When $k_{\text{B}} = 0$, $i_{2\text{B}} = i_{3\text{B}}$. The mid-point of $\Delta i_{L\_T_1}$ will be on the axis that represents the average current I_L.

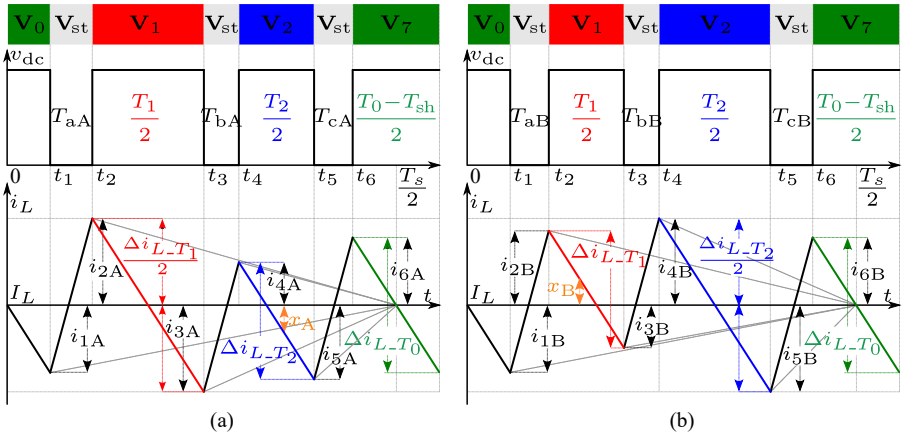

Fig. 4.7: Inductor current ripples with the modified SVM strategy (controlling the discharging current ripple) in one switching cycle: (a) when $T_1 \geq T_2$ and (b) when $T_1 < T_2$.

In a similar way as that in zone A, $T_{a\mathrm{B}}$, $T_{b\mathrm{B}}$ and $T_{c\mathrm{B}}$ can be expressed as

$$\begin{cases} T_{a\mathrm{B}} = \dfrac{T_{st}}{4(T_s - T_{st})}[T_0 + (1-k_{\mathrm{B}})T_1 + k_{\mathrm{B}}T_2 - T_{st}] \\ T_{b\mathrm{B}} = \dfrac{T_{st}}{4(T_s - T_{st})}[(1+k_{\mathrm{B}})T_1 + (1-k_{\mathrm{B}})T_2] \\ T_{c\mathrm{B}} = \dfrac{T_{st}}{4(T_s - T_{st})}(T_0 + T_2 - T_{st}) \end{cases} \tag{4.16}$$

Then, the instantaneous inductor charging current ripples $i_{x\mathrm{B}}$ within one switching cycle can be given as

$$\begin{cases} i_{1\mathrm{B}} = i_{6\mathrm{B}} = 3k\,|1 - d_{\mathrm{sh}} - m\cos(\theta - \pi/6)| \\ i_{2\mathrm{B}} = 3km\,|(1-k_{\mathrm{B}})\sin(\pi/3 - \theta) + k_{\mathrm{B}}\sin\theta| \\ i_{3\mathrm{B}} = 3km\,|(1+k_{\mathrm{B}})\sin(\pi/3 - \theta) - k_{\mathrm{B}}\sin\theta| \\ i_{4\mathrm{B}} = i_{5\mathrm{B}} = 3km\sin\theta \end{cases} \tag{4.17}$$

The maximum inductor ripple current appears with $\theta = 0$ in zone A or $\theta = \pi/3$ in zone B, which is then obtained as

$$\Delta i_{L\mathrm{max\_new}} = 3\sqrt{3}km \leq \Delta i_{L\mathrm{max}} \tag{4.18}$$

The ripple comparison of the conventional ZSVM6 and the improved ZSVM6 strategies in Sector I is presented in Fig. 4.6(b). As shown in Fig. 4.6(b), the maximum current ripples with the discharging current ripple control strategy are much smaller than those with six identical ST intervals, which can also be verified in the other sectors of the vector space, as shown in Fig. 4.1.

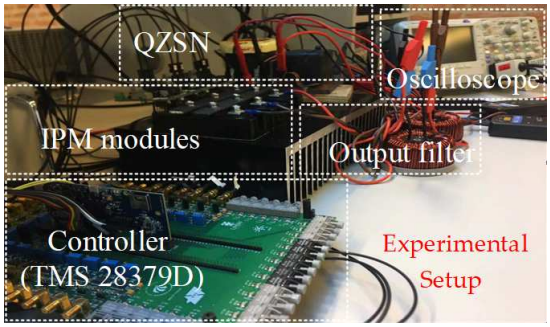

Fig. 4.8: Experimental setup of the three-phase qZSI system for ripple reduction verification.

Table 4.1: System Parameters of the qZSI for Verifying the Ripple Reduction Strategies.

Parameter	Value
Input voltage V_{in}	75 V
Inductors in the qZSI L_1, L_2	700 uH
Capacitors in the qZSI C_1, C_2	200 uF
Output filter L_f	1.8 mH
Load resistor R_{o}	10 Ω
Switching frequency f_s	10 kHz
Modulation index m	0.75
Shoot-through duty ratio d_{sh}	0.2

Accordingly, the inductor ripple current reduction ratio γ can then be obtained as

$$\gamma = 1 - \frac{\Delta i_{L\text{max\_new}}}{\Delta i_{L\text{max}}} = \frac{2(1-d_{\text{sh}})}{3\sqrt{3}m + 2(1-d_{\text{sh}})} \tag{4.19}$$

where γ can be affected by m and d_{sh}. Furthermore, γ can be used to further assess the performance of the ripple current reduction methods.

To verify the proposed SVM strategy, experimental tests are then performed to compare with the ZSVM6 strategy with six identical ST intervals. The experimental results of the qZSI system with six identical ST intervals in the conventional ZSVM6 strategy and updated ST intervals in the proposed SVM strategy are shown in Fig. 4.8. The system parameters of the qZSI are listed in Table 4.1. As shown in Fig. 4.9(a), the average inductor current I_L is 6.21 A with large instantaneous inductor current ripples in both zones A

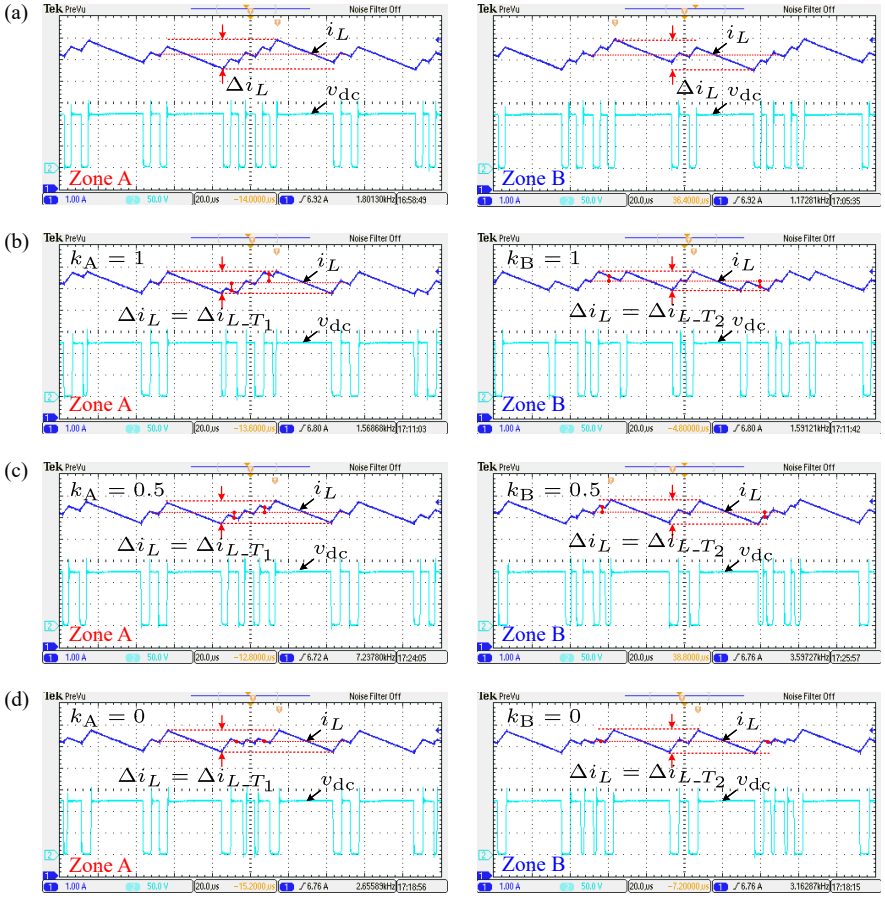

Fig. 4.9: Experimental results of the qZSI system with (a) six identical ST intervals and the updated six ST intervals when (b) $k_A = k_B = 1$, (c) $k_A = k_B = 0.5$, and (d) $k_A = k_B = 0$: inductor current i_L [1 A/div] and dc-link voltage v_{DC} [50 V/div] in a switching cycle.

and B with identical ST intervals, in which Δi_L is not optimized and related to the discharging current ripples. Moreover, as observed in Fig. 4.9(a), the instantaneous inductor current within a switching cycle is symmetric to I_L.

Three cases (i.e., $k_A = k_B = 1, 0.5, 0$) are performed to verify the proposed SVM strategy, and the corresponding experimental results are shown in Figs. 4.9(b)-(d). In those cases, the average inductor current I_L is the same as 6.21 A. Meanwhile, Δi_{Lmax} is decreased by 28.7% from 1.69 A to 1.21 A when compared with the ZSVM6 strategy strategy with six identical ST intervals. The ripple boundary in zone A will be $\Delta i_{L\_T_1}$, reducing the instantaneous current ripples. The mid-point of $\Delta i_{L\_T_1}$ is equal to I_L. With the defined k_A changing from 1 to 0, the mid-point of $\Delta i_{L\_T_2}$ moves to I_L.

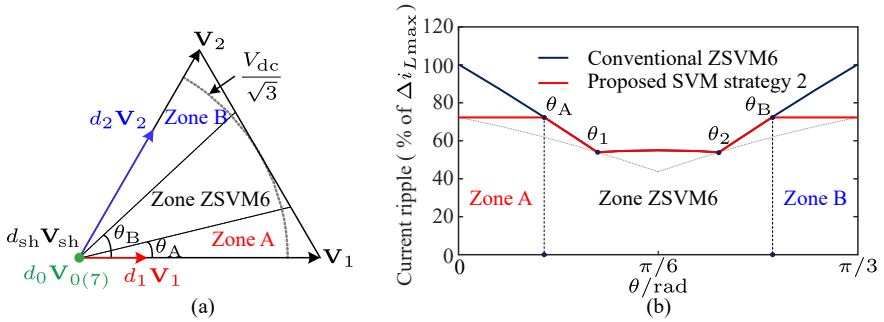

Fig. 4.10: Illustration of the ripple current reduction method by controlling the discharging current ripple for the qZSI: (a) vector space for the proposed SVM strategy with the divided zones in Sector I, and (b) inductor current ripples with six identical ST intervals and the updated six ST intervals in Sector I.

The ripple boundary in zone B will be the discharging current ripple $\Delta i_{L\_T_2}$, which is adopted for ripple reduction. The mid-point value of $\Delta i_{L\_T_2}$ also equal to I_L. When the improved SVM strategy is considered, Δi_L in a switching cycle becomes unrelated with the inductor charging current ripples, referring to (4.18). When the defined $k_{\rm B}$ varies from 1 to 0, $\Delta i_{L\_T_1}$ moves from the boundary created by $\Delta i_{L\_T_2}$ to I_L. As shown in Figs. 4.9(b)-(d), the inductor current remains symmetric to I_L in a switching cycle with the updated ST intervals in the modified SVM strategy. Furthermore, there is no necessary for $k_{\rm A}$ and $k_{\rm B}$ to be exactly the same in zones A and B when implementing the modified SVM strategy. Although the ST intervals are different when using the modified SVM strategy, the switch commutation number will remain the same as the case where six identical ST intervals are used, without introducing additional power losses. Overall, the given experimental tests have then verified the effectiveness of the modified SVM strategy for ripple reduction in the qZSI system by controlling the discharging current ripples.

4.3.2 Instantaneous Current Ripple Control

The inductor current ripple can also be reduced by only recalculating the ST intervals that are relevant to the instantaneous current ripple. With this, current ripples can also be effectively reduced, while achieving a lower computational burden. Referring to (4.8) and (4.18) for cases 1, 2 and 3a, the ripple bound varies from $3\sqrt{3}mk$ to $3\sqrt{3}mk + 2k(1 - d_{\rm sh})$ when m and $d_{\rm sh}$ meet

$$\sqrt{3}m + d_{\rm sh} \geq 1 \tag{4.20}$$

To obtain a higher reduction ratio, the ripple boundary is defined as $3\sqrt{3}mk$. The defined ripple boundary can have intersections with i_3 and i_4 (see Fig. 4.4), which divide the example Sector I into three zones, i.e., zones A, ZSVM6, and

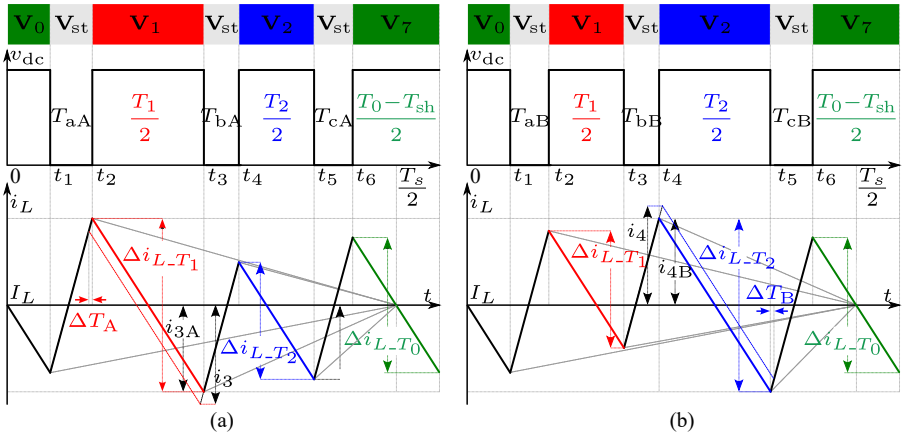

Fig. 4.11: Instantaneous inductor current ripples with the improved six ST intervals in a switching cycle: (a) when $T_1 > t_{\text{boundary}}$ and (b) when $T_2 > t_{\text{boundary}}$.

B, as illustrated in Fig. 4.10(a). The phases at the intersections of i_3, i_4 with the ripple boundary are denoted as θ_{A} and θ_{B}, as shown in Fig. 4.10(b). Then, the boundary interval for T_1 and T_2, which is used to detect the zones, is obtained as

$$t_{\text{boundry}} = \underbrace{mT_s \sin(\pi/3 - \theta_{\text{A}})}_{T_{1\_\text{boundry}}} = \underbrace{mT_s \sin(\theta_{\text{B}})}_{T_{2\_\text{boundry}}} \tag{4.21}$$

When $0 \le \theta \le \theta_{\text{A}}$, $\boldsymbol{V}_{\text{ref}}$ is in zone A with $T_1 \ge t_{\text{boundry}}$, which makes $i_3 \ge 3\sqrt{3}mk$. Thus, the ST time intervals ($T_{a\text{A}}$, $T_{b\text{A}}$) related to $\Delta i_{L\_T_1}$ should be recalculated, where $T_{a\text{A}}$, $T_{b\text{A}}$ and $T_{c\text{A}}$ can be obtained as

$$\begin{cases} T_{a\text{A}} = \dfrac{T_{st}}{6} + \dfrac{(12T_1 + 6T_0 - 2T_{st} - 4T_s - 3\sqrt{3}mT_s)T_{st}}{24(T_s - T_{st})} = \dfrac{T_{st}}{6} + \Delta T_{\text{A}} \\ T_{b\text{A}} = \dfrac{T_{st}}{6} - \dfrac{(12T_1 + 6T_0 - 2T_{st} - 4T_s - 3\sqrt{3}mT_s)T_{st}}{24(T_s - T_{st})} = \dfrac{T_{st}}{6} - \Delta T_{\text{A}} \\ T_{c\text{A}} = \dfrac{T_{st}}{6} \end{cases} \tag{4.22}$$

When $\theta_{\text{A}} < \theta < \theta_{\text{B}}$, $\boldsymbol{V}_{\text{ref}}$ will be in zone ZSVM6 with $\max(T_1, T_2)$ being smaller than t_{boundry}, making all the instantaneous ripples smaller than $3\sqrt{3}mk$. Then, six identical ST intervals can be used directly in this zone.

When $\theta_{\text{B}} \le \theta \le \pi/3$, $\boldsymbol{V}_{\text{ref}}$ is in zone B with $T_2 \ge t_{\text{boundry}}$. Only i_4 exceeds the defined boundary in zone B, leading to the recalculation of the ST intervals $T_{b\text{B}}$ and $T_{c\text{B}}$, as shown in Fig. 4.11(b), while $T_{a\text{B}}$ remains. Then, according

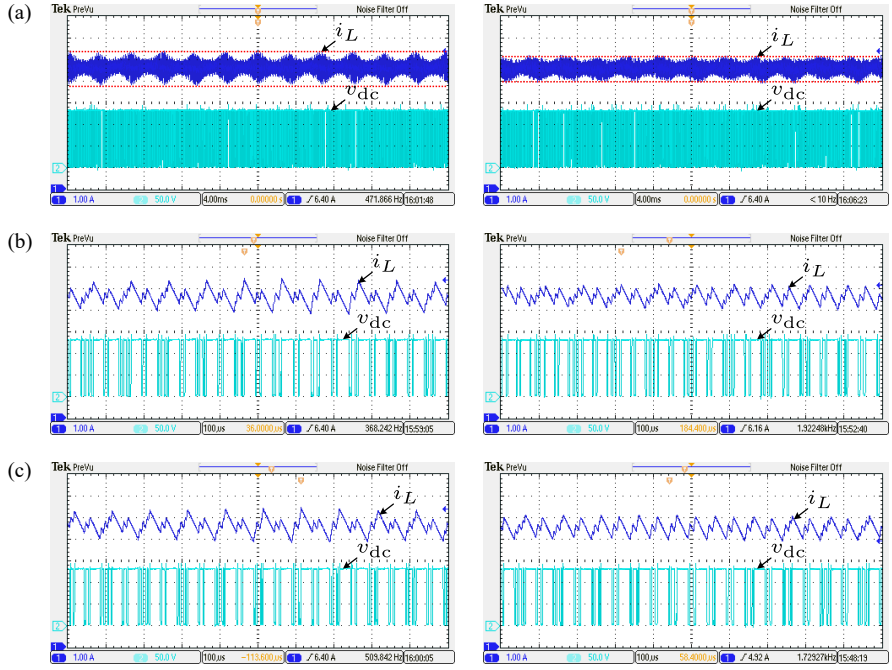

Fig. 4.12: Experimental results of the qZSI with six identical ST intervals and the modified six ST intervals in (a) one line cycle (b) zone A, and (c) zone B: inductor current i_L [1 A/div] and dc-link voltage v_{DC} [50 V/div].

to Fig. 4.11(b), $T_{a\mathrm{B}}$, $T_{b\mathrm{B}}$ and $T_{c\mathrm{B}}$ can be expressed as

$$\begin{cases} T_{a\mathrm{B}} = \dfrac{T_{st}}{6} \\ T_{b\mathrm{B}} = \dfrac{T_{st}}{6} - \dfrac{(12T_2 + 6T_0 - 2T_{st} - 4T_s - 3\sqrt{3}mT_s)T_{st}}{24(T_s - T_{st})} = \dfrac{T_{st}}{6} - \Delta T_{\mathrm{B}} \\ T_{c\mathrm{B}} = \dfrac{T_{st}}{6} + \dfrac{(12T_2 + 6T_0 - 2T_{st} - 4T_s - 3\sqrt{3}mT_s)T_{st}}{24(T_s - T_{st})} = \dfrac{T_{st}}{6} + \Delta T_{\mathrm{B}} \end{cases} \tag{4.23}$$

With the updated ST intervals in the three zones, the maximum instantaneous ripple will not be larger than $3\sqrt{3}mk$. Then, the maximum instantaneous ripple current with the proposed SVM strategy will be equal to $3\sqrt{3}mk$.

Notably, the reduction ratio of this method is the same as that in (4.19), which is also related to the ST duty ratio d_{sh} and modulation index m. Fig. 4.10(b) benchmarks the inductor current ripple of the proposed method with six identical ST intervals under the same operational conditions. Only the related ST intervals will be recalculated in the proposed strategy for ripple reduction, reducing the calculation burden and implementation complexity.

To verify the proposed strategy, experimental tests are provided in this section, as shown in Fig. 4.12. The input voltage v_{in} is 80 V, and the ST duty ratio is 0.2. As seen in Fig. 4.12, the average inductor current I_L is 5.52A in both ZSVM6 strategies. Comparing the experimental results in Fig. 4.12(a), the inductor current ripples with six identical ST intervals can be further optimized, while the proposed SVM strategy can reduce the maximum ripple by 32.1% from 1.53 A to 1.04 A. The instantaneous inductor current ripples in zone A with both strategies are shown in Fig. 4.12(b). The maximum inductor ripple current with the proposed SVM strategy is limited to the defined boundary in zone A, while the maximum ripple current with six identical ST intervals exceeds the predefined boundary. Similarly, the inductor current ripples in zone B with the proposed SVM strategy is within the defined boundary. With the proposed ZSVM6 strategy, the inductor charging current ripple Δi_L is not affected by the ST charging current ripples in a switching cycle. Moreover, the instantaneous inductor current remains symmetric to I_L in a switching cycle, as observed in Fig. 4.12. The instantaneous ripple currents with six identical ST intervals, exceeding the defined boundaries, are effectively reduced by the proposed strategy, as shown in Fig. 4.12. Referring to (4.8) and (4.18), the current ripple reduction ratio γ with the proposed strategy will be dependent on the ST duty ratio d_{sh} and modulation index m. Moreover, during the operation process, only the ST intervals that are related to the instantaneous inductor current exceeding the bounds will be recalculated, while the other ST intervals remain as $T_{\text{sh}}/6$. This guarantees that the operation of the qZSI is not affected. In all, the experimental results have validated the proposed method in terms of effective current ripple reduction while achieving a low computation burden.

4.4 Summary

In this chapter, the inductor current ripples of the qZSI system with six ST intervals have been explored. The instantaneous inductor current ripples with six identical ST intervals have been derived under all operational conditions. According to the obtained instantaneous inductor current ripples, two current ripple reduction strategies have been proposed, by controlling the discharging current ripple and directly limiting the instantaneous current ripple, respectively. Then, experimental tests were performed on a three-phase two-level qZSI system, which have validated the effectiveness of the proposed strategy strategies for ripple current reduction.

5 Common-Mode Voltage Mitigation for PV Applications

This chapter will address the CMV issue that due to the additional ST state for the three-phase two-level qZSI system. The CMV reduction strategies for the qZSI system will be explored in this chapter by making the full of the CMV reduction strategies for the conventional two-level VSI. Several conventional CMV reduction strategies will be exemplified and modified in this chapter to verify the effectiveness of the proposed strategy for the three-phase 2L qZSI-based system.

5.1 Introduction

Considering the feature of relatively small volume and easy installation, PV technology is particularly popular for renewable generation applications. Meanwhile, a power-electronic-based conversion system is essential for transferring solar energy to the grid. With the features, e.g., low-voltage and intermittent, the boosting capability should be included in the power-electronic-based conversion system for PV applications. To reduce the cost and volume of the transformer-based PV system, transformerless alternatives have been used widely nowadays. However, the leakage current will appear for the absence of galvanic isolation between the PV source and the grid, leading to electromagnetic interference and distorted currents [69–71]. Thus, the leakage current should be limited to a certain level [72].

For the transformerless PV system, common-mode voltage (CMV) can lead to large leakage currents [73, 74]. To reduce CMV and leakage currents, various methods have been proposed [75–77]. By using modulation technologies with appropriate switching patterns, the CMV of the PV system can be reduced, leading to smaller leakage currents [78–80]. Meanwhile, conventional control schemes can also be modified to alleviate the CMV [18, 81–85].

As an representative to the conventional two-stage structure, the qZSI can operate with a high boosting gain by using the extra ST state for PV applications, as shown in Fig. 5.1. With the ST state, the high-frequency components that exist in the CMV become larger in the qZSI system when compared with those in the two-stage structure [86]. The ST state makes the CMV reduction strategies for the VSI unavailable for the qZSI system for introducing an additional CMV value. A CMV comparison of the typical modulation strategies for the three-phase qZSI is presented in [87]. In [88], an improved PWM strategy is proposed by using only odd vectors and ST vector, leading to a relatively low dc-link utilization ratio. The higher dc-link utilization ratio can be obtained by adopting the similar method in three-phase four-leg qZSI to reduce the leakage currents, as presented in [89, 90].

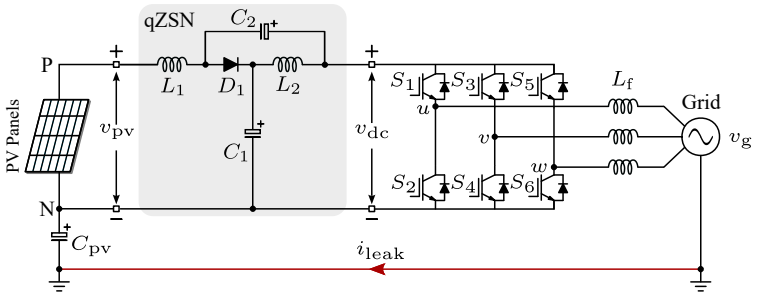

Fig. 5.1: A typical three-phase grid-tied qZSI system, in which the qZSN has two inductors L_1, L_2, two capacitors C_1, C_2, and a diode D_1, L_f is the grid-side filter, v_g is the grid voltage, C_{pv} is the capacitor between the negative terminal of the PV panels and the ground, and i_{leak} is the leakage current.

Table 5.1: Switching Vectors and Corresponding CMV Values in the qZSI.

Vectors	CMV Values
$\mathbf{V}_1$, $\mathbf{V}_3$, $\mathbf{V}_5$ (odd vectors)	$V_{dc}/3$
$\mathbf{V}_2$, $\mathbf{V}_4$, $\mathbf{V}_6$ (even vectors)	$2V_{dc}/3$
$\mathbf{V}_7$ (zero vector)	V_{dc}
$\mathbf{V}_0$ (zero vector)	0
$\mathbf{V}_{sh}$ (shoot-through vectors)	0

In [91], there is a diode connected to the negative side of the PV source to limit the leakage current during the ST state, leading to a discontinuous input current.

To make the most of the qZSI-based system, it is necessary to tackle the extra high-frequency issues in the CMV from the additional ST state. Thus, this chapter then introduces a CMV reduction method for the qZSI by splitting the input inductors of the qZSI to enable the conventional CMV reduction strategies, i.e., the strategies for the VSI-based system, and the effectiveness is validated by simulations and experimental tests.

5.2 CMV Analysis of the QZSI

CMV can be obtained as the average of the voltages through points u, v, w to the common reference N, as shown in Fig. 5.1. Then, the CMV for the qZSI can be obtained as [92]

$$v_{cmv} = \frac{v_{uN} + v_{vN} + v_{wN}}{3} \tag{5.1}$$

where v_{cmv} is the CMV under different switching vectors, and v_{uN}, v_{uN} and v_{uN} are the voltages through points u, v, w to the common reference N.

In addition to the commonly used switching states, i.e., six active vectors ($\mathbf{V}_1$, $\mathbf{V}_2$, $\mathbf{V}_3$, $\mathbf{V}_4$, $\mathbf{V}_5$, $\mathbf{V}_6$) and two zero vectors ($\mathbf{V}_0$, $\mathbf{V}_7$), the qZSI has an extra ST state ($\mathbf{V}_{\text{sh}}$). Accordingly, the switching states of the qZSI can be classified into five groups: odd vectors $\mathbf{V}_{odd}$ ($\mathbf{V}_1$, $\mathbf{V}_3$, $\mathbf{V}_5$), even vectors $\mathbf{V}_{even}$ ($\mathbf{V}_2$, $\mathbf{V}_4$, $\mathbf{V}_6$), zero vector $\mathbf{V}_7$, zero vector $\mathbf{V}_0$, and ST vector $\mathbf{V}_{\text{sh}}$. Table 5.1 summarizes the switching vectors and the relevant CMV, and with different switching patterns, the CMV shows different features.

With different switching patterns, the CMV varies periodically, making the CMV affected by the modulation strategies. However, the CMV of the qZSI system with additional ST states contains large high-frequency components. Moreover, the adoption of the ST state makes the typical CMV reduction strategies for the VSI unavailable for the qZSI system. To tackle this issue, a short review of the conventional CMV reduction strategies for the two-level VSI is discussed in the next section.

5.3 Conventional CMV Reduction Strategies

There are various CMV reduction strategies for the VSI, which can reduce the CMV by rearranging the switching sequence with chosen switching vectors, e.g, discontinuous pulse width modulation (DPWM) strategy, the active zero state pulse width modulation (AZSPWM) strategy, the near state pulse width modulation (NSPWM), and the remote state pulse width modulation (RSPWM) strategy, as shown in Fig. 5.2.

By using switching vectors partially, the CMV can be reduced when compared with strategies using all switching vectors. The space vectors, switching signals and the corresponding CMV of the typical CMV reduction strategies for the VSI in Sector I are presented in Fig. 5.2. As shown in Fig. 5.2(a), the CMV varies from $V_{\text{dc}}/3$ to V_{dc} when no zero vector $\mathbf{V}_0$ is used in the DPWM strategy. The complementary switching vectors, e.g., $\mathbf{V}_3$ and $\mathbf{V}_6$ in Sector I, are adopted to generate zero-state output in the AZSPWM strategy without using zero vectors $\mathbf{V}_0$ and $\mathbf{V}_7$, making the CMV limited between $V_{\text{dc}}/3$ and $2V_{\text{dc}}/3$, as seen in Fig. 5.2(b). If only the switching vectors with the same CMV value are used, e.g., all odd vectors with $V_{\text{dc}}/3$ or all even vectors with $2V_{\text{dc}}/3$, a constant CMV can be obtained with the RSPWM strategy, as observed in Fig. 5.2(c). In the NSPWM strategy, only three active switching vectors that are near to $\mathbf{V}_{\text{ref}}$ will be adopted to generate the output, limiting the CMV between $V_{\text{dc}}/3$ and $2V_{\text{dc}}/3$, as shown in Fig. 5.2(d). Generally, using more groups of switching vectors makes the dc-link utilization ratio higher.

However, the ST state introduces additional high-frequency components into the CMV of the qZSI system. The CMV reduction strategies for the VSI can not be utilized for the qZSI system directly. Thus, it is necessary to find

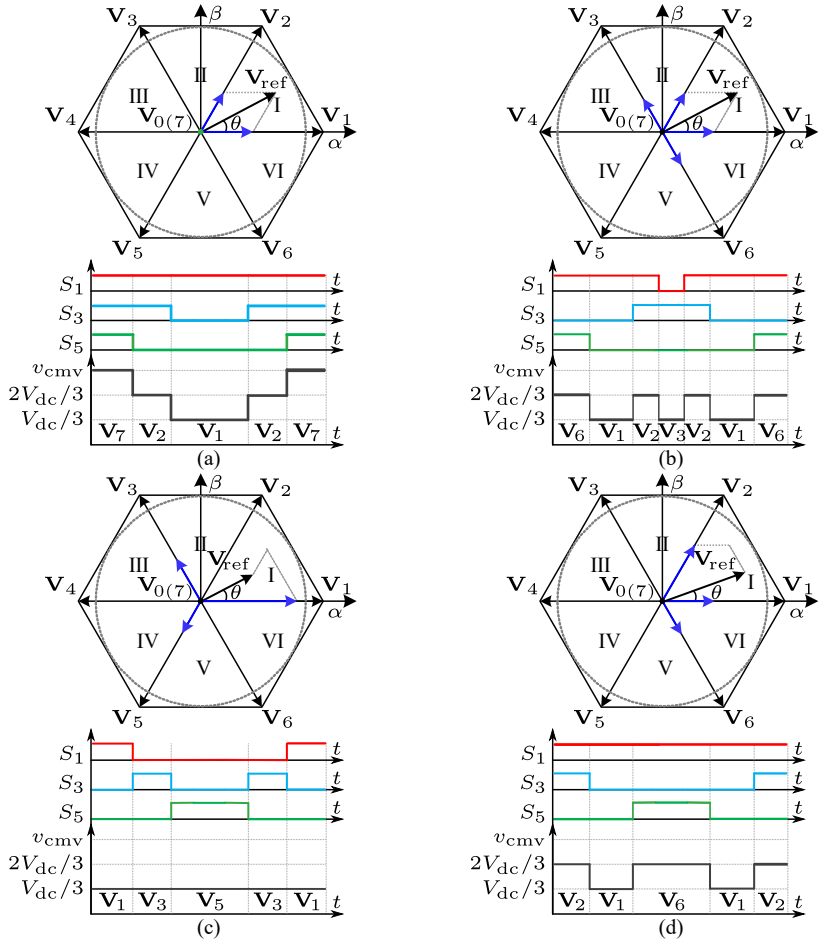

Fig. 5.2: CMV reduction strategies for the conventional two-level VSI with switching patterns and CMVs when adopting: (a) the DPWM strategy, (b) the AZPWM strategy, (c) the RSPWM strategy, and (d) the NSPWM strategy.

a solution to mitigation the effect of the ST state on the CMV, which enables the typical CMV reduction strategies for the qZSI system.

5.4 Modified QZSI for CMV Reduction

Although the ST state can be adopted in the qZSI to achieve boosting capability, the CMV characteristics are also affected. During the ST state, the CMV value is equal to zero, as presented in Table 5.1. Then, in this section, a split-input-inductor strategy is proposed to mitigate the effect of ST state on the CMV for the qZSI system, as shown in Fig. 5.3. With an inductor between

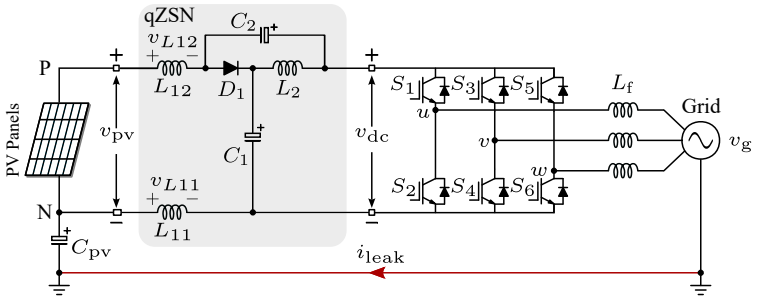

Fig. 5.3: Improved grid-connected qZSI system with a split input inductor.

the negative terminal N and the inverter, the CMV value during the ST state will not be zero. The split ratio of the input inductor can be derived by the relationship between the average CMV during the ST state and the CMV during the non-ST state [36], while the total input inductance will remain as L. Then, the proposed CMV reduction strategy for the qZSI by mitigating the effect of the ST state on the CMV can then be realized as follows.

The voltage through inductor L_1 during the non-ST and ST states can be expressed as

$$v_{L1} = \begin{cases} -D_{\text{sh}} V_{\text{dc}} & \text{non-ST state} \\ (1 - D_{\text{sh}}) V_{\text{dc}} & \text{ST state} \end{cases} \tag{5.2}$$

As shown in Fig. 5.4, the voltage through L_1 and the CMV with different CMV reduction strategies are presented. The voltage through L_1 is positive during the ST state and negative during the non-ST state. Meanwhile, the CMV is positive during the non-ST state and equal to zero during the ST state. The voltage through L_1 can be adopted to compensate the CMV by shifting the inductor voltage partially. To obtain the split ratio of the inductor, the average CMV during the non-ST state should be calculated, and which is obtained as

$$v_{\text{cmv\_avg}} = \frac{0 \cdot t_{zero\_0} + V_{\text{dc}}/3 \cdot t_{odd} + 2V_{\text{dc}}/3 \cdot t_{even} + V_{\text{dc}} \cdot t_{zero\_7}}{t_{zero} + t_{odd} + t_{even}} \tag{5.3}$$

with $v_{\text{cmv\_avg}}$ being the average CMV during the non-ST state, t_{odd}, t_{even}, t_{zero_0} and t_{zero_7} are the dwell time of all odd switching vectors, all even switching vectors, zero switching vector $\mathbf{V}_0$ and zero switching vector $\mathbf{V}_0$. The total dwell time of all zero switching vectors is denoted as t_{zero} ($t_{zero} = t_{zero\_0} + t_{zero\_7}$). $v_{\text{cmv\_avg}}$ is shown in Fig. 5.4 (in red).

To implement the proposed CMV reduction strategy, the inductor L_1 is split into two inductors, i.e., inductors L_{11} and L_{12}, as shown in Fig. 5.3. Ignoring the nonlinear features and the inner parasitic parameter in the inductors, the inductors L_1, L_{11}, L_{12}, and the voltage through them can be

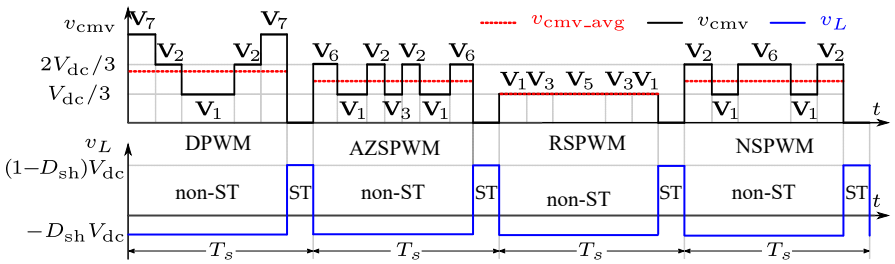

Fig. 5.4: Conventional CMV reduction strategies with ST state when using: (a) the DPWM strategy, (b) the AZPWM strategy, (c) the RSPWM strategy, and (d) the NSPWM strategy.

described as

$$\begin{cases} L_{11} = xL_1 \\ L_{12} = (1-x)L_1 \end{cases} \Rightarrow \begin{cases} v_{L_{11}} = xv_{L_1} \\ v_{L_{12}} = (1-x)v_{L_1} \end{cases} \tag{5.4}$$

in which x is the split ratio that describes the linear relationship among L_1, L_{11} and L_{12}, v_{L11} and v_{L12} are the voltages through L_{11} and L_{12}, and v_{L1} is the voltage through inductor L_1.

Then, the CMV in (5.1) can be updated when using a split input inductor, and which can be obtained as

$$v'_{\rm cmv} = v_{L11} + \frac{v_{uN'} + v_{vN'} + v_{wN'}}{3} \tag{5.5}$$

in which $v'_{\rm cmv}$ is the updated CMV with a split input inductor, $v_{uN'}$, $v_{vN'}$ and $v_{wN'}$ are the voltages through points u, v, w to the updated common reference N′.

Accordingly, the updated average CMV during the non-ST and the CMV during the ST states can then be obtained as

$$v'_{\rm cmv} = \begin{cases} v_{\rm cmv\_avg} - xD_{\rm sh}V_{\rm dc} & \text{non-ST state} \\ x(1-D_{\rm sh})V_{\rm dc} & \text{ST state} \end{cases} \tag{5.6}$$

To reduce the CMV difference between the non-ST and ST states, the relationship between the updated average CMV during the non-ST state and the CMV during the ST state should meet

$$v_{\rm cmv\_avg} - xD_{\rm sh}V_{\rm dc} = x(1-D_{\rm sh})V_{\rm dc} \tag{5.7}$$

Then, the split ratio x can be obtained as

$$x = \frac{0 \cdot t_{zero\_0} + 1 \cdot t_{odd} + 2 \cdot t_{even} + 3 \cdot t_{zero\_7}}{3 \cdot (t_{zero} + t_{odd} + t_{even})} \tag{5.8}$$

Table 5.2: Split Ratio with Different CMV Reduction Strategies.

CMV Reduction Strategies	Split Ratio x
DPWM Strategy	Inconstant
AZPWM Strategy	Constant as 1/2
RSPWM (odd)) Strategy	Constant as 1/3
RSPWM (even)) Strategy	Constant as 2/3
RSPWM (odd-even)) Strategy	Constant as 1/2
NSPWM Strategy	Constant as 1/2

Table 5.3: System Parameters of the QZSI System for CMV Reduction Strategies.

Parameters	Symbol	Values
Input voltage	V_{in}	160 V
qZSI inductors	L_1, L_2	700 uH
qZSI inductor resistance	R_{L1}	0.05 Ω
qZSI capacitors	C_1, C_2	200 uF
qZSI capacitor resistance	R_{C1}	0.05 Ω
Output filter	L_f	1.8 mH
Switching frequency	f_s	10 kHz
Shoot-through duty ratio	D_{sh}	0.1

Moreover, the average updated CMV $\bar{v}_{CM}$ can then be described as

$$\bar{v}_{\text{cmv}} = \frac{(1 - D_{\text{sh}})(t_{odd} + 2t_{even} + 3t_{zero\_7})V_{\text{dc}}}{3 \cdot (t_{zero} + t_{odd} + t_{even})} \tag{5.9}$$

in which all the variables have been defined previously.

The split ratio x with typical CMV reduction strategies are summarized in Table 5.2. Three kinds of RSPWM strategies are included, i.e., all odd switching vectors, all even switching vectors, and odd-even switching patterns which changes the group of corresponding switching vectors every $\pi/6$ in the vector space. As shown in Table 5.2, the split ratio x for the AZPWM, all RSPWM and NSPWM strategies are constant, while the split ratio of the DPWM strategy is inconstant which is affected by the operational conditions. Thus, when adopting this CMV strategy, the switching vectors need to be decided before design the qZSI system.

With the proposed strategy, the CMV value in the conventional qZSI system will be modified. The CMV value that is smaller than $\bar{v}_{\text{cmv}}$ will increase,

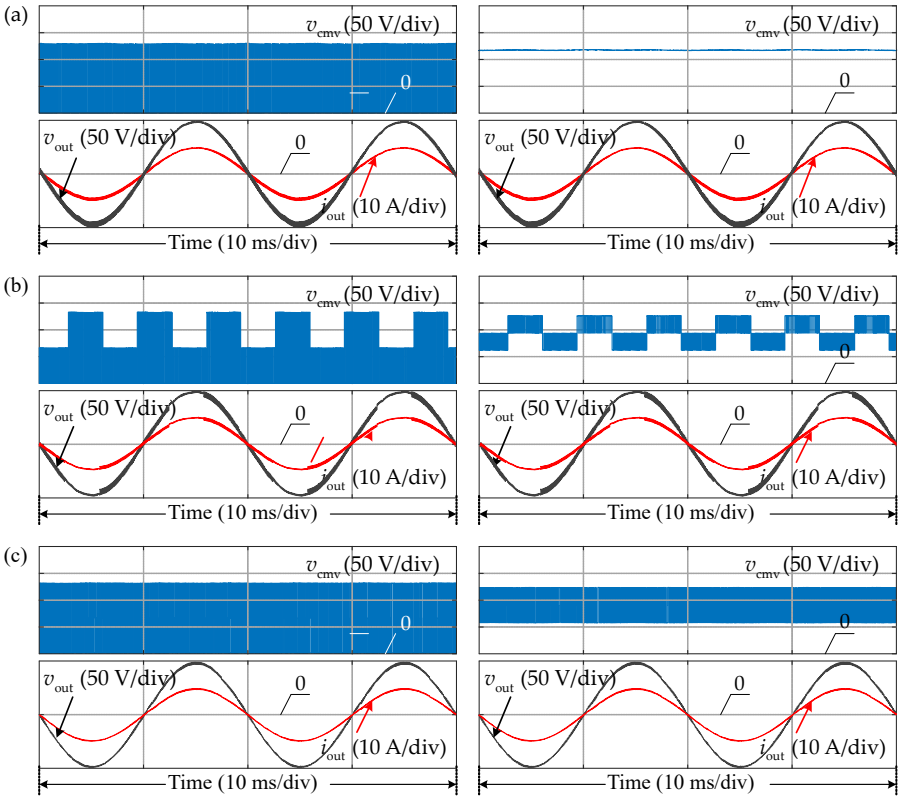

Fig. 5.5: Simulation results of the CMV v_{cmv}, output voltage v_{out} and output voltage i_{out} in the three-phase qZSI system without/with the split input inductor when (a) the RSPWM (even) strategy, (b) the RSPWM (odd-even) strategy, and (c) the NSPWM strategy are used: Time (10 ms/div).

while the CMV value that is larger than $\bar{v}_{cmv}$ will move towards $\bar{v}_{cmv}$, which can reduce the amplitude of the CMV for the updated qZSI system and further reduce the high-frequency components in the CMV. As for the variation of inductors L_{11} and L_{12}, the split ratio x will also be affected. However, the inductance variation ratio will reflect the CMV difference of the average CMV during the non-ST state and the CMV during the ST state, which shows a negligible effect on the CMV reduction if this variation is small.

To verify the effectiveness of the proposed CMV reduction strategy, simulations and experimental tests are performed on the three-phase qZS in this section. The system parameters for both simulations and experimental tests of the qZSI system are the same and listed in Table 5.3. As shown in Fig. 5.5, the simulation results of the CMV v_{cmv}, output voltage v_{out} and output current i_{out} for the qZSI system with the RSPWM (even), RSPWM (odd-even)

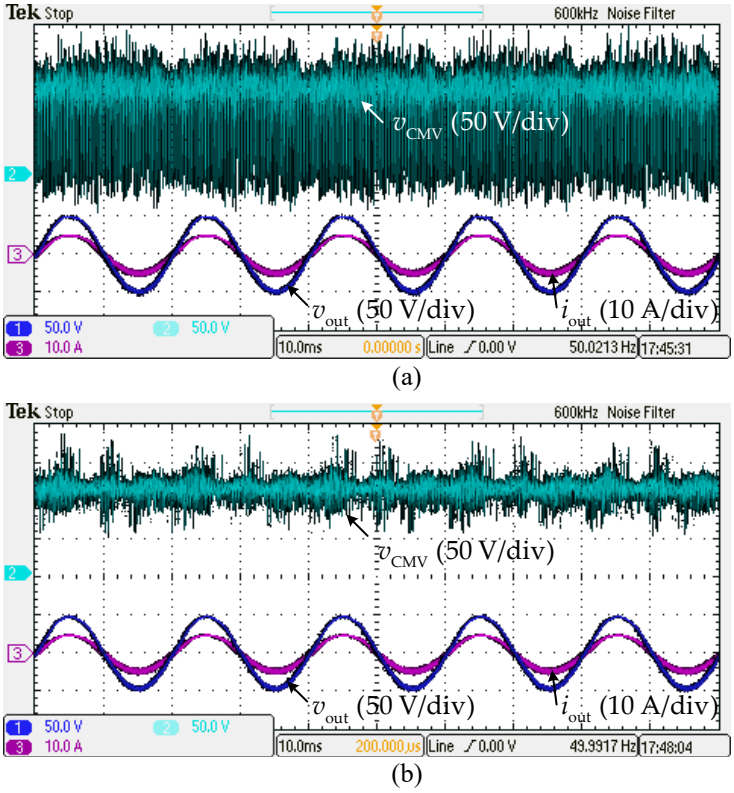

Fig. 5.6: Experimental results of the CMV v_{cmv} output voltage v_{out} and output voltage $i_{out}$when the RSPWM (even) strategy is used in the three-phase qZSI system (a) without the split input inductor and (b) with the split input inductor [Time (10 ms/div)].

and NSPWM strategies are given. Then, the experimental results of the CMV v_{cmv}, output voltage v_{out} and output current i_{out} for the qZSI system with the RSPWM (even) strategy are shown in Fig. 5.6.

Fig. 5.5(a) shows the CMV with the RSPWM (even) strategy with/without the split input inductor in qZSI system. The amplitude of the CMV without the split input inductor varies between 0 V and 133.33 V, while the CMV is constant as 120 V when the split ratio x is 2/3. The effect of the ST state on the CMV is removed with the proposed strategy, reducing the high-frequency components in the CMV. The output voltage v_{out} and output current i_{out} under those two systems are exactly the same, which reveals that the proposed CMV strategy will not affect the output quality, see Fig. 5.5(a). The simulation results when the RSPWM (odd-even) strategy is used are shown in Fig. 5.5(b). Referring to Table 5.2, the split ratio x is 1/2 with the RSPWM (odd-even). The CMV range of the qZSI system without the split inductor is

from 0 V to 133.33 V, while the CMV varies from 60 V to 120 V when adopting the proposed CMV reduction strategy. Meanwhile, the outputs are not affected while the high-frequency components partially removed, as shown in Fig. 5.5(b). Fig. 5.5(c) shows the simulation results of the qZSI when the NSPWM strategy is used. The split ratio x is $1/2$ for the input inductor in the qZSI system. The CMV range of the qZSI without the split input inductor varies from 0 V to 133.33 V, while CMV amplitude of the qZSI system with a split inductor changes between 60 V and 120 V, which is much smaller than the original qZSI system.

Fig. 5.6 shows the experimental results of the qZSI system with the RSPWM (even) strategy, which agree well with the simulation results in Fig. 5.5(a). The split ratio x is $2/3$ in this case, and all even switching vectors and a ST switching vector are used. As shown in Fig. 5.6(a), the CMV varies from 0 V to 133.33 V in the qZSI system without the split input inductor, which contains large high-frequency components. When the split inductors L_{11} and L_{12}, i.e., 350 uH, are used in the qZSI system, the CMV will become constant as 120 V, as illustrated in Fig. 5.6(b). The high-frequency components in the CMV have been removed, while the output quality remains with the proposed CMV strategy, as seen in Fig. 5.6. Thus, the proposed CMV strategy has been verified to be effective.

5.5 Summary

This chapter has investigated the CMV features of the three-phase two-level qZSI system for PV applications with low leakage currents. The impact of the ST state on the conventional CMV reduction strategies for the VSI has been studied. Furthermore, a CMV reduction strategy has been proposed, which enables the application of the conventional CMV reduction strategies in the three-phase two-level qZSI system. The strategy adopts a split input inductor to achieve the reduction of the CMV, and thus, lower leakage currents that are suitable for PV applications. Simulations and experimental tests have been performed to verify the effectiveness of the strategy.

6 Control of the QZSN-Based NPC Inverter

This chapter will explore the adoption of ST operational modes to achieve the neutral-point voltage (NPV) balancing for the three-phase neutral-point-clamped (NPC) qZSI. According to the space vectors of the three-phase NPC qZSI, two additional ST states, i.e., upper ST state and lower ST state, will be introduced in the control system to balance the NPV. Moreover, no extra CMV harmonics will be introduced with the proposed method for NPV balancing.

6.1 Introduction

With a smaller total harmonic distortion (THD) and lower device stresses, the three-phase three-level NPC inverter has been widely applied in the renewable generation system [93–95]. However, similar to the two-level VSI, the NPC inverter can only operate in the buck mode, which makes it unable to generate an ac voltage higher than the input voltage. As mentioned previously, the ISN can be inserted between the source and the converter to achieve boosting capability. As shown in Fig. 6.1, two qZSNs, i.e., $qZSN_1$ and $qZSN_2$, are used with the common point connected to the mid-point of the NPC converter in the three-phase NPC inverter, forming the NPC qZSI [96–99]. The three-phase NPC qZSI remains to have the same features as the two-level qZSI, e.g., a continuous input current and high boosting capability, while maintaining low-voltage stresses on power devices.

Although the NPC qZSI increases the system performance, the issue that occurs in the conventional NPC inverter will also challenge the application of the NPC qZSI, e.g., the imbalanced NPV [100, 101]. The imbalanced NPV can result from the capacitance mismatch of the upper and lower dc-link capacitors, abnormal switch characteristics, or nonlinear loads [102–104]. When the dc-link voltage imbalance appears, the output power quality will be affected with additional current harmonics [105–107]. The basic principle in the conventional NPC inverter for the NPV balancing is to redistribute the dwell time of the small vectors, which is related to either the upper dc-link voltage or the lower dc-link voltage [108, 109]. In addition to the 27 switching vectors in the conventional NPC inverter, the qZSN in the NPC qZSI introduces additional ST vectors [110]. Unlike the two-level qZSI with only full-ST state and non-ST state, there will be upper ST (UST) operational mode and lower ST (LST) operational mode, which are also related to the dc-link voltage. The conventional small vectors can balance the dc-link voltage by releasing the power stored in the capacitor with a higher voltage, while the additional ST vectors charge the capacitor with a lower voltage. Then, it is possible to utilize the ST vectors to achieve the NPV balancing.

Thus, this chapter will tackle the NPV imbalance issue with the redundant ST vectors in the NPC qZSI. The corresponding modulation method and the

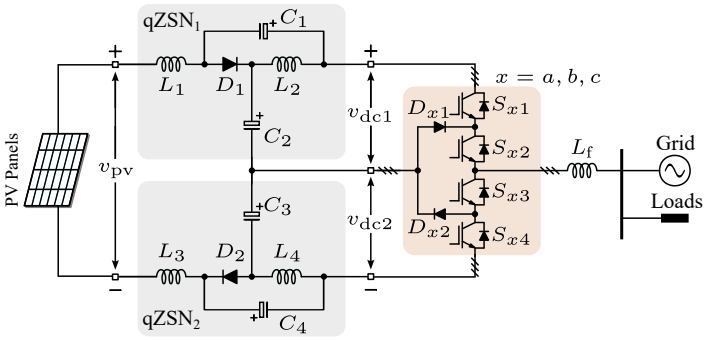

Fig. 6.1: Schematic of the three-phase NPC qZSI, which contains two qZSNs, i.e, $qZSN_1$ (L_1, L_2, C_1, C_2, and D_1) and $qZSN_2$ (L_3, L_4, C_3, C_4, and D_2), a three-phase NPC inverter (S_{x1}, S_{x2}, S_{x3}, S_{x4}, D_{x1} and D_{x2} with $x = a, b, c$), in which v_{dc1} and v_{dc2} are the upper and lower dc-link voltages, respectively.

NPV balancing control for the NPC qZSI will be investigated. In addition, the integrated closed-loop control strategy for the dc-link voltage control and NPV balance will also be presented in this chapter.

6.2 Operation of the Three-Phase NPC QZSI

Generally, the operational modes of the NPC QZSI can be divided as full-ST (FST) state in Fig. 6.2(a) and non-ST state in Fig. 6.2(b). In addition, two additional switching states, i.e., UST state in Fig. 6.2(c) and LST state Fig. 6.2(d), can be identified, as presented in [111]. According to Figs. 6.2(a) and (b), the steady-state values of the inductors i_{L1}, i_{L2}, and capacitors v_{C1}, v_{C2} with FST state modulation method can be derived as

$$V_{C1} = V_{C4} = \frac{D_{\text{sh}}}{2(1-2D_{\text{sh}})}V_{\text{in}}, \quad V_{C2} = V_{C3} = \frac{1-D_{\text{sh}}}{2(1-2D_{\text{sh}})}V_{\text{in}} \tag{6.1}$$

where V_{C1}, V_{C2}, V_{C3}, V_{C4} and D_{sh} are the steady-state values of v_{C1}, v_{C2}, v_{C3}, v_{C4} and d_{sh} (the ST duty ratio).

Similarly, according to Figs. 6.2(a), (c) and (d), when the UST and LST states are used in the modulation, the UST steady-state duty ratio D_{shu} and LST steady-state duty ratio D_{shl} should meet

$$D_{\text{shu}} = D_{\text{shl}} = 2D_{\text{sh}} \tag{6.2}$$

Then, the dc-link voltages when using the UST and LST states can be obtained as

$$V_{\text{dc1}} = \frac{1}{2(1-D_{\text{shu}})}V_{\text{in}}, \quad V_{\text{dc2}} = \frac{1}{2(1-2D_{\text{shl}})}V_{\text{in}} \tag{6.3}$$

where V_{dc1} and V_{dc2} is the peak values of the dc-link voltages v_{dc1} and v_{dc2} in Fig. 6.2, and V_{in} is the steady-state value of the input voltage v_{in}.

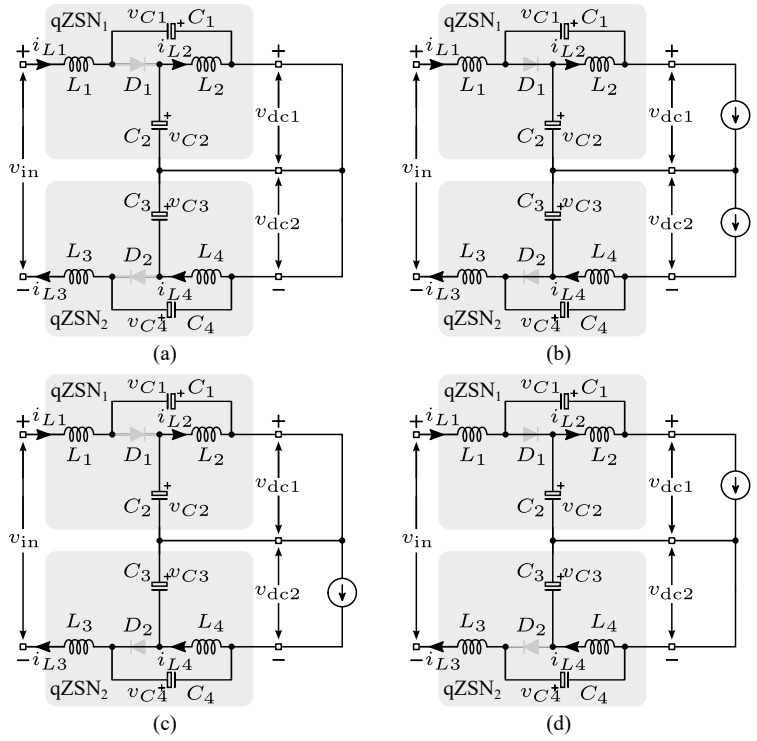

Fig. 6.2: Equivalent circuits of the NPC qZSI during: (a) FST state, (b) non-ST state, (c) UST state and (d) LST state.

Table 6.1: Switching states and the output voltage of the NPC qZSI.

States	On Switches	Output Voltage
P State	S_{x1}, S_{x2}	$+V_{dc}/2$
O State	S_{x2}, S_{x3}	0
N State	S_{x3}, S_{x4}	$-V_{dc}/2$
Full (F) ST State	S_{x1}, S_{x2}, S_{x3}, S_{x4}	0
Upper (U) ST State	S_{x1}, S_{x2}, S_{x3}	0
Lower (L) ST State	S_{x2}, S_{x3}, S_{x4}	0

The switching states and the output voltage are shown in Table 6.1, which includes the positive (P) state, zero (O) state, negative (N) state, FST state, UST state and LST state. Fig. 6.3 shows the schematic diagrams of the space vector modulation for the NPC qZSI. The time intervals of each sector can be calculated like the SVM for the two-level inverters by using the selected

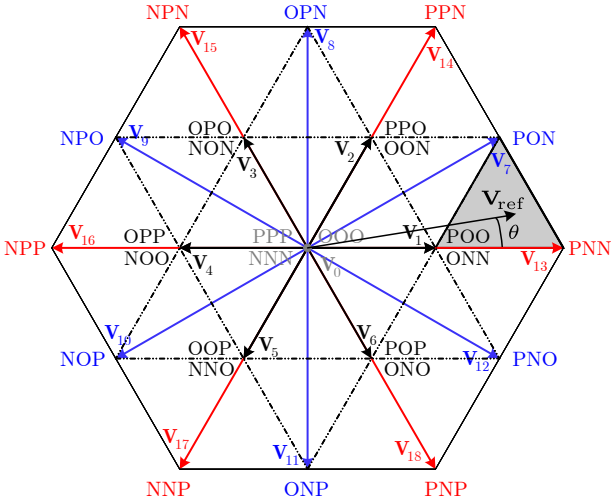

Fig. 6.3: Space vectors for the NPC qZSI, where P represents positive states, N indicates negative states, and O means zero states.

Table 6.2: Switching Sequence in the Shaded Sector with the SVM for NPC Inverter.

Sequence	Middle	Large	Middle	Small	Middle	Large	Middle
Vector	$\boldsymbol{V}_1$	$\boldsymbol{V}_{13}$	$\boldsymbol{V}_7$	$\boldsymbol{V}_1$	$\boldsymbol{V}_7$	$\boldsymbol{V}_{13}$	$\boldsymbol{V}_1$
State	ONN	PNN	PON	POO	PON	PNN	ONN

switching vectors. As shown in Fig. 6.3, and the shaded sector is taken as an example here with the corresponding duty ratios being

$$\begin{cases} d_{\mathrm{L}} = \sqrt{3} m \sin(\pi/6 - \theta) \\ d_{\mathrm{M}} = 2m \sin\theta \\ d_{\mathrm{O}} = 1 - d_{\mathrm{L}} - d_{\mathrm{M}} - d_{\mathrm{sh}} \end{cases} \tag{6.4}$$

where d_{L}, d_{M}, d_{O}, d_{sh} are the duty ratios of the large vector PNN, middle vector PON, zero vectors and ST vector, m is the modulation index, $\boldsymbol{V}_{\mathrm{ref}}$ is the reference voltage vector, and θ is the output angle of $\boldsymbol{V}_{\mathrm{ref}}$.

In order to achieve the minimum number of switching commutations, the switching states should only change between two adjacent states. The seven-segment switching sequence is adopted here. The switching sequence in the shaded sector in Fig. 6.3 with the SVM strategy for the traditional NPC inverter is then shown in Table 6.2. In this chosen sequence, there will be only one phase leg that changes the switching pattern, e.g., from ONN to

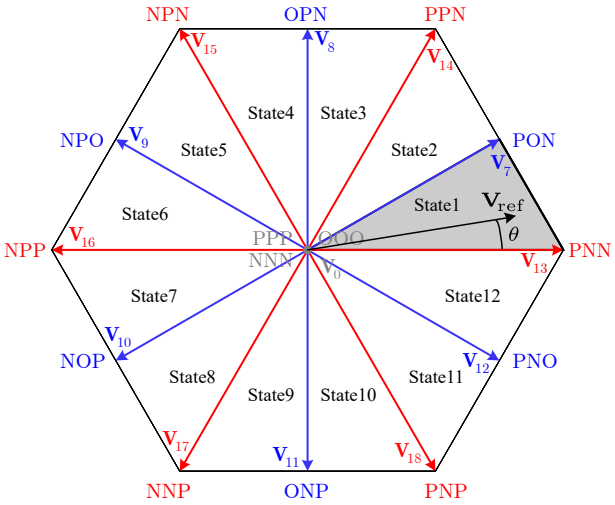

Fig. 6.4: Space vector diagrams for the NPC qZSI considering the CMV reduction.

PNN. However, the CMV of this strategy is large and additional intervals for small vectors are needed to achieve the NPV balancing. To implement the NPV balancing without introducing new CMV harmonics, a new method is proposed. The details of the NPV balancing strategy are presented in the next section.

6.3 Neutral-Point Voltage Balancing

In [112], all the small vectors were removed to reduce the CMV value, as shown in Fig. 6.4. With this strategy, the NPV can not be controlled or balanced by arranging the intervals for the small vectors. Accordingly, the switching sequence in the shaded sector with this CMV reduction strategy for the traditional NPC inverter is OOO-PON-PNN-PON-OOO. Then, the corresponding time intervals in the exemplified section can be obtained as

$$\begin{cases} d_{\mathrm{L}} = \sqrt{3} m \sin(\pi/6 - \theta) \\ d_{\mathrm{M}} = 2m \sin\theta \\ d_{\mathrm{O}} = 1 - d_{\mathrm{L}} - d_{\mathrm{M}} - d_{\mathrm{sh}} \end{cases} \tag{6.5}$$

which is the same as that in the conventional SVM strategy with an extended operational sector, as shown in Fig. 6.4. The switching sequence changes into five segments. To implement the ST state in the proposed strategy, the following sequence is defined to achieve the minimum number of switching commutations, as shown in Table 6.3.

Table 6.3: Proposed Switching Sequence for the NPV Balancing.

Sequence	Zero	ST	Middle	Large	Middle	ST	Zero
Vector	V_0	V_{st}	V_7	V_{13}	V_7	V_{st}	V_0
State1	OOO	UOL	PON	PNN	PON	UOL	OOO
Vector	V_0	V_{st}	V_7	V_{14}	V_7	V_{st}	V_0
State2	OOO	UOL	PON	PPN	PON	UOL	OOO
Vector	V_0	V_{st}	V_8	V_{14}	V_8	V_{st}	V_0
State3	OOO	OUL	OPN	PPN	OPN	OUL	OOO
Vector	V_0	V_{st}	V_8	V_{15}	V_8	V_{st}	V_0
State4	OOO	OUL	OPN	NPN	OPN	OUL	OOO
Vector	V_0	V_{st}	V_9	V_{15}	V_9	V_{st}	V_0
State5	OOO	LUO	NPO	NPN	NPO	LUO	OOO
Vector	V_0	V_{st}	V_9	V_{16}	V_9	V_{st}	V_0
State6	OOO	LUO	NPO	NPP	NPO	LUO	OOO
Vector	V_0	V_{st}	V_{10}	V_{16}	V_{10}	V_{st}	V_0
State7	OOO	LOU	NOP	NPP	NOP	LOU	OOO
Vector	V_0	V_{st}	V_{10}	V_{17}	V_{10}	V_{st}	V_0
State8	OOO	LOU	NOP	NNP	NOP	LOU	OOO
Vector	V_0	V_{st}	V_{11}	V_{17}	V_{11}	V_{st}	V_0
State9	OOO	OLU	ONP	NNP	ONP	OLU	OOO
Vector	V_0	V_{st}	V_{11}	V_{18}	V_{11}	V_{st}	V_0
State10	OOO	OLU	ONP	PNP	ONP	OLU	OOO
Vector	V_0	V_{st}	V_{12}	V_{18}	V_{12}	V_{st}	V_0
State11	OOO	ULO	PNO	PNP	PNO	ULO	OOO
Vector	V_0	V_{st}	V_{12}	V_{13}	V_{12}	V_{st}	V_0
State12	OOO	ULO	PNO	PNN	PNO	ULO	OOO

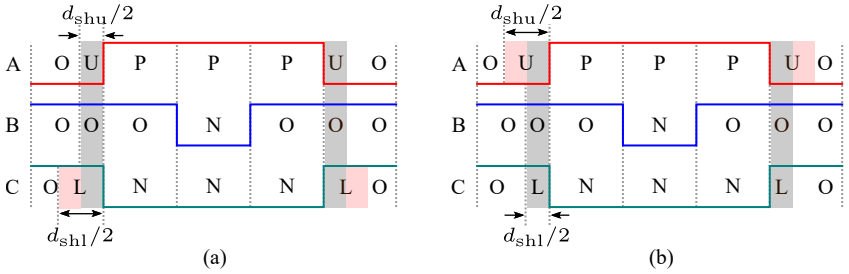

Fig. 6.5: Switching sequences when the dc-link voltage is imbalanced: (a) $v_{dc1} > v_{dc2}$ and (b) $v_{dc1} < v_{dc2}$, where A, B and C are the corresponding phases in the NPC inverter.

The sequence starts with a zero state to a large switching vector, and the ST state is inserted into the null state with UST and LST states in different phase legs, making the operational condition identical to the FST state. The conventional FST in the VSI, i.e, the upper and lower bridges in the same phase are short-circuited, will result in distortions in the output. To reduce the switching commutation, the change principle is the same as the conventional SVM, i.e., P state→UST state→O state→LST state→N state. As shown in Table 6.3 for the shaded sector, the inserted UST state is in phase A, while the LST state is used in phase C. When $v_{dc1} = v_{dc2}$, the NPV is balanced. The UST and LST duty ratios are equal, which will not result in the UST mode or the LST mode. If $v_{dc1} > v_{dc2}$, the NPC qZSI can charge the energy to the lower bridge in the proposed strategy. As shown in Fig. 6.5(a), the general dc-link voltage boosting can be implemented by inserted UST and LST in phases A and C separately (in grey). By increasing the time interval of the LST in phase C, the NPC will enter into the LST operational mode, as shown Fig. 6.2(d). In the proposed strategy, both UST and LST states will not affect the output active time intervals. When $v_{dc1} < v_{dc2}$, the basic boosting ST duty ratio remains, while an additional UST state will be inserted into phase A (in pink), as shown in Fig. 6.5(b). The UST operational mode is shown in Fig. 6.2(c), in which v_{dc1} will increase until $v_{dc1} = v_{dc2}$.

It should be pointed out that the maximum duty ratios of the UST and LST states should always be smaller than the duty ratio of the null state. The vectors and the switching states of the proposed strategy are further summarized in Table 6.3. According to [112], with the proposed strategy, the CMV of the NPC qZSI will be limited inside $V_{dc}/6$, which is a half of the maximum CMV when the conventional SVM strategy is used. Meanwhile, by adopting the null-like states, i.e., UST state and LST state, the NPV can be balanced without introducing extra CMV harmonics. In the conventional NPV balance strategy, the additional small vector will introduce a CMV value that varies from $-V_{dc}/6$ to $V_{dc}/6$. Thus, the proposed strategy can balance the NPV and reduce the CMV simultaneously.

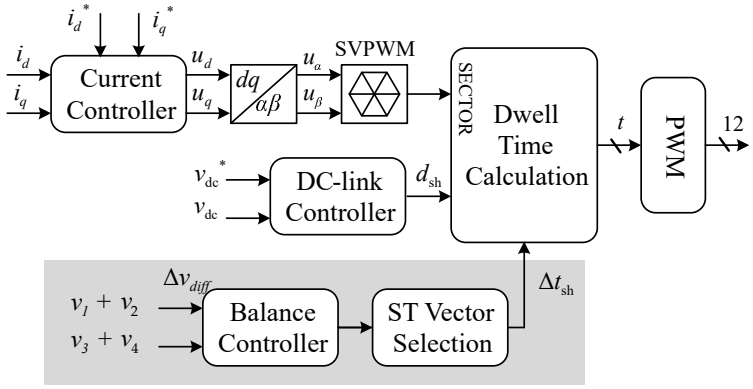

Fig. 6.6: Control system of the NPC qZSI with the NPV balancing and general dc-link voltage control, in which Δv_{diff} is the voltage difference between the upper and lower dc-link voltage, and Δd_{sh} is the extra UST or LST interval to balance the NPV.

Table 6.4: Parameters of the qZSI for model verification.

Parameter	Value
Input voltage v_{in}	500 V
Inductors L_1, L_2, L_3, L_4	1 mH
Capacitors C_1, C_2, C_3, C_4	1.5 mF
Output filter L_{f}	4 mH
Switching frequency f_s	10 kHz

The control system for the NPC qZSI with the NPV balancing and general dc-link voltage control is presented in Fig. 6.6. The ac side controller is the same as the conventional NPC inverter, which will not be further discussed in detail here. As an impedance source inverter, the NPC qZSI also encounters the issue that the dc-link voltage is varying. Similarly, the direct or the indirect dc-link controller can be used here, e.g, by controlling v_{C1}, v_{C2}, v_{C3}, v_{C4} or the combination of these variables. With the dc-link controller, the ST duty ratio d_{sh} for boosting the dc-link voltage can be obtained. When the derived time intervals for the null state and active states are implemented in the SVM technology, the switching sequence can be divided into a 5-segment sequence, and then extended into a 7-segment sequence by inserting the UST and LST states in the sequence, as shown in Table 6.3. Since the UST and LST states are inserted simultaneously in different phases, the total ST duty ratio remains as d_{sh}. If the NPV is balanced, the balance con-

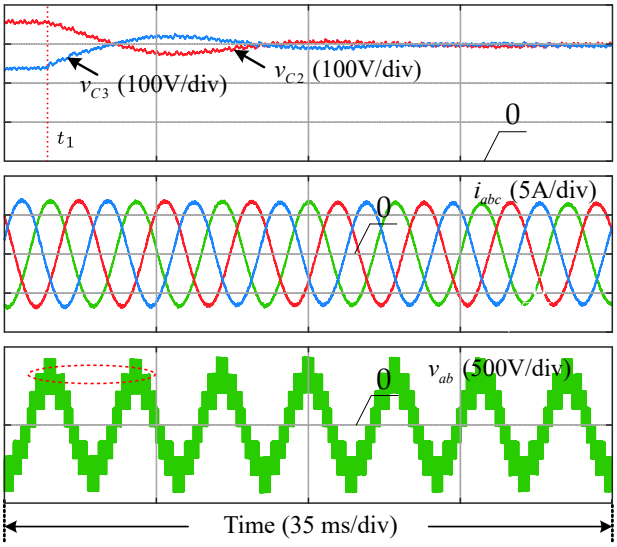

Fig. 6.7: Simulation results of the capacitor voltages v_{C2}, v_{C3}, output current i_{abc} and phase voltage v_{ab} with the proposed NPV balancing strategy: Time (35 ms/div).

troller will no work, meaning that the voltage difference Δv_{diff} and the upper and lower duty ratio Δd_{sh} are zero. However, if the NPV is imbalanced, the balance controller will be triggered. The proposed method will then charge the capacitor with a small dc-link voltage value, e.g., smaller V_{dc1} with an extra UST state. To increase the extra upper or lower ST duty ratio, the 7-segment sequence will be extended to a 9-segment sequence. As shown in Fig. 6.5(a), the switching sequence will change from OOO-UOL-PON-PNN-PON-UOL-OOO to OOO-OOL-UOL-PON-PNN-PON-UOL-OOL-OOO if the imbalance occurs with $v_{\text{dc1}} > v_{\text{dc2}}$. When $v_{\text{dc1}} < v_{\text{dc2}}$, the switching sequence will change from OOO-UOL-PON-PNN-PON-UOL-OOO to OOO-UOO-UOL-PON-PNN-PON-UOL-UOO-OOO. According to the active states, null states, FST states, UST state or LST state, the output control signal can be defined, as shown in Table 6.1 with the corresponding dwelling time. By using the above controller, the closed-loop control strategy for the dc-link voltage control and NPV balancing can be realized.

To verify the proposed NPV balancing strategy, simulations were performed on a three-phase NPC qZSI, , referring to Fig. 6.1. The system parameters of the three-phase NPC qZSI are listed in Table 6.4. The simulation results of the balanced capacitor voltages v_{C2}, v_{C3}, output current i_{abc} and phase voltage v_{ab} are presented in Fig. 6.7.

A 1-kΩ resistor was placed in parallel with the capacitor C_3 to generate the mismatch between the upper and lower bridge. There will be a 113-V voltage shift between v_{C2} and v_{C3} initially, as shown in Fig. 6.7. Meanwhile,

as presented in Fig. 6.7, the distortions occur in the phase voltage v_{ab}. By adopting the UST or LST states at t_1 (i.e., by enabling the introduced voltage balancing strategy), the NPV becomes balanced between v_{C2} and v_{C3}, as observed in Fig. 6.7. However, the settling time is longer with the distribution of the UST or LST states when compared with that when the small vectors are adopted. Although the settling time will increase with the proposed strategy, the CMV remains while the small vectors introduce additional harmonics.

6.4 Summary

This chapter has explored the possibility for the ST state in tackling the NPV imbalance issue in the three-phase three-level NPC qZSI. With two impedance networks in the NPC qZSI, there are two extra operational states, i.e., UST and LST states. By using the UST and LST states instead of the small vectors, an NPV balance strategy has been proposed in this chapter, which makes the most of the additional operational modes introduced by the UST and LST states. Moreover, the proposed strategy can maintain the CMV while the conventional method increases the CMV harmonics. Simulation results have been provided to verify the effectiveness of the proposed strategy. The study presented in this chapter validates the application of qZSNs in multilevel inverters for PV systems.

Part IV

Conclusions

The part is the conclusion of this Ph.D. project, which includes, ***Chapter 7****. Summary and Future Work.*

7 Summary and Future Work

This chapter will summarize the research work and contribution of the Ph.D. project - *Modeling and Control of Impedance Source Converters for Grid-Connected PV Systems*. The main outcomes and contributions are highlighted, and the research perspectives are discussed in the end.

7.1 Summary

The main objective of this Ph.D. project was on how to make the most of the ISCs for PV applications when considered as an alternative to the conventional two-stage inverter. The project focused on modeling and control of the qZSC/qZSI and then addressing the issues due to the introduction of the ISNs and an additional ST state. More importantly, potential solutions have been explored in this project. A summary of this Ph.D. project is given as follows.

The background and motivation of this Ph.D. project were presented in *Chapter 1* with a review of the ISCs seen from the perspectives of topologies, modulation strategies, and control methods. The introduction of the ISN enables the boosting capability of the impedance source inverter by using an additional ST state, which is forbidden in the conventional VSI. Although the impedance network brings new possibilities, issues like the pulsating dc-link voltage, additional passive components, and common-mode voltage (CMV) with high-order harmonics should in turn be discussed. Accordingly, several sub objectives have been set up for exploration in *Chapter 1*.

The qZSI is exemplified in *Chapter 2* to investigate the possible operational modes of the qZSI. When the passive parameters in the qZSN are ideal, the operational modes of the qZSI can be simply classified into ST state and non-ST state. However, when encountering light loads, relatively low switching frequencies, or small inductance values, new operational modes, e.g., LIC mode and DCM, will appear. The LIC mode was then discussed in *Chapter 2*, and the operational boundary for the CCM and DCM ihas also been presented in this chapter. To obtain the critical parameters between different operational modes, the qZSI system was simplified into a qZSN-based dc-dc converter. The derived critical parameters were also verified by experimental tests in *Chapter 2*.

The ST state is inserted into the zero state of the conventional VSI, making the qZSN and the inverter coupled in the qZSI system. Although the control system of the qZSI system is similar to the two-stage structure, the ac part of the qZSI system cannot be simply considered as a VSI. In *Chapter 3*, the effect of the qZSN on the ac side controller design was then explored. The small-signal models of the qZSN were derived first with an equivalent load current. Then, the disturbance from the load current to the peak dc-link voltage was presented, which can be integrated into the ac side control system. From the above model, a resonant transfer function resulted from the qZSN was obtained, which lowers the phase margin of the ac side controller. At the end of *Chapter 3*, the cases, e.g., different operational conditions, which could trigger the instability of the qZSI system, were verified with simulations and the experimental test on the system stability conditions considering the control parameters were provided.

In *Chapter 4*, the modulation technique was used to implement the inductor current ripple reduction, which further reduces the system volume and increases the system power density with smaller inductance. The instantaneous inductor current ripples of the qZSI with six identical ST intervals were obtained, which were not optimized and related to the angular of the output reference. By limiting all the inductor current ripples inside the maximum inductor discharging current ripple in a switching cycle, the maximum inductor current ripple in a switching cycle can be limited. Meanwhile, the maximum discharging current ripple can be defined as the ripple boundary to simplify the ripple reduction calculation burden. With the proposed methods, the inductor current ripple reduction ratio can be up to around 30%, which will not be affected by the charging current ripples. The proposed strategies have been verified through experimental tests in *Chapter 4*.

The CMV fluctuations in the transformerless qZSI can result in large leakage currents. The use of the ST state makes the high-frequency components in the CMV of the qZSI larger than those in the VSI. Meanwhile, the ST state introduces a new CMV value that makes the conventional CMV reduction strategies no longer work. It is noticed that the inductor voltage and

the CMV during the operational process are complementary. Thus, a split-input-inductor strategy was proposed in *Chapter 5* for CMV reduction with the conventional CMV reduction strategies. The average CMV value and the dwelling intervals of the switching vectors were used to obtain the split ratio of the input inductor. The proposed CMV reduction strategy was verified to be effective at the end of *Chapter 5*.

To test the scalability and applicability of the ISNs, the three-phase NPC qZSI was explored in *Chapter 6*. With two qZSNs, there are more possibilities to solve the inherent issue in the NPC inverter, e.g., NPV imbalance. In addition to the full ST state and non-ST state, there will be two new ST states, i.e., upper ST state and lower ST state. Instead of using small vectors, the two new ST states can also be adopted to balance the NPV for the NPC qZSI. The small vectors will release the power from the capacitor with a higher voltage, while the ST state charges the capacitor with a smaller value. Meanwhile, the ST state shows the same feature with the null state for the CMV, which means the additional ST state can balance the NPV and reduce the CMV simultaneously. At the end of *Chapter 6*, the proposed NPV balance strategy was validated to be effective by simulations.

7.2 Main Project Contribution

The main contributions of this Ph.D. project can be summarized:

- Energy Transfer Mode Analysis and Critical Parameters Design

By replacing the ac side as a resistor load, the energy transfer process of the simplified qZSN-based converter has been analyzed in this Ph.D. project. The DCM and the LIC mode have also been discussed in this project. Besides the boundary of the CCM and DCM, the critical parameters between different operation modes, i.e., CISM-CCM, IISM-CCM, and DCM have been calculated. The CISM-CCM can then be taken as a special case for the LIC mode. With the obtained critical parameters between those operational modes, the design consideration can be used in practical qZSI-based PV systems.

- Interactive Small-Signal Modeling Method for the QZSI

In order to explore how the ISN affects the dynamics of the ac controller, a general small-signal modeling method was developed in this Ph.D. project. The obtained model can reflect the coupling between the qZSN and the ac side by deriving a resonant transfer function. According to the interactive models, the impedance network will reduce the phase margin during the design of the ac controller. When countering a low input voltage, large ST duty ratio, or high output current, the instability might be triggered in the qZSI-based system. This contribution can be taken into practical design of qZSI systems for stable operation.

- Inductor Current Ripple Reduction for Higher Power Density

To reduce the inductor current ripple in the qZSN with the modulation technique, two modified ZSVM6 strategies have been proposed in this Ph.D. project. According to the instantaneous inductor current ripples of the conventional ZSVM6 strategy, a method by defining the maximum inductor current ripple in a switching cycle equal to the maximum discharging current ripple was presented. According to the maximum discharging current ripple in a line cycle, a method was proposed to make the instantaneous current ripple smaller than the maximum discharging current ripple for inductor current ripple reduction. Both methods can achieve the same ripple reduction ratio, while the first method generates a smaller instantaneous current ripple and the second method can reduce the computation burden. The current reduction can enable a higher power density of qZSI PV inverters that is desired in practice.

- Common-Mode Voltage Mitigation for PV Applications

Considering the high-order harmonics introduced by the additional ST state, this Ph.D. project made a contribution to the CMV reduction enabling the application of the qZSI in PV systems. With the ST state, the CMV reduction strategies for the two-level VSI are not suitable for the qZSI system. By making the most of the feature that the inductor voltage and the CMV during the operational process are complementary, a split-input-inductor strategy has been proposed for CMV reduction. According to the dwell time of the switching state, the average CMV value during the non-ST state can be derived. Then, the input inductor can be split accordingly by making the average CMV during the non-ST state equal to the CMV during the ST state. By doing so, the typical CMV reduction strategies can be applied to the qZSI no matter how the ST state is implemented. This further confirms the application of qZSCs in PV systems.

- Neutral-Point Voltage Balancing in the qZSI NPC Inverter

To further extend the application of the qZSNs, the NPC qZSI is of interest. Generally, the distribution of the small vectors in the NPC inverter is used to balance the NPV. With the use of two qZSNs in the NPC qZSI, a new NPV balance strategy was proposed in this Ph.D. project by using the additional ST operational states. By rearranging the upper ST state and the lower ST state, the phase bridge with a smaller value will enter into the corresponding ST state. Meanwhile, similar to the null state, the adoption of the ST state will not introduce new CMV harmonics. This contribution brings more possibilities of the qZSNs to enhance the performance of PV systems.

7.3 Future Research Perspectives

Although this Ph.D. project has investigated some issues on the control and application of the ISCs in grid-connected PV systems, more challenges remain to be addressed:

- New impedance source converters with better operation performance

  The qZSI is exemplified in this Ph.D. project for PV applications. However, the boosting gain of the qZSI is not high enough for a situation where the input voltage is very low. Meanwhile, the additional passive components also increase the volume and size of the system. New technologies, e.g., coupled inductors, planar transformers, switched capacitors, and new power devices, can also improve the impedance source converters. Then, the development of new impedance source converters with better performance, e.g., higher boosting capability, fewer components and smaller volume, can enhance the impedance source converters for PV applications. The modeling and control of such new converters are of interest.

- Advanced control strategies for the impedance source converters

  With higher boosting capability, the impedance source converters show strong nonlinear features, which challenges the design of the control system. Advanced control strategies, e.g., model predictive controller, sliding mode controller, and artificial intelligence-based methods, can be considered for addressing the nonlinear issues. Moreover, the pulsating dc-link voltage and the decoupled structure in the ISCs induce more challenges for the control system. This is also interesting to explore.

- System-level reliability evaluation of the impedance source converters

  The impedance network introduces new paths, and the reliability assessment of the conventional converters may be modified for the ISCs. The passive components and power modules considering temperature, life prediction and fault detection should be covered in the reliability evaluation. Moreover, strategies that improve the reliability of the impedance source converters can also be studied.

Bibliography

References

[1] REN 21, "Renewables 2019: Global Status Report (GSR)," Tech. Rep., May 2019.

[2] F. Blaabjerg, R. Teodorescu, M. Liserre, and A. V. Timbus, "Overview of Control and Grid Synchronization for Distributed Power Generation Systems," *IEEE Trans. Ind. Electron.*, vol. 53, no. 5, pp. 1398–1409, Oct. 2006.

[3] S. V. Araujo, P. Zacharias, and R. Mallwitz, "Highly Efficient Single-Phase Transformerless Inverters for Grid-Connected Photovoltaic Systems," *IEEE Trans. Ind. Electron.*, vol. 57, no. 9, pp. 3118–3128, Sep. 2010.

[4] Y. Xue, L. Chang, S. B. Kjaer, J. Bordonau, and T. Shimizu, "Topologies of single-phase inverters for small distributed power generators: an overview," *IEEE Trans. Power Electron.*, vol. 19, no. 5, pp. 1305–1314, 2004.

[5] M. E. Ahmed, M. Orabi, and O. M. Abdelrahim, "Two-stage micro-grid inverter with high-voltage gain for photovoltaic applications," *IET Power Electron.*, vol. 6, no. 9, pp. 1812–1821, Nov. 2013.

[6] Y. Yang, K. A. Kim, F. Blaabjerg, and A. Sangwongwanich, *Advances in Grid-Connected Photovoltaic Power Conversion Systems*. Woodhead Publishing, 2018.

[7] Ó. López, F. D. Freijedo, A. G. Yepes, P. Fernández-Comesaña, J. Malvar, R. Teodorescu, and J. Doval-Gandoy, "Eliminating Ground Current in a Transformerless Photovoltaic Application," *IEEE Trans. Energy Convers.*, vol. 25, no. 1, pp. 140–147, Mar. 2010.

[8] F. Peng, "Z-source inverter," *IEEE Trans. Ind. Appl.*, vol. 39, no. 2, pp. 504–510, Mar. 2013.

[9] M. Shen, A. Joseph, J. Wang, F. Z. Peng, and D. J. Adams, "Comparison of Traditional Inverters and Z-Source Inverter for Fuel Cell Vehicles," *IEEE Trans. Power Electron.*, vol. 22, no. 4, pp. 1453–1463, Jul. 2007.

[10] T.-D. Duong, M.-K. Nguyen, Y.-C. Lim, J.-H. Choi, and D. M. Vilathgamuwa, "SiC-based active quasi-Z-source inverter with improved PWM control strategy," *IET Power Electron.*, vol. 12, no. 14, pp. 3810–3821, Sep. 2019.

[11] O. Ellabban and H. Abu-Rub, "Z-Source Inverter: Topology Improvements Review," *IEEE Ind. Electron. Mag.*, vol. 10, no. 1, pp. 6–24, Mar. 2016.

[12] W. Liu, J. Yuan, Y. Yang, and T. Kerekes, "Modeling and Control of Single-Phase Quasi-Z-Source Inverters," in *Proc. IECON*, Oct. 2018, pp. 3737–3742.

[13] W. Liu, Y. Yang, and T. Kerekes, "Characteristic Analysis of the Grid-Connected Impedance-Source Inverter for PV Applications," in *Proc. PEDG*, Jun. 2019, pp. 874–880.

[14] Y. P. Siwakoti, F. Z. Peng, F. Blaabjerg, P. C. Loh, and G. E. Town, "Impedance-Source Networks for Electric Power Conversion Part I: A Topological Review," *IEEE Trans. Power Electron.*, vol. 30, no. 2, pp. 699–716, Feb. 2015.

[15] Y. P. Siwakoti, F. Z. Peng, F. Blaabjerg, P. C. Loh, G. E. Town, and S. Yang, "Impedance-Source Networks for Electric Power Conversion Part II: Review of Control and Modulation Techniques," *IEEE Trans. Power Electron.*, vol. 30, no. 4, pp. 1887–1906, Apr. 2015.

[16] H. Abu-Rub, A. Iqbal, S. Moin Ahmed, F. Z. Peng, Y. Li, and G. Baoming, "Quasi-Z-Source Inverter-Based Photovoltaic Generation System With Maximum Power Tracking Control Using ANFIS," *IEEE Trans. Sustain. Energy*, vol. 4, no. 1, pp. 11–20, Jan. 2013.

[17] C. J. Gajanayake, D. M. Vilathgamuwa, P. C. Loh, R. Teodorescu, and F. Blaabjerg, "Z-Source-Inverter-Based Flexible Distributed Generation System Solution for Grid Power Quality Improvement," *IEEE Trans. Energy Convers.*, vol. 24, no. 3, pp. 695–704, Sep. 2009.

[18] S. K. Hoseini, A. Sheikholeslami, and J. Adabi, "Predictive modulation schemes to reduce common-mode voltage in three-phase inverters-fed AC drive systems," *IET Power Electron.*, vol. 7, no. 4, pp. 840–849, Apr. 2014.

[19] A. Abdelhakim, P. Davari, F. Blaabjerg, and P. Mattavelli, "Switching Loss Reduction in the Three-Phase Quasi-Z-Source Inverters Utilizing Modified Space Vector Modulation Strategies," *IEEE Trans. Power Electron.*, vol. 33, no. 5, pp. 4045–4060, May 2018.

[20] Y. Liu, H. Abu-Rub, B. Ge, F. Blaabjerg, O. Ellabban, and P. C. Loh, *Impedance source power electronic converters*. John Wiley & Sons, 2016.

[21] J. Anderson and F. Z. Peng, "Four quasi-Z-Source inverters," in *Proc. IEEE PESC*, Jun. 2008, pp. 2743–2749.

[22] Y. P. Siwakoti, F. Blaabjerg, and P. C. Loh, "New Magnetically Coupled Impedance (Z-) Source Networks," *IEEE Trans. Power Electron.*, vol. 31, no. 11, pp. 7419–7435, Nov. 2016.

[23] P. C. Loh and F. Blaabjerg, "Magnetically Coupled Impedance-Source Inverters," *IEEE Trans. Ind. Appl.*, vol. 49, no. 5, pp. 2177–2187, Sep. 2013.

[24] A. Nabae, I. Takahashi, and H. Akagi, "A New Neutral-Point-Clamped PWM Inverter," *IEEE Trans. Ind. Appl.*, vol. IA-17, no. 5, pp. 518–523, Sep. 1981.

[25] M. Hanif, M. Basu, and K. Gaughan, "Understanding the operation of a Z-source inverter for photovoltaic application with a design example," *IET Power Electron.*, vol. 4, no. 3, pp. 278–287, Mar. 2011.

[26] F. Z. Peng, M. Shen, and Z. Qian, "Maximum boost control of the Z-source inverter," *IEEE Trans. Power Electron.*, vol. 20, no. 4, pp. 833–838, Jul. 2005.

[27] M. Shen, J. Wang, A. Joseph, F. Z. Peng, L. Tolbert, and D. Adams, "Constant boost control of the Z-source inverter to minimize current ripple and voltage stress," *IEEE Trans. Ind. Appl.*, vol. 42, no. 3, pp. 770–778, May 2006.

[28] Y. Liu, B. Ge, H. Abu-Rub, and F. Z. Peng, "Overview of Space Vector Modulations for Three-Phase Z-Source/Quasi-Z-Source Inverters," *IEEE Trans. Power Electron.*, vol. 29, no. 4, pp. 2098–2108, Apr. 2014.

[29] S. An, X. Sun, Q. Zhang, Y. Zhong, and B. Ren, "Study on the Novel Generalized Discontinuous SVPWM Strategies for Three-Phase Voltage Source Inverters," *IEEE Trans. Ind. Inform.*, vol. 9, no. 2, pp. 781–789, May 2013.

[30] Y. Huang, M. Shen, F. Z. Peng, and J. Wang, "Z-Source Inverter for Residential Photovoltaic Systems," *IEEE Trans. Power Electron.*, vol. 21, no. 6, pp. 1776–1782, Nov. 2006.

[31] W. Liu, J. Yuan, Y. Yang, and T. Kerekes, "Modeling and Control of Single-Phase Quasi-Z-Source Inverters," in *Proc. IECON*, Oct. 2018, pp. 3737–3742.

[32] Y. Tang, J. Wei, and S. Xie, "Grid-tied photovoltaic system with series Z-source inverter," *IET Renew. Power Gener.*, vol. 7, no. 3, pp. 275–283, May 2013.

[33] S. Yang, F. Z. Peng, Q. Lei, R. Inoshita, and Z. Qian, "Current-Fed Quasi-Z-Source Inverter With Voltage Buck–Boost and Regeneration Capability," *IEEE Trans. Ind. Appl.*, vol. 47, no. 2, pp. 882–892, Mar. 2011.

[34] F. Guo, L. Fu, C.-H. Lin, C. Li, W. Choi, and J. Wang, "Development of an 85-kw bidirectional quasi-z-source inverter with dc-link feed-forward compensation for electric vehicle applications," *IEEE Trans. Power Electron.*, vol. 28, no. 12, pp. 5477–5488, 2013.

[35] W. Liu, Y. Yang, E. Liivik, D. Vinnikov, and F. Blaabjerg, "Critical Parameter Analysis and Design of the Quasi-Z-Source Inverter," in *Proc. IEEE UKRCON*, Jul. 2019, pp. 474–480.

[36] W. Liu, Y. Yang, and T. Kerekes, "Modified Quasi-Z-Source Inverter with Model Predictive Control for Constant Common-Mode Voltage," in *Proc. ICPE-ECCE Asia*, May 2019, pp. 1–6.

[37] Y. Liu, W. Liang, B. Ge, H. Abu-Rub, and N. Nie, "Quasi-Z-Source Three-to-Single-Phase Matrix Converter and Ripple Power Compensation Based on Model Predictive Control," *IEEE Trans. Ind. Electron.*, vol. 65, no. 6, pp. 5146–5156, Jun. 2018.

[38] A. Bakeer, M. A. Ismeil, and M. Orabi, "A powerful finite control set-model predictive control algorithm for quasi z-source inverter," *IEEE Trans. Ind. Informat.*, vol. 12, no. 4, pp. 1371–1379, 2016.

[39] M. Shen and F. Z. Peng, "Operation Modes and Characteristics of the Z-Source Inverter With Small Inductance or Low Power Factor," *IEEE Trans. Ind. Electron.*, vol. 55, no. 1, pp. 89–96, Jan. 2008.

[40] A. Liske, G. Clos, and M. Braun, "Analysis and modeling of the Quasi-Z-Source-Inverter," in *Proc. of IEEE IECON*, Nov. 2011, pp. 1197–1202.

[41] T. Kayiranga, H. Li, X. Lin, Y. Shi, and H. Li, "Abnormal Operation State Analysis and Control of Asymmetric Impedance Network-Based Quasi-Z-Source PV Inverter (AIN-qZSI)," *IEEE Trans. Power Electron.*, vol. 31, no. 11, pp. 7642–7650, Nov. 2016.

[42] B. Ge, Y. Liu, H. Abu-Rub, R. S. Balog, F. Z. Peng, S. McConnell, and X. Li, "Current ripple damping control to minimize impedance network for single-phase quasi-z source inverter system," *IEEE Trans. Ind. Inform.*, vol. 12, no. 3, pp. 1043–1054, 2016.

[43] D. Vinnikov, I. Roasto, R. Strzelecki, and M. Adamowicz, "CCM and DCM operation analysis of cascaded quasi-Z-source inverter," in *Proc. IEEE ISIE*, Jun. 2011, pp. 159–164.

[44] A. K. Chauhan, S. T. Mulpuru, M. Jain, and S. K. Singh, "A Cross-Regulated Closed-Loop Control for Hybrid L-Z Source Inverter," *IEEE Trans. Ind. Appl.*, vol. 55, no. 2, pp. 1983–1997, Mar. 2019.

[45] Y. Li, S. Jiang, J. G. Cintron-Rivera, and F. Z. Peng, "Modeling and Control of Quasi-Z-Source Inverter for Distributed Generation Applications," *IEEE Trans. Ind. Electron.*, vol. 60, no. 4, pp. 1532–1541, Apr. 2013.

[46] W. Liu, Y. Yang, E. Liivik, D. Vinnikov, and F. Blaabjerg, "Critical Parameter Analysis and Design of the Quasi-Z-Source Inverter," in *Proc. UKRCON*, Jul. 2019, pp. 474–480.

[47] Y. Liu, B. Ge, H. Abu-Rub, and D. Sun, "Comprehensive Modeling of Single-Phase Quasi-Z-Source Photovoltaic Inverter to Investigate Low-Frequency Voltage and Current Ripple," *IEEE Trans. Ind. Electron.*, vol. 62, no. 7, pp. 4194–4202, Jul. 2015.

[48] K. Wolski, M. Zdanowski, and J. Rabkowski, "High-frequency SiC-based inverters with input stages based on quasi-Z-source and boost topologies - experimental comparison," *IEEE Trans. Power Electron.*, pp. 1–1, 2019.

[49] W. Liu, Y. Yang, T. Kerekes, and F. Blaabjerg, "Generalized Space Vector Modulation for Ripple Current Reduction in Quasi-Z-Source Inverters," *IEEE Trans. Power Electron.*, vol. 36, no. 2, pp. 1730–1741, 2021.

[50] C. J. Gajanayake, D. M. Vilathgamuwa, and Poh Chiang Loh, "Small-signal and signal-flow-graph modeling of switched Z-source impedance network," *IEEE Power Electron. Lett.*, vol. 3, no. 3, pp. 111–116, Sep. 2005.

[51] F. Guo, L. Fu, C. Lin, C. Li, W. Choi, and J. Wang, "Development of an 85-kW Bidirectional Quasi-Z-Source Inverter With DC-Link Feed-Forward Compensation for Electric Vehicle Applications," *IEEE Trans. Power Electron.*, vol. 28, no. 12, pp. 5477–5488, Dec. 2013.

[52] P. C. Loh, C. Gajanayake, D. Vilathgamuwa, and F. Blaabjerg, "Evaluation of Resonant Damping Techniquesfor Z-Source Current-Type Inverter," *IEEE Trans. Power Electron.*, vol. 23, no. 4, pp. 2035–2043, Jul. 2008.

[53] Y. Shi, T. Kayiranga, Y. Li, and H. Li, "Exploring the LCL Characteristics in GaN-Based Single-L Quasi-Z-Source Grid-Tied Inverters," *IEEE Trans. Ind. Electron.*, vol. 64, no. 10, pp. 7758–7768, Oct. 2017.

[54] Z. Liang, S. Hu, H. Yang, and X. He, "Synthesis and Design of the AC Current Controller and Impedance Network for the Quasi-Z-Source Converter," *IEEE Trans. Ind. Electron.*, vol. 65, no. 10, pp. 8287–8296, Oct. 2018.

[55] T. Suntio, T. Messo, and J. Puukko, *Power electronic converters: dynamics and control in conventional and renewable energy applications*. John Wiley & Sons, 2017.

[56] W. Liu, Y. Pan, and Y. Yang, "Small-Signal Modeling and Dynamic Analysis of the Quasi-Z-Source Converter," in *Proc. IECON*, Oct. 2019, pp. 5039–5044.

[57] B. Ge, Y. Liu, H. Abu-Rub, R. S. Balog, F. Z. Peng, S. McConnell, and X. Li, "Current Ripple Damping Control to Minimize Impedance Network for Single-Phase Quasi-Z Source Inverter System," *IEEE Trans. Ind. Inform.*, vol. 12, no. 3, pp. 1043–1054, Jun. 2016.

[58] J. Liu, J. Hu, and L. Xu, "Dynamic Modeling and Analysis of Z Source Converter—Derivation of AC Small Signal Model and Design-Oriented Analysis," *IEEE Trans. Power Electron.*, vol. 22, no. 5, pp. 1786–1796, Sep. 2007.

[59] P. C. Loh, D. M. Vilathgamuwa, C. J. Gajanayake, Y. R. Lim, and C. W. Teo, "Transient modeling and analysis of pulse-width modulated z-source inverter," *IEEE Trans. Power Electron.*, vol. 22, no. 2, pp. 498–507, 2007.

[60] P. C. Loh, D. M. Vilathgamuwa, Y. Lai, G. T. Chua, and Y. Li, "Pulse-width modulation of Z-source inverters," *IEEE Trans. Power Electron.*, vol. 20, no. 6, pp. 1346–1355, Nov. 2005.

[61] Y. Liu, B. Ge, H. Abu-Rub, and F. Z. Peng, "Overview of Space Vector Modulations for Three-Phase Z-Source/Quasi-Z-Source Inverters," *IEEE Trans. Power Electron.*, vol. 29, no. 4, pp. 2098–2108, Apr. 2014.

[62] S. Dong, Q. Zhang, and S. Cheng, "Inductor Current Ripple Comparison Between ZSVM4 and ZSVM2 for Z-Source Inverters," *IEEE Trans. Power Electron.*, vol. 31, no. 11, pp. 7592–7597, Nov. 2016.

[63] S. Singh and S. Sonar, "A New SVPWM Technique to Reduce the Inductor Current Ripple of Z-Source Inverter," *IEEE Trans. Ind. Electron.*, vol. 67, no. 5, pp. 3540–3550, 2019.

[64] Y. Tang, S. Xie, and J. Ding, "Pulsewidth Modulation of Z-Source Inverters With Minimum Inductor Current Ripple," *IEEE Trans. Ind. Electron.*, vol. 61, no. 1, pp. 98–106, Jan. 2014.

[65] R. Iijima, T. Isobe, and H. Tadano, "Optimized Short-Through Time Distribution for Inductor Current Ripple Reduction in Z-Source Inverters Using Space-Vector Modulation," *IEEE Trans. Ind. Appl.*, vol. 55, no. 3, pp. 2922–2930, May 2019.

[66] Y. He, Y. Xu, and J. Chen, "New Space Vector Modulation Strategies to Reduce Inductor Current Ripple of Z-Source Inverter," *IEEE Trans. Power Electron.*, vol. 33, no. 3, pp. 2643–2654, Mar. 2018.

[67] D. G. Holmes, "The significance of zero space vector placement for carrier-based PWM schemes," *IEEE Trans. Ind. Appl.*, vol. 32, no. 5, pp. 1122–1129, Sep. 1996.

[68] W. Liu, Y. Yang, T. Kerekes, and F. Blaabjerg, "Generalized Space Vector Modulation for Ripple Current Reduction in Quasi-Z-Source Inverters," *IEEE Trans. Power Electron.*, vol. 36, no. 2, pp. 1730–1741, 2021.

[69] M. Cacciato, A. Consoli, G. Scarcella, and A. Testa, "Reduction of common-mode currents in PWM inverter motor drives," *IEEE Trans. Ind. Appl.*, vol. 35, no. 2, pp. 469–476, Mar. 1999.

[70] T. Kerekes, R. Teodorescu, M. Liserre, C. Klumpner, and M. Sumner, "Evaluation of Three-Phase Transformerless Photovoltaic Inverter Topologies," *IEEE Trans. Power Electron.*, vol. 24, no. 9, pp. 2202–2211, Sep. 2009.

[71] F. Bradaschia, M. C. Cavalcanti, P. E. P. Ferraz, G. M. S. Azevedo, F. A. S. Neves, and E. C. dos Santos, "Stability analysis of reduced leakage current modulation techniques for Z-source inverters in transformerless photovoltaic applications," in *Proc. ECCE*, Sep. 2011, pp. 2268–2275.

[72] Y. Tang, W. Yao, P. C. Loh, and F. Blaabjerg, "Highly Reliable Transformerless Photovoltaic Inverters With Leakage Current and Pulsating Power Elimination," *IEEE Trans. Ind. Electron.*, vol. 63, no. 2, pp. 1016–1026, Feb. 2016.

[73] H. Xiao and S. Xie, "Leakage Current Analytical Model and Application in Single-Phase Transformerless Photovoltaic Grid-Connected Inverter," *IEEE Trans. Electromagn. Compat.*, vol. 52, no. 4, pp. 902–913, Nov. 2010.

[74] B. Yang, W. Li, Y. Gu, W. Cui, and X. He, "Improved Transformerless Inverter With Common-Mode Leakage Current Elimination for a Photovoltaic Grid-Connected Power System," *IEEE Trans. Power Electron.*, vol. 27, no. 2, pp. 752–762, Feb. 2012.

[75] T. Kerekes, R. Teodorescu, P. Rodriguez, G. Vazquez, and E. Aldabas, "A New High-Efficiency Single-Phase Transformerless PV Inverter Topology," *IEEE Trans. Ind. Electron.*, vol. 58, no. 1, pp. 184–191, Jan. 2011.

[76] Y. Zhou, W. Huang, P. Zhao, and J. Zhao, "A Transformerless Grid-Connected Photovoltaic System Based on the Coupled Inductor Single-Stage Boost Three-Phase Inverter," *IEEE Trans. Power Electron.*, vol. 29, no. 3, pp. 1041–1046, Mar. 2014.

[77] W. Liu, Y. Yang, and T. Kerekes, "Modified Quasi-Z-Source Inverter with Model Predictive Control for Constant Common-Mode Voltage," in *Proc. ICPE-ECCE Asia*, May 2019, pp. 1–6.

[78] A. M. Hava and E. Ün, "A High-Performance PWM Algorithm for Common-Mode Voltage Reduction in Three-Phase Voltage Source Inverters," *IEEE Trans. Power Electron.*, vol. 26, no. 7, pp. 1998–2008, Jul. 2011.

[79] C.-C. Hou, C.-C. Shih, P.-T. Cheng, and A. M. Hava, "Common-Mode Voltage Reduction Pulsewidth Modulation Techniques for Three-Phase Grid-Connected Converters," *IEEE Trans. Power Electron.*, vol. 28, no. 4, pp. 1971–1979, Apr. 2013.

[80] T. Kerekes, R. Teodorescu, and M. Liserre, "Common mode voltage in case of transformerless PV inverters connected to the grid," in *Proc. ISIE*. IEEE, Jun. 2008, pp. 2390–2395.

[81] G. Buticchi, D. Barater, E. Lorenzani, and G. Franceschini, "Digital Control of Actual Grid-Connected Converters for Ground Leakage Current Reduction in PV Transformerless Systems," *IEEE Trans. Ind. Inform.*, vol. 8, no. 3, pp. 563–572, Aug. 2012.

[82] C. A. Rojas, M. Aguirre, S. Kouro, T. Geyer, and E. Gutierrez, "Leakage Current Mitigation in Photovoltaic String Inverter Using Predictive Control With Fixed Average Switching Frequency," *IEEE Trans. Ind. Electron.*, vol. 64, no. 12, pp. 9344–9354, Dec. 2017.

[83] P. Kakosimos and H. Abu-Rub, "Predictive Control of a Grid-Tied Cascaded Full-Bridge NPC Inverter for Reducing High-Frequency Common-Mode Voltage Components," *IEEE Trans. Ind. Inform.*, vol. 14, no. 6, pp. 2385–2394, Jun. 2018.

[84] X. Wang, J. Zou, L. Ma, J. Zhao, C. Xie, K. Li, L. Meng, and J. M. Guerrero, "Model predictive control methods of leakage current elimination for a three-level T-type transformerless PV inverter," *IET Power Electron.*, vol. 11, no. 8, pp. 1492–1498, Jul. 2018.

[85] S.-k. Mun and S. Kwak, "Reducing Common-Mode Voltage of Three-Phase VSIs using the Predictive Current Control Method based on Reference Voltage," *J. Power Electron.*, vol. 15, no. 3, pp. 712–720, May 2015.

[86] X. Guo, J. Zhou, R. He, X. Jia, and C. A. Rojas, "Leakage Current Attenuation of a Three-Phase Cascaded Inverter for Transformerless Grid-Connected PV Systems," *IEEE Trans. Ind. Electron.*, vol. 65, no. 1, pp. 676–686, Jan. 2018.

[87] N. Noroozi, M. R. Zolghadri, and M. Yaghoubi, "Comparison of common-mode voltage in three-phase quasi-Z-source inverters using different shoot-through implementation methods," in *Proc. CPE-POWERENG*, Apr. 2018, pp. 1–6.

[88] N. Noroozi and M. R. Zolghadri, "Three-Phase Quasi-Z-Source Inverter With Constant Common-Mode Voltage for Photovoltaic Application," *IEEE Trans. Ind. Electron.*, vol. 65, no. 6, pp. 4790–4798, Jun. 2018.

[89] X. Guo, Y. Yang, B. Wang, and F. Blaabjerg, "Leakage Current Reduction of Three-Phase Z-Source Three-Level Four-Leg Inverter for Transformerless PV System," *IEEE Trans. Power Electron.*, vol. 34, no. 7, pp. 6299–6308, Jul. 2019.

[90] X. Guo, Y. Yang, R. He, B. Wang, and F. Blaabjerg, "Transformerless Z-Source Four-Leg PV Inverter With Leakage Current Reduction," *IEEE Trans. Power Electron.*, vol. 34, no. 5, pp. 4343–4352, May 2019.

[91] M. Meraj, S. Rahman, A. Iqbal, and L. Ben–Brahim, "Common Mode Voltage Reduction in A Singlephase Quasi Z-Source Inverter for Transformerless Grid-Connected Solar PV Applications," *IEEE J. Emerg. Sel. Top. Power Electron.*, vol. 7, no. 2, pp. 1352–1363, 2018.

[92] F. Bradaschia, M. C. Cavalcanti, P. E. P. Ferraz, F. A. S. Neves, E. C. dos Santos, and J. H. G. M. da Silva, "Modulation for Three-Phase Transformerless Z-Source Inverter to Reduce Leakage Currents in Photovoltaic Systems," *IEEE Trans. Ind. Electron.*, vol. 58, no. 12, pp. 5385–5395, Dec. 2011.

[93] N. Celanovic and D. Boroyevich, "A comprehensive study of neutral-point voltage balancing problem in three-level neutral-point-clamped voltage source PWM inverters," *IEEE Trans. Power Electron.*, vol. 15, no. 2, pp. 242–249, Mar. 2000.

[94] A. K. Gupta and A. M. Khambadkone, "A Simple Space Vector PWM Scheme to Operate a Three-Level NPC Inverter at High Modulation Index Including Overmodulation Region, With Neutral Point Balancing," *IEEE Trans. Ind. Appl.*, vol. 43, no. 3, pp. 751–760, May 2007.

[95] A. Lewicki, Z. Krzeminski, and H. Abu-Rub, "Space-Vector Pulsewidth Modulation for Three-Level NPC Converter With the Neutral Point Voltage Control," *IEEE Trans. Ind. Electron.*, vol. 58, no. 11, pp. 5076–5086, Nov. 2011.

[96] F. B. Effah, P. Wheeler, J. Clare, and A. Watson, "Space-Vector-Modulated Three-Level Inverters With a Single Z-Source Network," *IEEE Trans. Power Electron.*, vol. 28, no. 6, pp. 2806–2815, Jun. 2013.

[97] P. C. Loh, F. Gao, F. Blaabjerg, and S. W. Lim, "Operational Analysis and Modulation Control of Three-Level Z-Source Inverters With Enhanced Output Waveform Quality," *IEEE Trans. Power Electron.*, vol. 24, no. 7, pp. 1767–1775, Jul. 2009.

[98] P. C. Loh, S. W. Lim, F. Gao, and F. Blaabjerg, "Three-Level Z-Source Inverters Using a Single LC Impedance Network," *IEEE Trans. Power Electron.*, vol. 22, no. 2, pp. 706–711, Mar. 2007.

[99] O. Husev, C. Roncero-Clemente, E. Romero-Cadaval, D. Vinnikov, and S. Stepenko, "Single phase three-level neutral-point-clamped quasi-Z-source inverter," *IET Power Electron.*, vol. 8, no. 1, pp. 1–10, 2015.

[100] S. Singh and S. Sonar, "A New SVPWM Technique to Reduce the Inductor Current Ripple of Z-Source Inverter," *IEEE Trans. Ind. Electron.*, vol. 67, no. 5, pp. 3540–3550, 2019.

[101] T. E. Shults, O. Husev, F. Blaabjerg, C. Roncero-Clemente, E. Romero-Cadaval, and D. Vinnikov, "Novel Space Vector Pulsewidth Modulation Strategies for Single-Phase Three-Level NPC Impedance-Source Inverters," *IEEE Trans. Power Electron.*, vol. 34, no. 5, pp. 4820–4830, May 2019.

[102] J.-S. Lee and K.-B. Lee, "New Modulation Techniques for a Leakage Current Reduction and a Neutral-Point Voltage Balance in Transformerless Photovoltaic Systems Using a Three-Level Inverter," *IEEE Trans. Power Electron.*, vol. 29, no. 4, pp. 1720–1732, Apr. 2014.

[103] W. Wei and W. Guangsen, "DC-link capacitor voltage balance strategy of independent double three-phase common bus five-level NPC/H-bridge inverter based on finite control set," *IET Power Electron.*, vol. 13, no. 8, pp. 1546–1553, 2020.

[104] D. Zhou, L. Ding, and Y. Li, "Two-Stage Model Predictive Control of NPC Inverter-Fed PMSM Drives Under Balanced and Unbalanced DC Links," *IEEE Trans. Ind. Electron.*, pp. 1–1, 2020.

[105] X. Xing, X. Li, F. Gao, C. Qin, and C. Zhang, "Improved Space Vector Modulation Technique for Neutral-Point Voltage Oscillation and Common-Mode Voltage Reduction in Three-Level Inverter," *IEEE Trans. Power Electron.*, vol. 34, no. 9, pp. 8697–8714, Sep. 2019.

[106] X. Xing, C. Zhang, A. Chen, J. He, W. Wang, and C. Du, "Space-Vector-Modulated Method for Boosting and Neutral Voltage Balancing in Z-Source Three-Level T-Type Inverter," *IEEE Trans. Ind. Appl.*, vol. 52, no. 2, pp. 1621–1631, Mar. 2016.

[107] U.-M. Choi and K. B. Lee, "Space vector modulation strategy for neutral-point voltage balancing in three-level inverter systems," *IET Power Electron.*, vol. 6, no. 7, pp. 1390–1398, Aug. 2013.

[108] A. Choudhury, P. Pillay, and S. S. Williamson, "Modified DC-Bus Voltage Balancing Algorithm for a Three-Level Neutral-Point-Clamped PMSM Inverter Drive With Reduced Common-Mode Voltage," *IEEE Trans. Ind. Appl.*, vol. 52, no. 1, pp. 278–292, Jan. 2016.

[109] C. Qin, C. Zhang, X. Xing, X. Li, A. Chen, and G. Zhang, "Simultaneous Common-Mode Voltage Reduction and Neutral-Point Voltage Balance Scheme for the Quasi-Z-Source Three-Level T-Type Inverter," *IEEE Trans. Ind. Electron.*, vol. 67, no. 3, pp. 1956–1967, Mar. 2020.

[110] P. C. Loh, F. Blaabjerg, and C. P. Wong, "Comparative Evaluation of Pulsewidth Modulation Strategies for Z-Source Neutral-Point-Clamped Inverter," *IEEE Trans. Power Electron.*, vol. 22, no. 3, pp. 1005–1013, May 2007.

[111] X. Xing, Z. Zhang, C. Zhang, J. He, and A. Chen, "Space Vector Modulation for Circulating Current Suppression Using Deadbeat Control Strategy in Parallel Three-Level Neutral-Clamped Inverters," *IEEE Trans. Ind. Electron.*, vol. 64, no. 2, pp. 977–987, Feb. 2017.

[112] C. Qin, C. Zhang, A. Chen, X. Xing, and G. Zhang, "A Space Vector Modulation Scheme of the Quasi-Z-Source Three-Level T-Type Inverter for Common-Mode Voltage Reduction," *IEEE Trans. Ind. Electron.*, vol. 65, no. 10, pp. 8340–8350, Oct. 2018.

ISSN (online): 2446-1636
ISBN (online): 978-87-7210-879-7 AALBORG UNIVERSITY PRESS